

**EXPLORATION OF SURFACE POTENTIAL IN ORGANIC SEMICONDUCTORS:  
STATIC BEHAVIOR, KINETICS, AND MORPHOLOGY**

by

**Paula Beth Hoffmann**

Bachelor's of Science, DePaul University, 2010

Submitted to the Graduate Faculty of the  
Dietrich School of Arts and Sciences in partial fulfillment  
of the requirements for the degree of  
Doctor of Philosophy

University of Pittsburgh

2015

UNIVERSITY OF PITTSBURGH  
DIETRICH SCHOOL OF ARTS AND SCIENCES

This dissertation was presented

by

Paula Beth Hoffmann

It was defended on

March 27, 2015

and approved by

Dr. Jill Millstone, Assistant Professor, Chemistry

Dr. David Waldeck, Professor, Chemistry

Dr. Tomasz Kowalewski, Professor, Carnegie Mellon Department of Chemistry

Dissertation Advisor: Dr. Geoffrey Hutchison, Assistant Professor, Chemistry

Copyright © by Paula Beth Hoffmann

2015

# **EXPLORATION OF SURFACE POTENTIAL IN ORGANIC SEMICONDUCTORS: STATIC BEHAVIOR, KINETICS, AND MORPHOLOGY**

Paula Beth Hoffmann, PhD

University of Pittsburgh, 2015

Organic electronic devices offer cheaper solution processability than their inorganic counterparts and allow for the vast tailorability of synthetic chemistry to tune properties and efficiency. A critical fundamental challenge is to understand the dynamics and mechanisms of charge transport, particularly the role of defects and traps. This is motivated in part by research we performed in the origins and occurrence of negative differential resistance (NDR) in phthalocyanine systems, discussed below. In this dissertation, I have explored the surface potential energy distributions of organic, semiconducting thin films via Kelvin probe force microscopy and analyzed the effects of disorder in the samples. Thin films of commonly used materials in organic electronic devices were tested, both on short and long time scales, and throughout these experiments, a previously unnoted asymmetry in the energetic distribution was observed. To determine the cause of this asymmetry, the energetic distributions were compared to a dynamic Monte Carlo simulation, with experimental and theoretical results suggesting nanoscale charge heterogeneity providing the greatest cause. These results were followed with additional experiments, first testing the evolution of the potential energy distribution over time and then testing intentionally patterned dual-component films to witness whether the asymmetry persisted or not. Over long scan times, the energetic distributions equilibrate to a more Gaussian distribution and shift in value, first quickly then more slowly, indicative of two different regimes of energetic disorder: shallow and deep, respectively. The patterned films were created using

multiple shapes at varying sizes, and they displayed no correlation between the degree of material patterning and the appearance of asymmetry. This indicates that while phase segregation may affect the potential energy distribution in organic semiconductors, it is not the main cause of asymmetry exhibited and explored here. It is important to more completely explore how disorder affects these materials, as they are commonly researched and utilized for organic electronic devices. With a greater understanding of disorder, more powerful and efficient devices can be created.

## TABLE OF CONTENTS

<b>ACKNOWLEDGEMENTS .....</b>	<b>XIX</b>
<b>1.0 INTRODUCTION.....</b>	<b>1</b>
<b>1.1 ELECTRONIC DEVICES.....</b>	<b>1</b>
<b>1.1.1 Material Variation .....</b>	<b>1</b>
<b>1.1.2 Complications and Loss Mechanisms in Organic Devices .....</b>	<b>2</b>
<b>1.2 CHARGE TRANSPORT IN DISORDERED MATERIALS.....</b>	<b>4</b>
<b>1.2.1 Simulation Method.....</b>	<b>5</b>
<b>1.2.2 Disorder Model.....</b>	<b>7</b>
<b>1.3 ATOMIC FORCE MICROSCOPY.....</b>	<b>9</b>
<b>1.3.1 Tapping and Contact modes .....</b>	<b>11</b>
<b>1.3.2 Kelvin Probe Force Microscopy (KPFM).....</b>	<b>12</b>
<b>1.3.3 Other Modes .....</b>	<b>14</b>
<b>2.0 NEGATIVE DIFFERENTIAL RESISTANCE IN IMPERFECT ORGANIC FIELD EFFECT TRANSISTORS .....</b>	<b>16</b>
<b>2.1 RESULTS .....</b>	<b>19</b>
<b>2.1.1 Electronic Structure.....</b>	<b>19</b>
<b>2.1.2 FET Measurements.....</b>	<b>20</b>
<b>2.1.3 AFM Measurements .....</b>	<b>22</b>

2.1.4	Monte Carlo Simulations .....	22
2.2	DISCUSSION.....	24
2.3	CONCLUSIONS AND CONTEXT.....	27
3.0	SURFACE POTENTIAL MAPPING IN STATIC, UNIMATERIAL FILMS.....	29
3.1	EXPERIMENTAL METHODS .....	31
3.1.1	Sample Preparation .....	31
3.1.2	Sample Characterization.....	32
3.2	KPFM DISTRIBUTIONS: EMERGENCE OF ASYMMETRY .....	33
3.3	UNDERSTANDING ASYMMETRIC SURFACE POTENTIAL DISTRIBUTIONS: NANOSCALE HETEROGENEITY .....	40
3.4	CONCLUSIONS .....	45
4.0	TIME EVOLUTION OF ASYMMETRIC POTENTIAL DISTRIBUTIONS .....	46
4.1	PROPOSED MECHANISM.....	48
4.1.1	Comparison to Theory.....	48
4.1.2	Instrument Artifacts .....	49
4.1.3	Interfacial Traps .....	50
4.2	DISCUSSION.....	52
4.3	CONCLUSIONS.....	59
5.0	INTERPLAY OF MORPHOLOGY AND ELECTRONIC PROPERTIES IN DUAL- COMPONENT, PATTERNED FILMS.....	60
5.1	STRATEGY: INTENTIONAL PHASE SEPARATION AND GRAIN BOUNDARIES BY MATERIAL PATTERNING .....	61
5.1.1	Experimental Methods .....	61

5.1.2	Results of Patterning.....	66
5.2	DISCUSSION.....	72
5.3	CONCLUSIONS.....	78
6.0	CONCLUSION .....	79
6.1	SUMMARY AND CONCLUSIONS.....	79
6.2	FUTURE DIRECTIONS.....	81
	ASYMMETRY CONTROL EXPERIMENTS .....	83
	KINETICS MODELING .....	100
	LAYER-BY-LAYER DEPOSITION TROUBLESHOOTING.....	106
	ELECTROCHEMICAL CHARACTERIZATION OF FILMS .....	112
	BIBLIOGRAPHY.....	115

## LIST OF TABLES

Table 3.1. Summation of KPFM Experimental Results .....	36
Table 3.2. Summation of Interfacial Test Results.....	39
Table 4.1. Control test for interfacial traps: summation of skewness values for samples where substrates were discharged before material deposition.....	52
Table 4.2. Summary of long time scale scans for P3HT and PEDOT samples.....	56
Table 5.1. Summary of patterned sample skewtest values. ....	74

### Appendix Tables

Appendix Table 1. Summary of varied film samples for troubleshooting layer-by-layer deposition.....	107
---	-----

## LIST OF FIGURES

Figure 1.1. Diagram of charge separation in an organic bulk heterojunction solar cell. ....	3
Figure 1.2. a) A visualization of the Monte Carlo simulation model and b) an example of the use of “random walk” architecture for use with charge movement. <sup>3</sup> .....	6
Figure 1.3. Charge transport in the simulation model interacting with a) noninteracting and b) interacting charged defects. <sup>3</sup> .....	7
Figure 1.4. A) Distributions of potential energy computed for monolayer organic semiconductor transistors for varied “seed trap” percentage (shown in the frames) and B) a visualization of the compared seed trap percentages, where more heterogeneous films have lowest seed percentage (1%) and homogeneous have higher (100%). <sup>4</sup> The distributions in A) were performed using only positive charges. Thus, they have a scale issue for comparison, but the shapes of the distribution are in agreement with more accurate simulations performed after these including negative charges as well. ....	9
Figure 1.5. Diagram of AFM working principles. ....	11
Figure 1.6. Diagram of working principles of KPFM. A) shows initial measurements performed by the instrument while B) shows the application of a bias to determine the contact potential difference between the tip and sample, which is translated into the sample’s surface potential. .	13

Figure 2.1. The chemical structures of Ni(II) 1,4,8,11,15,18,22,25-octabutoxy-29H,31H-phthalocyanine (NiOBuPc) and 5,9,14,18,23,27,32,36-octabutoxy-2,3-naphthalocyanine (OBuNc). The two structures differ in metal center and peripheral ligand substitution..... 18

Figure 2.2. Frontier orbitals for NiOBuPc and OBUnc..... 20

Figure 2.3. Example OFET IV curves A) 100% NiOBuPc and B) 75% OBUnc. The curve in B) exhibits NDR, which agrees with previous simulation predictions by our group<sup>3</sup>. New simulations in this paper detail the origins of this behavior. .... 21

Figure 2.4. Mobility vs. barrier concentration plots from A) experiment and B) theory. .... 21

Figure 2.5. A) Curve of the slope of the saturation region as a function of trap/barrier energy and B) simulated IV curve for tall barriers exhibiting NDR. .... 23

Figure 3.1. Representative height (a) and potential (b) scans and histogram (c) of the potential scan. .... 34

Figure 3.2. Representative histograms of surface potential scans obtained via KPFM for all materials and substrates. A-D) histograms of potential scans on varied materials as indicated (P3HT, PEDOT:PSS, 3T, and NiPS, respectively) and E-H) scans of P3HT on additional substrates for comparison with original ITO substrate samples (ITO, SiO<sub>2</sub>, Au, MgO, respectively). Gaussian distributions have been added to the histograms based on curve fitting from IgorPro to demonstrate inaccurate fits. .... 35

Figure 3.3. A) Schematic of heterogeneous islands of positive charge (blue) in a more homogeneous distribution of negative charges (red), leading to an asymmetric distribution of surface potentials. B) The heterogeneous spatial distribution of charges leads to a peak in short-range interactions. .... 41

Figure 3.4. (top) Histogram of experimental KPFM surface potentials from a P3HT/ITO film in Figure 2, illustrating asymmetry, and a best fit from a Voigt model of mixed Gaussian and Lorentzian disorder and (bottom) simulated surface potentials from a heterogeneous spatial distribution of positive charges and a more homogeneous distribution of negative charges. The skewness (asymmetry) of both distributions is similar..... 43

Figure 3.5. Compilation of Monte Carlo simulations of surface potentials as a function of heterogeneous spatial distribution of charge traps. A) Change in peak potential as the concentration of positive charges increases (with matching increase in negative charges), B) change in peak potential as the spatial heterogeneity of positive charges increases with constant charge concentration, C) saturation of asymmetric skewness with increasing concentration of positive charges, and D) change in skewness with increasing spatial heterogeneity. .... 44

Figure 4.1. Histograms of the surface potential scans for a PEDOT sample graphed in succession. Each scan took approximately 10 minutes for a total of 120 minutes of scan time. . 48

Figure 4.2. KPFM histograms indicating effects of discharging ITO substrates before deposition of P3HT. (left) Potential scans with a discharge time of 20 minutes and (right) with a discharge time of 100 minutes before measurement. .... 51

Figure 4.3. A) Histograms of surface potential energy scans graphed together for comparison. Each scan took ~6 minutes for a total scan time of ~70 minutes. B) Potential at highest count value for each of the histograms in A) graphed as a function of scan time..... 53

Figure 4.4 Figure showing example fits attempted for the data presented in Figure 4.3. A) Power, B) quadratic, and C) a combination of exponential and power function fits were utilized, but none presented an accurate representation of the data and its projection into longer time scales.

Fits were extended to 100 minutes to determine whether longer time scales would be well represented by the function..... 55

Figure 4.5 Height images for a PEDOT:PSS sample scanned over a long time frame (11 scans, ~2 hours) in the same place. .... 57

Figure 4.6 Potential images for a PEDOT:PSS sample scanned over a long time frame (11 scans, ~2 hours) in the same place. .... 57

Figure 5.1. Side-view diagram of the edges of diffraction grating from which the lined stamps were made. .... 63

Figure 5.2. Diagrams for the stamp patterns used in this experiment. They include 1 and 2  $\mu\text{m}$  lines, 2 and 5  $\mu\text{m}$  dots, and 6-pointed stars measuring approximately 6  $\mu\text{m}$ . Dark colors in the figure are voids, meaning that the stars are actually voids in the resultant stamp while dots and lines are features in the stamps. Both positive and negative star stamps were created and utilized during the experiments, but this is the only pattern for which negative stamps were made. .... 64

Figure 5.3. In both A) and B) above, APTES (aminopropyl triethoxysilane) was stamped onto PEDOT:PSS films via microcontact printing. Both of these images demonstrate an incomplete pattern transfer from the PDMS stamp to the sample surface, which was witnessed in most attempts of this patterning method..... 66

Figure 5.4. Height scan and line trace for 1  $\mu\text{m}$  line P3HT sample. These stamps had line patterns small enough that the patterning was consistent without much spreading of the PDMS during the stamping process..... 67

Figure 5.5. Height scan and line trace for 2  $\mu\text{m}$  line P3HT sample. Having been made from 500 lines/nm diffraction grating, the lines in these patterns appear wider. It is likely the stamp spreads during the imprinting process, producing a less-defined pattern..... 67

Figure 5.6. Height scan and line trace for 2  $\mu\text{m}$  dot P3HT sample. Slight amounts of bowing can be witnessed inside the dot patterns, as is evident in the line scan. These patterns were among the most consistent, as it appeared this size and pattern of stamps is ideal for imprinting. .... 68

Figure 5.7. Height scan and line trace for 5  $\mu\text{m}$  dot P3HT sample. As is evident in the figure, this size dot pattern is pushing the limits of the stamping process. Bowing occurred with the stamp, which is why the voids of the dot pattern appear hill-like while the “flat” areas appear to have dips in them..... 68

Figure 5.8. Height scan and line trace for star P3HT sample. This pattern was unique in that the features were voids in the stamp, making them features in the actual sample. Stamping was surprisingly consistent for such a large figure, as less bowing is seen than in the 5  $\mu\text{m}$  dot samples..... 69

Figure 5.9. KPFM example scans for a 1  $\mu\text{m}$  line sample after PCBM deposition. PCBM consistently deposited well into the line voids in these samples, though it is difficult to see accumulated negative potentials due to the small dimensions of the patterns..... 70

Figure 5.10. KPFM example scans for a 2  $\mu\text{m}$  line sample after PCBM deposition. Most of these types of patterned samples showed evidence of the lined pattern but also showed incomplete transfer. .... 70

Figure 5.11. KPFM example scans for a 2  $\mu\text{m}$  dot sample after PCBM deposition. The light areas in the potential scan correspond to P3HT-rich flat areas in the height scan. These samples exhibited incomplete filling of the dot voids by PCBM. It is possible that this is due to quicker PCBM diffusion into the P3HT regions from a smaller pattern size..... 71

Figure 5.12. KPFM example scans for 5  $\mu\text{m}$  dot samples after PCBM deposition. Evident in these samples were the coffee-ring like display of PCBM. Because the dot voids are so large, it

was difficult for the entire shape to be filled with PCBM, so deeper sections of the dots accumulated more PCBM clusters and an over all incomplete filling was noted. .... 71

Figure 5.13. KPFM example results for the star samples after PCBM deposition. The stars seen here are from a positive star stamp. These patterns were less consistent than others, and this is likely due to the sheer size of the star in the master. .... 72

Figure 5.14. Histograms of surface potential scans for the samples given in Figures 5.9 through 5.13. As can be seen in the figure, the 1  $\mu\text{m}$  line and star patterns in this example produced more symmetric distributions than the other patterns. The patterned sample sets produced consistent asymmetric distributions in the initial scan 95% of the time..... 73

Figure 5.15. Height and potential scans with potential histograms for samples from the same batch of a dropcast P3HT/PCBM film scanned via KPFM approximately 20-40 minutes apart. Similar topographies produce different potential distributions, indicating the source of the distributions' shapes is separate from topography..... 76

**Appendix Figures**

Appendix Figure 1. Height (left), phase (middle), and potential (right) scan images for each of the sample types tested. All scans are the first of the set taken for the sample and were taken in ambient conditions using experiment settings described in Chapter 3. .... 87

Appendix Figure 2. Topography (left column), potential (middle column), and correlation (right column) plots for each of the indicated materials. Height and potential scans were taken directly from experiment data. Correlation plots were calculated using the deviance of the height and potential scans calculated for each point in the grid. .... 88

Appendix Figure 3. Two P3HT samples scanned for the same amount of time after being prepared at the same time in the same manner. .... 89

Appendix Figure 4. Two samples (A and B) made from P3HT deposited onto ozone-treated ITO substrates and scanned via KPFM with sample grounding. Including height and potential scans of one scan and a histogram of all potential scans from the sample (as indicated). ..... 90

Appendix Figure 5. Surface potential distributions for acid-etched ITO and a P3HT solution deposited onto acid-etched ITO. .... 91

Appendix Figure 6. Histograms of multiple scans for P3HT/SAM samples. Both films are P3HT dropcast onto a TCOS or an APTES self-assembled monolayer. .... 92

Appendix Figure 7. A) Histograms of potential scans of P3HT films made at the same time utilizing both clean (left) and coated/contaminated (right) tips to determine the effects of contaminated tips on sample behavior. B) One P3HT sample was scanned successively with coated then clean tips (left) while the other from the same batch was scanned with clean then coated tips (right). .... 93

Appendix Figure 8. First and last (as indicated) topography scans of terthiophene (top), poly(3-hexyl)thiophene (middle), and polyethylene dioxythiophene: polystyrene sulfonate (bottom). Each scan lasts approximately 10 min. .... 95

Appendix Figure 9. Divided histograms for the top  $1 \times 5 \mu\text{m}^2$ , the entire scan ( $5 \times 5 \mu\text{m}^2$ ), and the bottom  $1 \times 5 \mu\text{m}^2$  for A) sulfonated nickel phthalocyanine, B) poly (3-hexyl)thiophene, and C) polyethylene dioxythiophene samples. Part D) shows an example of the method used to separate the scans to take histograms of different segments, by masking the rest of the scan. .... 97

Appendix Figure 10 Height images for a layer-by-layer deposited thin film of nickel phthalocyanine taken in the same spot using both non-contact (left) and Kelvin probe (right) modes. .... 98

Appendix Figure 11. A potential scan and corresponding line scan for a sample gold electrode tested via KPFM. Applied bias was changed approximately every micron by 0.2V and ranged from 0.6V to 1.4V..... 99

Appendix Figure 12 Peak potential versus scan time for several PEDOT:PSS samples. Linear fits were utilized to calculate the average change in potential over scan time for each of the two discharge regions. .... 101

Appendix Figure 13 Peak potential versus scan time for several P3HT samples. Linear fits were utilized to calculate the average change in potential over scan time for each of the two discharge regions..... 102

Appendix Figure 14 Example plots of fits attempting to model potential discharge data..... 103

Appendix Figure 15 Example first order rate plots for three samples (indicated)..... 104

Appendix Figure 16 Example second order rate plots for three samples (indicated). .... 105

Appendix Figure 17. UV-Vis spectra for phthalocyanine films tested for film deposition troubleshooting. A) shows spectra for films where PDDA was added to the wash water between film layers and spectra in B) are for films with no PDDA in the water bath. As can be seen, there is no appreciable film deposition without additional PDDA. Work done by Xialing Chen..... 108

Appendix Figure 18. KPFM data for phthalocyanine layer-by-layer films without PDDA in water baths used for rinsing samples between sample layers, including: A) height scan, B) potential scan, and C) potential histogram..... 109

Appendix Figure 19. KPFM data for phthalocyanine layer-by-layer films with PDDA in water baths used for rinsing samples between sample layers, including: A) height scan, B) potential scan, and C) potential histogram. In comparing this figure with Appendix Figure 13 above, a far rougher height profile is seen..... 110

Appendix Figure 20. Two current-voltage (IV) curves for nanotube devices. Both were created on the same wafer in the same way, with silver paint dotted on the ends of the nanotubes to create contacts. .... 113

## ACKNOWLEDGEMENTS

I've often heard the adage, "A journey of a thousand miles begins with a single step." Now, having completed this journey, I have a newfound appreciation for its sentiment. Looking back on over a decade of study in chemistry, it is surprisingly easy to remember the endless struggles and frustration all the way back to sophomore year of high school. Every year since then has presented a new challenge, and every year since then I've wondered if it would be the one I couldn't overcome. With great pride, I realize today that I've risen above every challenge presented to me, and with great humility, I extend the deepest gratitude to the people who have helped me do it.

First and foremost, I'd like to thank my family. Mom, you have always told me that I could do anything I put my mind to, and it is your absolute and unwavering confidence in me that has pushed me the hardest. Lauren and Kelly, you two have always combined to make the perfect duo: endless inspiration to achieve greatness and unconditional support to help make it so. Hayley, your friendship has provided endless support and entertainment, and were it not for you, I wouldn't have made it through this journey with my sense of humor intact. Dad, your focus on education helped instill that priority in me at a young age, and it continues to this day. Thanks also to the rest of my wacky family tree: you mean the world to me and I wouldn't be the person I am today without you.

Friendships have always been important to me, and I truly believe they provide the basis for a healthy life. Thanks to the close friends I've made throughout graduate school: you have helped to keep me sane and smiling through some of the most challenging years of my life. There are a handful of things I'll miss about Pittsburgh, and you are definitely one of them.

In addition to personal relationships, my academic and professional connections have helped guide and shape me as a scientist to this point. To all of my primary education teachers, thank you so much for the foundation on which my expertise has been built. Thanks to my professors, classmates, and lab partners for helping me grow and develop my scientific knowledge and intellect. All of my labmates throughout graduate school have provided unique discussion, advice, and amusement, especially Chris, Xinfeng, Tamika, and Adam. To the members of my thesis committee, Dr. Millstone, Dr. Waldeck, and Dr. Kowalewski, thank you so much for your time, attention, challenging questions, and direction. Dr. Hutchison, I extend my gratitude to you for your detailed feedback, your patient answers to my endless questions, and your amusement at my hyper-organized antics.

Finally, thank you to Brad for swooping in at the "last minute" and helping me to finish school in contented mutual weirdness; I can't wait to start another adventure with you.

Thanks to all of these people and the others too numerous to mention, I feel ready and excited for the next chapter of my life. I know that with your help, I can go anywhere from here. After all, I believe Dr. Seuss said it best:

"You have brains in your head. You have feet in your shoes. You can steer yourself any direction you choose. You're on your own. And you know what you know. And YOU are the one who'll decide where to go."

## **1.0 INTRODUCTION**

### **1.1 ELECTRONIC DEVICES**

#### **1.1.1 Material Variation**

Since the beginning of the technical age, silicon and other inorganic semiconductors have been in widespread use/production. The major advantage of these materials, and why they have been utilized almost exclusively in the last sixty or so years, is that when purified and doped properly, they provide the effective charge transport pathways needed for electronic devices. The major downside, however, is that the purity required for use in electronics is extremely high (i.e. for solar cells purity must be at least 99.9999999%), especially when compared to the concentration of dopants required to encourage charge transport within the material.

Beginning in the 1990's, interest began to increase in the use of organic semiconductors for electronic devices. Due primarily to the difference in dielectric constant between the two types of materials, i.e. silicon dioxide and conducting polymers, charge transport is a much more complex process in organic materials, as discussed below and outlined in Figure 1.1. In addition, long-term stability is a concern for these types of less robust devices. Key advantages persist, however, and have maintained interest in the use of organic polymers and small molecules: synthetic tailorability, ease of processing, and low cost of production. With the help of synthetic chemistry, functionality, size, polarity, and many other properties can be changed according to requirements of device operation. Processing of films and devices with methods like roll-to-roll

printing, inkjet printing, and various spraying techniques provide many cost-effective, simple deposition methods from which to choose. Finally, the difference in cost between production of solar panel silicon and conducting polymer device materials alone is drastic, in addition to the significantly lower cost of processing techniques for organic materials.

### **1.1.2 Complications and Loss Mechanisms in Organic Devices**

The discrepancies in efficiency between organic and inorganic semiconductors primarily stem from a more complex process of charge separation in organic materials. An inorganic solar panel with a p-n junction architecture works according to the following process: a photon of light is absorbed, the electron is excited, the hole makes its way to the p-type portion of the material while the electron moves to the n-type doped material, and the two charges move to their respective electrodes. In an organic material, because of the much lower dielectric constant, the electron and hole cannot separate unless there is a much higher energetic favorability; they are a bound pair, referred to as an exciton. The charge separation process in an example organic device (a bulk heterojunction solar cell) is outlined in Figure 1.1 below.

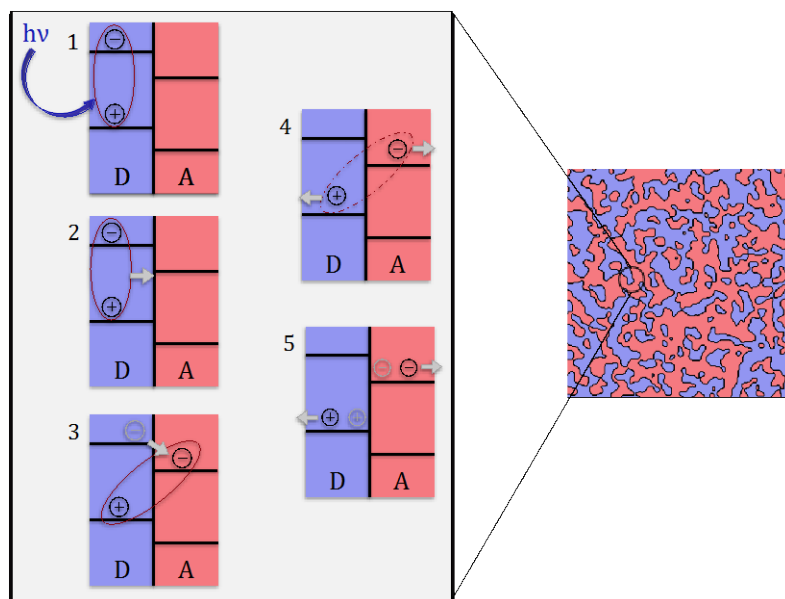


**Figure 1.1.** Diagram of charge separation in an organic bulk heterojunction solar cell.

A bulk heterojunction solar cell is comprised of a donor and an acceptor material, both of which are dispersed isotropically through the device. The process of charge separation occurs in the following steps. First, a photon is absorbed to create an exciton. Second, the exciton moves toward a grain boundary, where the energetics favor the transfer of the electron into the acceptor material. Third, the exciton breaks apart. Finally, the two charges move through their respective materials toward the electrodes.

Complications consistently arise during this process, as evidenced by its low efficiency. The two main processes in competition with full charge separation are exciton loss and charge recombination. The energy responsible for the excitation of the electron in the first step of the process may be lost in a myriad of ways in the time it takes for the exciton to reach the grain boundary. For instance, the exciton may collide with a defect or energetic trap in the film, in which case the energy would dissipate to neighboring molecules and the electron would de-excite. After successful separation, charges are traveling through a chaotic material landscape,

and there are many places where charges can (re)combine and de-excite as well. Both of these mechanisms, among others, contribute to the low efficiency and the material-specific challenges researchers face in organic electronic device design.

## **1.2 CHARGE TRANSPORT IN DISORDERED MATERIALS**

Similar to the distinctive charge separation processes in inorganic and organic semiconductor materials detailed above, charge transport occurs very differently in the two types of materials.<sup>1</sup> Consistent charge transport in an inorganic semiconductor is achieved by doping the material with impurities to introduce charge carriers and modify the charge band architecture. Different types of dopants encourage transport of either electrons or holes, based on whether the conduction or valence band of the material is moved closer to the Fermi level by the addition. Charge movement thus occurs similarly to that of a metal, with carriers moving freely through the lattice to produce current.<sup>2</sup>

Organic semiconductors, however, arrange in semi-crystalline lattices and have a much higher degree of disorder than their inorganic counterparts. Because of this, charge carriers are not free to move through the material but are localized on molecular sites, necessitating the use of thermally activated hopping to move. There are several theories on the rate by which this process occurs, the most common of which are Marcus-Hush and Miller-Abrahams, but there is not a distinct picture of the role of defects and disorder in the process. Defects come in many forms in conducting polymers and small molecules as both chemical and physical impurities, like contaminated materials or dust and dirt in the film, respectively. In addition, many electronic

devices require the use of multiple materials in device fabrication. Thus, a more complete understanding of disorder effects is necessary to further device development.

### **1.2.1 Simulation Method**

For several years, our research group has investigated the relationship between disorder and charge transport via Monte Carlo simulations with direct incorporation of disorder within the model.<sup>3-5</sup> The most unique aspect of the model is that it takes Coulomb interactions into account, both in between charge carriers and between charge carriers and charged defects. This is very computationally taxing, but it is also quite important in determining how charges and their movement are affected by defects within the device.

Monte Carlo simulations utilize repeated random sampling to determine the probabilities of the occurrence(s) in question. In our model, this becomes a monitoring of the location and movement of charge carriers within a monolayer device as they are affected by intentionally placed energetic traps and barriers in the model. This process is explained in more detail below.

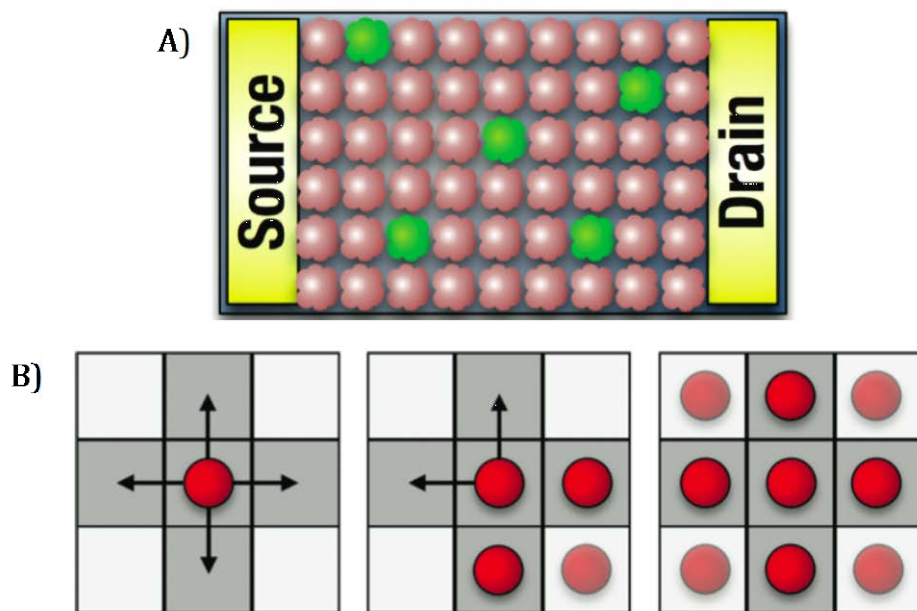


**Figure 1.2.** a) A visualization of the Monte Carlo simulation model and b) an example of the use of “random walk” architecture for use with charge movement.<sup>3</sup>

To begin, the model is set up like a grid, where each site represents one molecular space that can be occupied by a charge carrier. In Figure 1.2A, the grid is mostly made up of red sites (active, regular molecules) but also includes green sites (defects). During the course of the simulation, charges consider their surrounding neighborhood (exhibited in Figure 1.2B) and move according to calculated probabilities. The probability of a charge hopping to one of four nearest-neighbor sites is dependent on whether the site is occupied and the change in potential energy between sites. To study the role defects play in this process, defects as both non-interacting and interacting charges are placed within the simulation, seen in Figure 1.3.

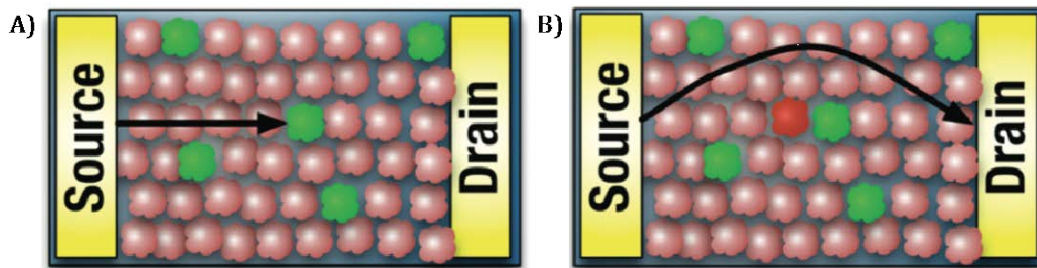


**Figure 1.3.** Charge transport in the simulation model interacting with a) noninteracting and b) interacting charged defects.<sup>3</sup>

Because Coulomb interactions are included in the simulation, the two transport scenarios in Figure 1.3 yield significantly different results. With a noninteracting defect (Figure 1.3A), the carrier is neither repulsed nor attracted and moves straight into it, becoming blocked. In Figure 1.3B, if the defect interacts with the carrier (and has the same sign), the carrier will be repulsed from the molecular site containing the defect and will likely move around and continue toward the drain, often times finding an alternate pathway to the electrode. In the case of the carrier and the defect having opposite signs, carriers would be attracted to the defect and accumulate, contributing to the creation of a charged island in the film. In which case, other carriers of the same sign would then move around the island similarly to that described in the first case.

After completing the simulation, many properties can be easily extracted, one of which is the potential energy distribution, which can provide information about how disorder affected the charge movement over the course of the run.

### 1.2.2 Disorder Model

Most commonly, it is assumed that disorder in a semiconductor system can be well-approximated via the Gaussian Disorder Model (GDM), developed by BäSSLer.<sup>6</sup> With the

assumption that electron-phonon coupling is weak and so polaron effects are neglected, charge hopping rates would be well-described by Miller-Abrahams theory, where the charge hopping rate is dependent on the distance between the molecular sites and the energy barrier associated with it. Coupled with this is the requirement that the concentration of charge carriers is low enough that there is no significant interaction between them<sup>7</sup>. Bässler then asserted that energy distribution of the localized molecular sites could be approximated by a Gaussian function, where both positional and energetic disorders are incorporated. This is supported by absorption spectra of the materials typically having Gaussian profiles and that coupling between a charge carrier and random distribution of dipoles leads to a Gaussian density of states function.

Given these assumptions, it stands to reason that the energy profile for organic semiconductor thin films, both theoretically and experimentally, would produce a Gaussian profile as well. However, the assumptions described in the model are inaccurate for organic semiconductors. Electron-phonon coupling in organic materials is strong and the concentration of charge carriers likely exceeds the low-carrier limit. Thus, Marcus theory of electron transfer, which takes into account polaronic effects, is a more accurate representation<sup>8,9</sup>. The break down of this assumption is reinforced by our simulation results, which have yielded energetic distributions showing an asymmetric shape. This is not surprising, given the incorporation of Coulombic effects into the simulation.

The distributions in Figure 1.4A below were calculated for varying “seed percentages” of traps at the same 20% trap concentration within the simulation, which essentially controls the heterogeneity of traps, with the lowest seed percentage creating the most heterogeneous distribution and the highest seed percentage creating the most homogeneous (Figure 1.4B). It appears from the simulation results that not only does the heterogeneity of charge traps in the

semiconductor film have a large affect on the energetic distribution, but that the energetic distributions are rarely truly Gaussian in shape.

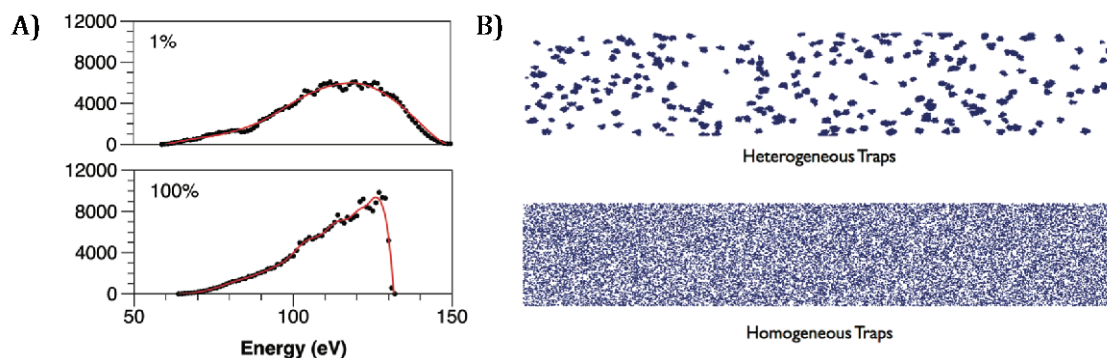


**Figure 1.4.** A) Distributions of potential energy computed for monolayer organic semiconductor transistors for varied “seed trap” percentage (shown in the frames) and B) a visualization of the compared seed trap percentages, where more heterogeneous films have lowest seed percentage (1%) and homogeneous have higher (100%).<sup>4</sup> The distributions in A) were performed using only positive charges. Thus, they have a scale issue for comparison, but the shapes of the distribution are in agreement with more accurate simulations performed after these including negative charges as well.

### 1.3 ATOMIC FORCE MICROSCOPY

Atomic force microscopy (AFM) was invented in the 1980’s following its precursor, scanning tunneling microscopy (STM). In recent decades, it has become an extremely versatile instrumental technique in a wide range of research fields for mapping and measuring nano- to micro-scale samples. The instrument operates via a small tool called the cantilever, which probes the surface of the sample to create a map. While optical microscopes are limited by the

wavelength of light, AFM is limited only by the constraints of the instrument architecture, like the size of the cantilever, the sensitivity of the feedback electronics, and the extension of the piezoelectric in the scanning head. For instance, the sensitivity of the measurement by the cantilever is limited by how small it can be made, and resolution cannot be achieved smaller than the tip radius for imaging. For instance, the cantilever tips used in experiments detailed below were machined from silicon wafers and have a radius of at least 10 nm, and consequently, the best resolution possible is  $>10$  nm with experimental factors likely increasing that number. This becomes less of an issue with continual advancements in tip fabrication to extend the length of the probe and increase resolution in multiple modes, i.e. height imaging or imaging of electronic properties. For example, a carbon nanotube-modified cantilever was sharpened to an apex of 5nm by *in situ* trimming in an ultra-high vacuum transmission electron microscope (UHV TEM) chamber. This tip, coupled with electrostatic force microscopy (EFM), resolved dopant features to within 10 nm in air, a significant improvement in resolution from previous measurements.<sup>10</sup>

Operation of the AFM is accomplished in a few simple steps. The cantilever is oscillated near or on the sample's surface. A laser point is focused on the cantilever's head and reflected onto a photodiode detector. As the cantilever is scanned across the sample, any changes in the oscillation of the cantilever, i.e. bumping into a feature on the surface, are recognized. The feedback electronics produce a nullifying bias that keeps constant the force exerted on the sample by the cantilever. This nullifying signal is then recorded and converted into a map of the surface. Figure 1.5 below shows a diagram of this process.

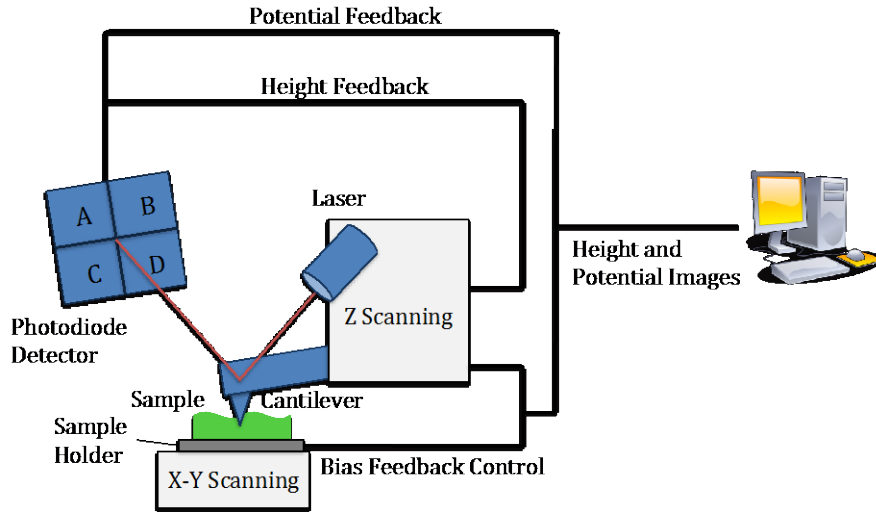


Figure 1.5. Diagram of AFM working principles.

### 1.3.1 Tapping and Contact modes

There are two common modes for topographical imaging: AC or tapping mode and contact mode. The ways in which they differ stem entirely from the type of contact the cantilever makes with the sample. As the names imply, cantilevers in contact mode drag along the sample while those in tapping mode make intermittent contact with the surface. The physical properties of a sample dictate a mode based on interaction with the motion of the cantilever.

Several factors are considered when determining the most advantageous mode for sample scanning, including whether the sample is easily damaged, its hardness, the degree of its surface height variation, and more. Samples that are difficult to remake or replace and are easily damaged should be imaged in tapping mode due to a lower force applied on the surface by the cantilever than that of contact mode. Similarly, softer samples should be imaged in tapping mode due to the possibility of the cantilever damaging the sample or, in fact, changing the topography

by moving material around. Harder samples are more resistant to changes from the cantilever and can be imaged in contact mode. Samples with a high degree of surface roughness (i.e. features that are taller than the height of the tip itself) should be imaged in tapping mode as well. This is due to the possibility of the tip breaking on sizeable features while imaging in contact mode. Because the tip is only making intermittent contact with a sample in tapping mode, it is more likely that the tip will encounter the feature before making full contact with the surface and be able to retract before damaging the tip. Whereas, in contact mode, the tip might hit the feature and break because of the increased time required to retract the piezo in the scanning head. These sample properties, among other things, must be considered when determining which of the AFM modes must be used.

### **1.3.2 Kelvin Probe Force Microscopy (KPFM)**

Kelvin probe force microscopy (KPFM) is an electrically based technique modeled after and using the same principles as the original Kelvin probe setup to measure the surface potential of a large-scale system.<sup>11</sup> The design of the tip-sample interaction is depicted in Figure 1.6 below. Both the metal-coated cantilever tip and the sample have an inherent work function associated with them. The instrument measures the work function of the sample relative to the tip by application of a nullifying bias (not unlike the feedback electronics in topography scanning mentioned above) to equilibrate the two work functions and measure the difference between them.

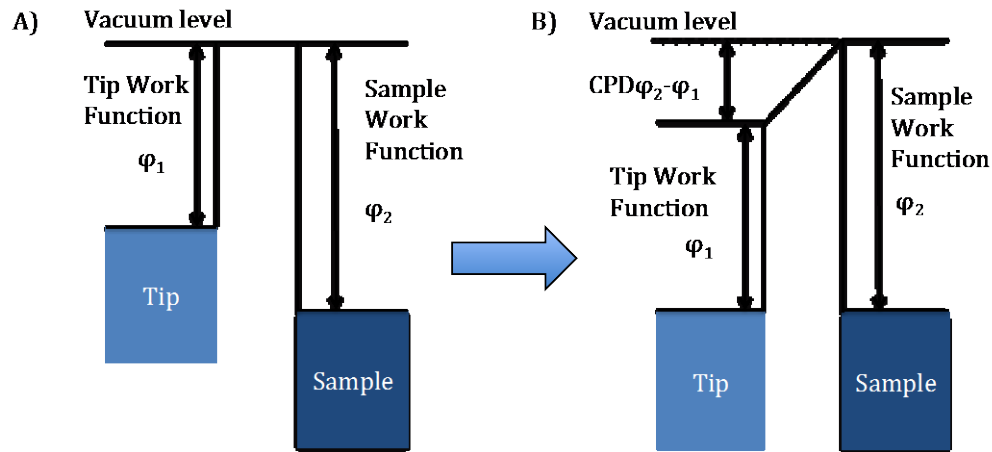


**Figure 1.6.** Diagram of working principles of KPFM. A) shows initial measurements performed by the instrument while B) shows the application of a bias to determine the contact potential difference between the tip and sample, which is translated into the sample's surface potential.

Due to the nature of this method, numerical data obtained from KPFM is somewhat subjective: the 2D map of surface potential with site energies compared to one another is useful information while the numerical values of the surface potential can vary dependent on changes in environment and work function of the tip and are thus arbitrary. Calibration of the tip ahead of the scan via a standard sample is typically used when contact potential difference needs to be measured outright.

Another complication that may arise from KPFM is a lower spatial resolution than with topographical scanning methods. KPFM itself is a double pass technique, which means it scans the height back and forth along one line, then rises above the surface of the sample a fixed amount and traces the same height profile it previously measured. In this way, the surface potential along the line (and entire scan) is measured continuously at the same height. As a consequence, the tip then measures electrostatic interaction from a higher portion of the sample, and the spatial resolution is decreased.

All in all, KPFM provides a measure of the energetics of a sample with little extra preparation of the sample or instrumentation, as many commercially available AFM setups include the capability as a standard. The only extra requirement is a metal-coated conductive cantilever.

### **1.3.3 Other Modes**

Conductive atomic force microscopy (CAFM) operates with electrically modified tips, the same that can be used in KPFM with a conductive coating, but is run in contact with the surface at all times. In this way, the instrument actually measures current via a modified cantilever holder equipped with a transimpedance amplifier. The distinction between the two modes (KPFM and CAFM) lies in the quantity measured by the instrument: KPFM measures the difference in potential between the tip and sample through a nullifying potential whereas CAFM is actually measuring a produced current resulting from a bias applied to the sample. Thus, the potential bias in KPFM is a dynamic quantity resulting from information obtained in the scan and the bias in CAFM is a fixed quantity that will produce varied current dependent on the sample properties.

Localized conductivity measurements can occur on very low amperage ranges; for example, the Asylum Research CAFM application can measure hundreds of femtoamps to ten microamps. This type of mode is most useful for ferroelectric films, nanotubes, thin dielectrics, conductive polymers, etc. With the increase in research interest for all of these areas and more, CAFM's prevalence has seen a large surge of use since its development and will likely see that continuing into the future.

Lateral force microscopy (LFM) is a mode useful for identifying dissimilar material regions within the same sample. Materials are identified by movement of the cantilever in a

unique direction from that typically detected: The detector is divided into four quadrants, shown in figure 1.5 above. Typical topography scans are measured by changes in deflection of the cantilever in the z direction, by subtracting the reflection of the light measured in quadrants C and D from that in quadrants A and B. LFM measures changes in twists of the cantilever, taking difference in A and C from B and D. These twists of the cantilever often come from differences in electrostatic interaction between multiple material types in a sample.

## 2.0 NEGATIVE DIFFERENTIAL RESISTANCE IN IMPERFECT ORGANIC FIELD EFFECT TRANSISTORS

*This chapter has been submitted for publication in Nature Materials and has been adapted to suit this dissertation. G.H. designed and directed the experiments and simulation. X.C., X.Q., P.H., and J.G. conducted the experiments. X.C. ran the electronic calculations. A.G. performed the Monte Carlo simulations. All authors discussed the results. X.C., A.G., P.H., and G.H. wrote the manuscript.*

Organic semiconductors have been used in many electronics to date, including organic field effect transistors (OFETs)<sup>12</sup>, organic photovoltaics (OPVs)<sup>13,14</sup>, and organic light emitting diodes (OLEDs). Compared to inorganic materials, organic semiconductors are synthetically variable<sup>15</sup>, recyclable, and potentially inexpensive due to solution processing<sup>16</sup> and roll-to-roll printing<sup>17</sup>. However, the presence of defects, such as dust or molecular voids, can lead to poor device performance. Thus, there are continued efforts to improve the charge transport properties of organic semiconductors, including synthesizing<sup>18</sup> materials with high mobility and optimizing device morphology<sup>19</sup>. Due to weak inter-molecular interactions<sup>20,21</sup>, organic semiconductors are very sensitive to impurities, defects, and traps in the film. The mechanism of how the traps affect charge transport in organic semiconductors is still not well understood, despite the intentional use of doping and mixtures in devices.

In a p-type material, the majority of carriers are holes. Holes denote an electron missing from the highest molecular orbital (HOMO) of the organic molecule. Charge transport occurs via the hopping of holes between the HOMOs of adjacent molecules. While the energy of each HOMO is somewhat random due to molecular disorder, a HOMO at a particularly high energy ( $\sim 0.1\text{eV}$ ) will act as a trapping site for holes. Likewise, molecules with low HOMO energies relative to adjacent molecules will act as a barrier, or “scattering” site<sup>22</sup>. If the relative HOMO energy is significantly lower ( $> 0.4\text{ eV}$ ), transport to the site becomes extremely unlikely. In this case, the site is called a defect.

The localization of carriers and large phonon coupling in organic semiconductors mean that impurities have great effect on charge transport. Removal of the impurities can lead to substantial improvement. For example, the measured mobility increases from about  $0.5\text{ cm}^2/\text{Vs}$  to  $2.2\text{ cm}^2/\text{Vs}$  when pentacene is purified via sublimation<sup>23,24</sup>. Other treatments, such as surface modification with perfluoropolyether (PFPE) can be used to quench trap sites<sup>25,26</sup>. The dipole moment normal to the substrate surface increases hole accumulation near the semiconductor/PFPE interface. This “trap-healing” effect leads to improved conductivity.

Traps, barriers, and defects do not just hinder charge transport. As this paper will show, barriers and defects can lead to negative differential resistance (NDR) in current-voltage (IV) curves. NDR is a phenomenon where the current decreases with increasing voltage over some portion of the IV curve. NDR is an interesting and relevant process for switching circuit and electronic oscillator applications. While NDR was observed as early as 1974 in GaAs<sup>27</sup>, numerous reports of doping and defect induced NDR have occurred more recently in the carbon nanotube literature<sup>28</sup>.

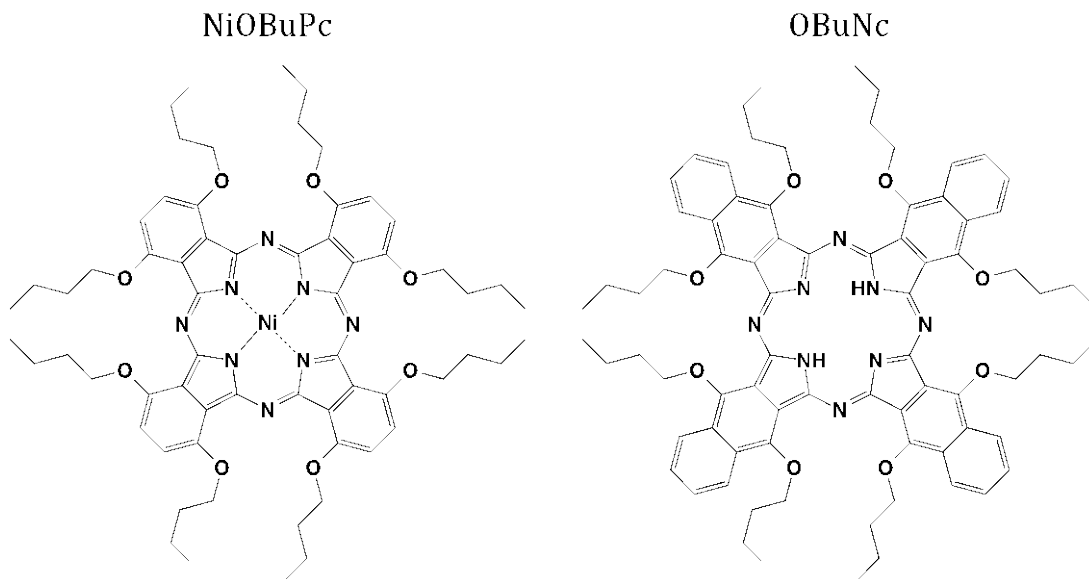


**Figure 2.1.** The chemical structures of Ni(II) 1,4,8,11,15,18,22,25-octabutoxy-29H,31H-phthalocyanine (NiOBuPc) and 5,9,14,18,23,27,32,36-octabutoxy-2,3-naphthalocyanine (OBUnc). The two structures differ in metal center and peripheral ligand substitution.

In this work, we have experimentally measured the mobility of phthalocyanine thin film transistors as a function of barrier concentration and compared it to theoretical Monte Carlo simulations performed earlier<sup>4</sup>. The host site was Ni(II) 1,4,8,11,15,18,22,25-octabutoxy-29H,31H-phthalocyanine (NiOBuPc) and the barrier site was 5,9,14,18,23,27,32,36-octabutoxy-2,3-naphthalocyanine (OBUnc), shown above in Figure 2.1. Pure and mixed films, ranging from 2.5% to 100% were fabricated via spin-coating. FET measurements of the mixed films showed NDR in the saturation region of the IV curve. Therefore, new Monte Carlo simulations of OFETs were performed to explain this phenomenon. The simulations suggest that tall barriers or defects can lead to NDR in IV curves.

## 2.1 RESULTS

### 2.1.1 Electronic Structure

The molecular orbital visualization in Figure 2.2 shows that the HOMO orbitals of NiOBuPc and OBUnc both have major contribution from porphyrine and phenyl rings, while the LUMO orbitals of these two molecules look quite different. The aromatic porphyrine rings have a larger contribution to OBUnc LUMO energy. However, the LUMO orbital in NiOBuPc is mainly located on an octabutoxyl alkyl arm. Therefore, this suggests that the LUMO energy difference between NiOBuPc and OBUnc should be larger than the HOMO energy difference. The calculated energy differences were -0.028 eV for HOMO and -0.385 eV for LUMO. We also used differential pulse voltammetry (DPV) to experimentally measure the difference in HOMO energies. The difference of the first oxidation peak of NiOBuPc and OBUnc, which is consistent with the HOMO-LUMO energy difference<sup>29</sup>, was 0.01 eV.

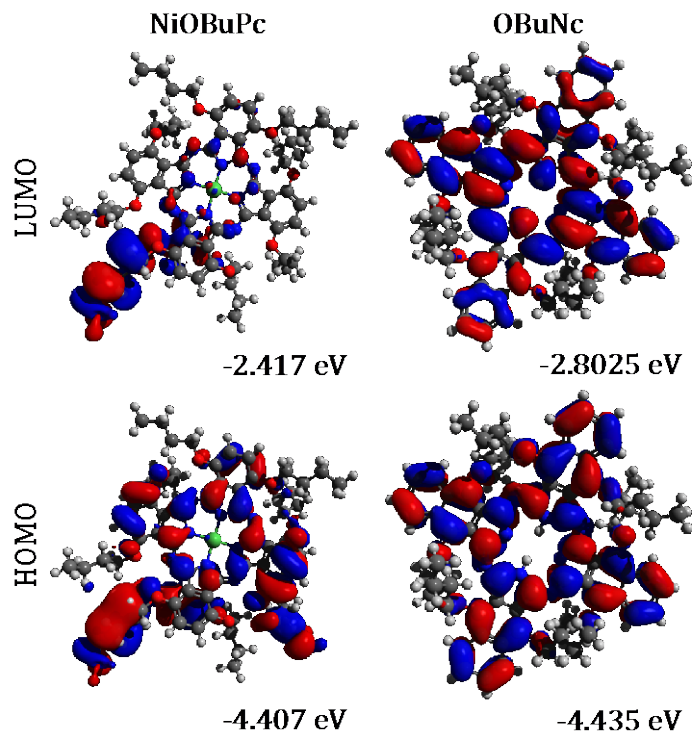


**Figure 2.2.** Frontier orbitals for NiOBuPc and OBUnc.

### 2.1.2 FET Measurements

For each film, the source drain voltage ( $V_{DS}$ ) was scanned from 0 to -30 V. Additionally, the gate voltage ( $V_G$ ) was varied from 0 to -15 V in 5 V intervals. Note that  $V_G$  is negative for p-type (hole conducting) materials. For values of  $V_G$  below 0 V, the source drain current ( $I_{DS}$ ) initially increased linearly and became saturated at large  $V_{DS}$ , typical of OFETs. A representative OFET IV curve is shown in Figure 2.3.

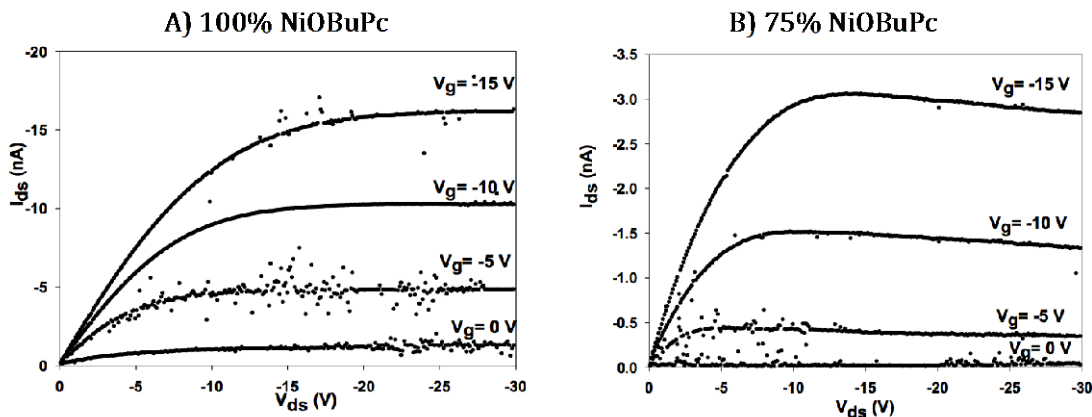


**Figure 2.3.** Example OFET IV curves A) 100% NiOBuPc and B) 75% OBUc. The curve in B) exhibits NDR, which agrees with previous simulation predictions by our group<sup>3</sup>. New simulations in this paper detail the origins of this behavior.

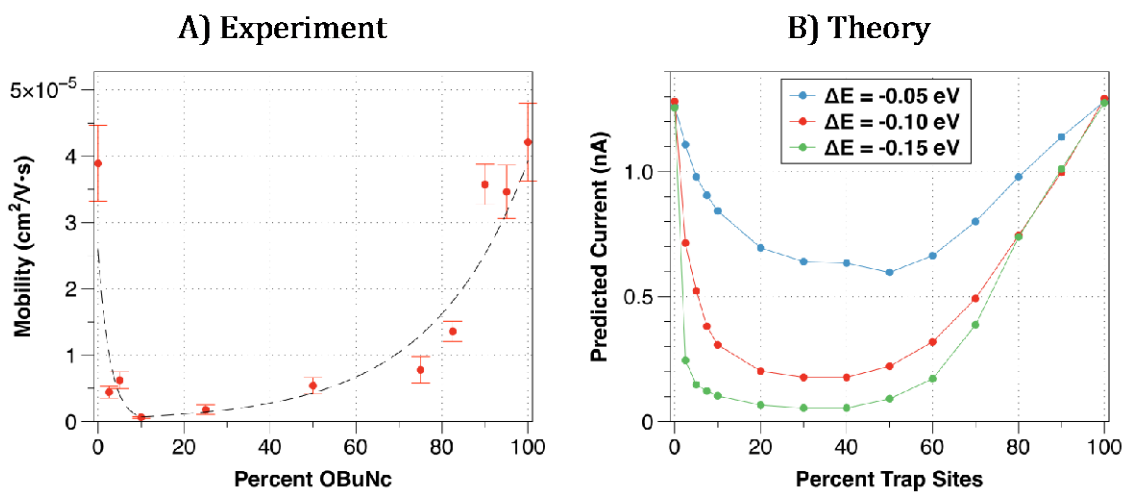


**Figure 2.4.** Mobility vs. barrier concentration plots from A) experiment and B) theory.

Figure 2.4A above shows mobility (calculated from the slope of a plot of  $\sqrt{I_{DS}}$  vs  $V_G$ ) as a function of barrier concentration. The asymmetrical trend of mobility agrees with the prediction from our Monte Carlo simulation (Figure 2.4B). Moreover, we found that  $I_{DS}$  decreases in the saturation region of our mixed films.

### 2.1.3 AFM Measurements

Surface topology of the films with different composition was characterized by tapping mode atomic force microscopy (AFM). Samples with OBUnc percentages of 0%, 25%, 50%, 75%, and 100% were chosen. Surfaces of all five films are smooth with low height roughness. The height roughness was 1.5 nm for OBUnc and  $\sim 0.3$  nm for the other four samples across a  $5 \mu\text{m} \times 5 \mu\text{m}$  area. No observable crystalline domains were seen from both height and phase images, indicating a homogeneous distribution of “traps” in the film at the scale of  $5 \mu\text{m} \times 5 \mu\text{m}$ .

### 2.1.4 Monte Carlo Simulations

IV curves for systems with defects, barriers, and traps were analyzed. We found that systems with defects and tall barriers ( $> 0.4$  eV) show NDR in the saturation region. Whereas, pure systems and systems with shallow traps did not. To understand this behavior, we examined the slope of the theoretical IV curves as a function of trap/barrier energy (Figure 2.5).

Figure 2.5A shows a curve of the slope of the saturation region (exemplified in Figure 2.5B) as a function of trap/barrier energy. The derivative of the IV curve has units of conductance (S), which is the inverse of resistance (R). Therefore, the slope is called the differential conductance. A negative differential conductance, then, is equivalent to a negative differential resistance. When the trap energy is zero (as in a pure system), the differential conductance is small and positive (0.04 nS). Ideal saturation would mean that the conductance does not change with voltage. This system is nearly entirely saturated.

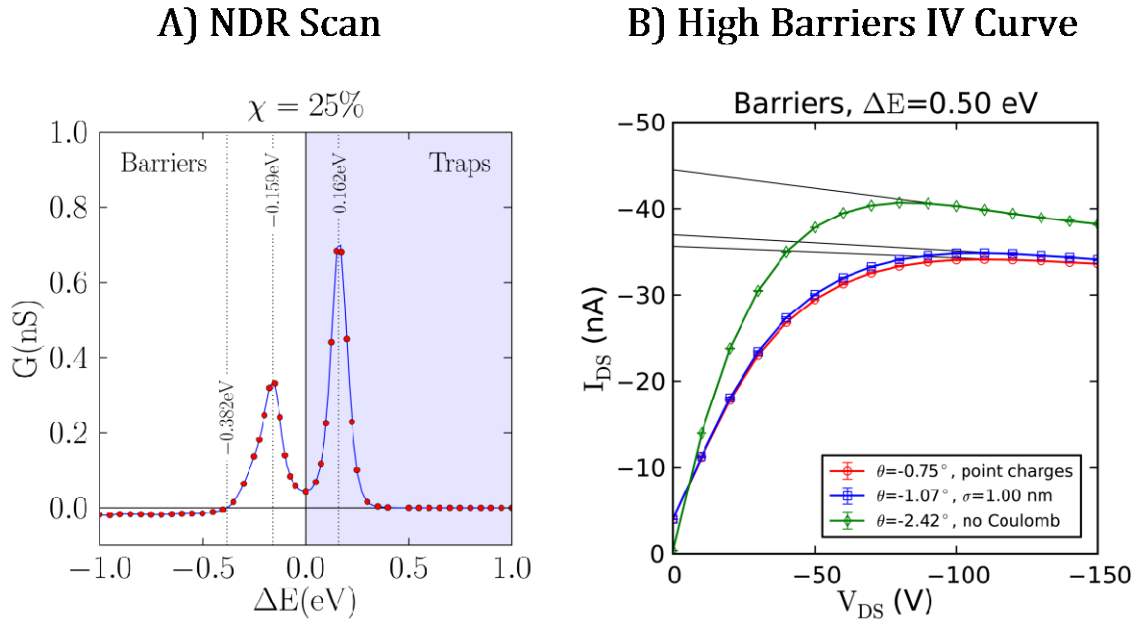


**Figure 2.5.** A) Curve of the slope of the saturation region as a function of trap/barrier energy and B) simulated IV curve for tall barriers exhibiting NDR.

Interestingly, as the trap or barrier energy increases, the differential conductance reaches a maximum at  $\pm 0.16$  eV. The peak for traps (0.68 nS) is nearly twice the height as the peak for barriers (0.32 nS). A larger differential conductance indicates a perturbed onset of ideal saturation. This suggests that traps are a larger hindrance to charge transport than barriers, likely because it is thermodynamically favorable to fall into a trap. The peak location in Figure 2.5A is near the energy associated with the potential difference between the source and drain electrodes at saturation for an adjacent site hop ( $e * 150 \text{ V} / 1024 \text{ nm} * 1 \text{ nm} \sim 0.15 \text{ eV}$ ). It is this energetic driving force, along with the Coulombic interactions between carriers, which drives carriers out of traps or past barriers. The presence of the peaks in Figure 2.5A indicates that traps/barriers are (at first) an increasing hindrance to ideal saturation.

As traps deepen beyond 0.16 eV, the differential conductance begins to fall and remains zero for traps deeper than 0.4 eV. Although the differential conductance calculated is zero

beyond 0.4 eV, a saturated IV curve does not exist. When traps are beyond 0.4 eV, there is nearly zero current, because nearly all carriers have become trapped and trap sites then far outnumber carriers. The simulation assumptions, such as constant carrier concentration, are likely invalid in this region. To obtain a more realistic result, a simulation with negatively charged defects could be performed. Barriers behave differently as they become larger than 0.16 eV. The differential conductance falls off, and becomes negative beyond 0.4 eV. At this energy, the barriers become insurmountable hills or defects.

## 2.2 DISCUSSION

It was reported by Ma<sup>30</sup> that both traps and barriers would decrease the mobility, but to a different degree. They found that traps reduced the mobility more strongly than the barriers and they attributed it to the different mechanism of how traps and barriers work: in the case of traps, the holes would be caught and could not move freely until there was sufficient thermal activation. However, while carriers are hindered by barriers, they may still move freely in the film. Qiu et. al<sup>31</sup> examined the effect of traps and barriers by doping the host semiconductor material, 4,4'-N,N'-dicarbazolebiphenyl (CBP), with three other different semiconductors of various energy level differences (low barriers, deep traps and deep barriers). They concluded that shallow traps and barriers decreased the mobility more than the deep dopants. While the energy barrier is not very large for shallow traps/barriers, carriers would still proceed in the regular hopping path between sites. However, if the energy barriers or dopants are large, the carriers will travel in elongated paths to avoid barrier sites.

Monte Carlo simulations performed suggest that shallow traps and barriers will also decrease the mobility of carriers. At a certain concentration dependent upon the trap/barrier energy, the mobility reaches a minimum value. It is true that the path of carriers may not change much in the presence of shallow traps/barriers, but there is an increased probability that carriers will remain on a trap site (or behind a barrier site) relative to normal sites. Thus, carriers spend more time in the film, decreasing the overall mobility. Nearly zero mobility is achieved by the presence of very deep traps, discussed above. The mobility can only recover in this regime when carriers begin to travel between the manifold of trap sites, occurring with significant increases in the number of those sites.

Our FET conductivity measurements show that the introduction of OBUnc decreased the charge transport in NiOBuPc strongly even though the morphology of the films did not look substantially different, which agreed with the simulation. However, the shallow barriers in the experiment produced the asymmetric mobility curve and NDR, both of which indicate the behavior of deep barriers predicted by the simulations.

The origin of NDR in the simulations is an interesting story. Consider, for example, that to have an escape probability of 1.0% without Coulomb interactions from a trap that is 0.3 eV deep, a  $0.391 \text{ eV C}^{-1} \text{ nm}^{-1}$  electric field is needed. As that is 391 V over 1000 nm, the device may decompose. In this situation (deep traps), all carriers in the OFET will be trapped and no current will flow. The Coulomb interactions between carriers will drastically lower the required voltage to free carriers from traps. For example, the repulsive energy from another like-charged carrier just 1 nm away is 0.411 eV. Ignoring the mean field energy from all other carriers, this means an extra 0.206 eV of energy is released when the carrier escapes the trap. This reduces the electric field needed (for a 1.0% probability) to  $0.185 \text{ eV C}^{-1} \text{ nm}^{-1}$ . Although 185V over 1000 nm is very

high, this calculation only includes the effect of a single extra like-charged charge. The addition of more charges will lower the voltage to a reasonable level. In this way, Coulomb interactions are significant for the de-trapping process in OFETs.

This is not the case for barriers, however. For a barrier at 0.3 eV, the above probabilities and voltage also apply. However, the process in question is transport to the barrier site rather than escape from a trap site, which is a crucial process for an OFET. While deep traps will reduce the current to zero rendering the device dead, current can still flow in the presence of high barriers, producing negative differential resistance in the saturation region of the IV curve.

The proposed mechanism of NDR is as follows. Carriers, which cannot easily transport to a barrier molecule, will be blocked from moving towards the drain electrode within the saturation region of mobility. This is because the probability to move towards the source is very low compared to other regions: the likeliest case is for the carrier to remain in place. For example, consider a system with no barrier, and an electric field of 0.1 V/nm. We can estimate the transport probabilities for a carrier by considering energy changes and using the Boltzmann factor with a coupling constant. Ignoring Coulomb interactions, the transport probabilities are  $P_{\text{right}}, P_{\text{up}}, P_{\text{down}} = 8.325\%$ ,  $P_{\text{left}} = 0.174\%$ ,  $P_{\text{stay}} = 74.85\%$ . If there is a tall barrier in front of the carrier, then  $P_{\text{right}} \approx 0\%$ . This raises the probability of the carrier staying in place to  $P_{\text{stay}} = 83.18\%$ . Although the energy change to move up, right, or down is negative, the probability is not 25% because the electronic coupling (a value of 1/3 is being used for demonstration) may not be perfect. This is one reason the probability to remain stationary is so high.

Coulomb interactions will reduce the probability for the carrier to remain in place in both cases. However, the probability for the carrier to stay put will remain higher when a barrier is present, because  $P_{\text{right}} \approx 0\%$ . When  $V_{\text{DS}}$  is lower (before the saturation region), the probability to

move backwards is increased. This has the effect of reducing the probability of the carrier remaining in place. For example, at 0.01 V/nm, the probability to move backwards increases to 5.654%. The net effect is that carriers are better able to move around the barrier and navigate to the electrode.

Because of these effects, increasing the voltage in the saturation region also increases the probability for carriers to remain in place. The carriers become entrenched behind the barriers since they cannot make it to the drain electrode, and the current decreases with increasing voltage: NDR. The same phenomenon will arise when sites are defective, or not allowing transport.

In short, Coulomb interactions can lead to a lessening of the negative differential resistance, as the slope of the IV curve in the saturation region will have smaller magnitude. The probability for a charge to remain behind a barrier is lowered with the introduction of Coulomb interactions, because the carrier must move against the field of other carriers to escape. However, the probability of other carriers to move near the blocked carrier is significantly reduced: from 8.325% without Coulomb interactions to 0.139% with interactions included. A carrier is much more likely to move around a blocked charge, increasing the likelihood that it will make it to the drain electrode and increase the overall current, thereby reducing the NDR.

### **2.3 CONCLUSIONS AND CONTEXT**

We explored the effect of barriers on the charge transport in organic semiconductors processed from solution. The AFM topography and FET conductivity measurements show that introduction of controlled amounts of barriers does not affect morphology or domain size, but the

conductivity changes significantly. It was found that even 2.5% of OBUnc introduced would decrease mobility by 90%, which is concurrent with the simulation of deep traps, barriers, and defects. Surprisingly, the shallow barriers in our experiments behaved more like the deep barriers predicted in simulation. Both the mobility and the emergence of NDR in experiments agree with the simulated prediction of high barriers. However, given the energy levels of the components, OBUnc should work as a shallow barrier in the charge transport between NiOBuPc molecules. While the cause of this discrepancy is unknown, it may be due to the introduction of shallow barriers affecting the crystal alignment and thus decreasing the electronic coupling in the system.

Based on this work, we draw two practical conclusions for organic semiconductors fabricated from solution. First, the introduction of a small amount of “impurities” can reduce the mobility significantly, so it is imperative to purify semiconductor solutions and fabricate defect-free devices. Second, if negative resistance is desired, there is no need to use photo-irradiation as reported previously<sup>32</sup>, it can be achieved simply using a similar mixture to that reported here.

This investigation also brings to light an interesting question. We assumed that there were homogeneous distributions of traps in the material based on the fact that height and phase scans measured via AFM showed no separated crystalline domains. While it is likely that grain boundaries would provide a source of traps in the film, is this the only possible source? Are heterogeneous traps conceivable from a nanoscale source not visible on a device scale, making our assumptions about disorder inaccurate in some real devices?

### 3.0 SURFACE POTENTIAL MAPPING IN STATIC, UNIMATERIAL FILMS

*This chapter was previously published as:*

Hoffmann, P.B., Gagorik, A.G., Chen, X., and Hutchison, G.R. “Asymmetric Surface Potential Energy Distributions in Organic Electronic Materials via Kelvin Probe Force Microscopy” *J Phys Chem C*, 2013, 117 (36), pp 18367-18374.

*All experimental data and analysis was performed by P.H. (including supplemental information provided in Appendix A), in addition to main writing of the manuscript. A.G. developed simulation models and helped with analyzing theoretical data, and X.C. contributed to experimental design. Simulation data was provided by G.H. along with contributions to the manuscript.*

Recent scientific and technological advances in the application of organic semiconductors for solar electric generation, displays, and other electronic devices have spurred a great deal of research into the rational design of materials<sup>33-36</sup>. A combination of experiment and theory is commonly used to investigate the complex relationships involved between all variables, including optoelectronic properties<sup>37</sup>, charge transport and trapping<sup>37,38</sup>, morphology<sup>39,40</sup>, interfacial effects<sup>41</sup>, and film thickness<sup>42</sup>. The underlying goal for all such experiments is to better understand and improve charge transport in organic semiconducting thin films.

Conventional charge transport theory relies on a variety of assumptions that have not always been directly tested, for example, the use of the Gaussian Disorder Model (GDM). This model was derived for low concentrations of conductive molecules embedded into a disordered insulating polymer matrix<sup>6</sup>, not the polycrystalline or crystalline ordered semiconductors now studied experimentally. Defining a more accurate model both computationally and with synergistic experiments for disorder in organic semiconductors will help our understanding of their charge transport processes and contribute to rational device design.

Kelvin probe force microscopy (KPFM) maps the surface potential of a thin film simultaneously with topography. It adds a second pass to the traditional AFM height scan and measures potential by nullifying the contact potential difference between the tip and the surface. This particular method is well suited to studying electronic properties because they can be investigated locally, with resolution in the x, y, and z directions on the sample. Though the method suffers from a reduced spatial resolution because of long-range interaction during the second scan pass<sup>43</sup>, the information has proven useful in many studies and will continue to be of use as researchers delve further into organic semiconductors. For example, KPFM has been used in recent works as a method for studying charge transport processes in OFETs<sup>41,44</sup> and diffusion lengths of photogenerated charge carriers<sup>45</sup>. More specifically, effects of disorder and trapping are also commonly studied via KPFM, from trap formation and photooxidation<sup>46</sup> to the effects of illumination and phase separation on electron transport and trapping<sup>47</sup>.

This chapter describes an investigation into surface potential energy distributions in organic semiconductor thin films. Films were deposited and scanned via KPFM. Histograms were then taken of the potential scans and compared to potential energy distributions calculated by a colleague via our simulation method. Results are reported then discussed in terms of

interactions between the distributions and material disorder, with implications outlined for the assumptions of disorder models in future organic semiconductor use and simulations.

## 3.1 EXPERIMENTAL METHODS

### 3.1.1 Sample Preparation

Substrates and materials were purchased from Sigma Aldrich and used without further purification, unless noted. Samples were dropcast from ultrapure water from a Millipore Synergy system (resistivity= 18.2 M $\Omega$ •cm) or chloroform (ACS certified, Fisher Scientific) solutions with approximate concentrations of 1 mg/mL onto indium-tin oxide (ITO) coated glass slides (30-60  $\Omega$ ). Terthiophene (3T) was purchased from Tokyo Chemical Industry Co. (MW 248.39 g/mol) and was also used without further purification. Sulfonated nickel (MW 979.4 g/mol) and copper (984.25 g/mol) phthalocyanine solutions (NiPs and CuPs, respectively) were purified after purchase using a mixed-solvent extraction of chloroform and water, where any organic impurities were removed in the organic layer. For additional substrate comparison, poly 3-hexyl thiophene (P3HT) was dropcast from chloroform onto single crystal quartz (SiO<sub>2</sub>) and single crystal magnesium oxide (MgO) substrates, in addition to a gold (Au) electrode. All substrates were cleaned prior to film deposition using an ultrapure water rinse, followed by submerged heating for 20 minutes and an acetone rinse, with similar heating for 20 minutes. The samples were then immediately used for deposition and were typically 30-50 nm thick, depending on the number of dropcast layers.

Multiple surface treatments were tested in addition to basic cleaning processes. This included using a UV-Ozone cleaner (Novascan PSD Pro 4 bench top) after regular cleaning, acid etching ITO before deposition/scanning and depositing a self-assembled monolayer (SAM) between substrate and material. Acid etching included sonication in 0.30M HCl for 20 minutes, rinsing with ultrapure water, drying with N<sub>2</sub> flow, and ozone cleaning. For SAM samples, substrates were submerged in an approximately 1 mg/mL silane solution, either trichloro(octadecyl) silane (TCOS) or 3-aminopropyl (triethoxy) silane (APTES), inside a glove box with <5ppm O<sub>2</sub> for 20 minutes, followed by a hexane rinse before deposition in ambient conditions. After being allowed to evaporate in a solvent-rich environment, the samples were stored in a vacuum environment until they were scanned, typically between 8 and 12 hours.

While P3HT, 3T, and PEDOT:PSS were deposited onto substrates via dropcasting, phthalocyanine (Pc) samples do not typically yield smooth enough surfaces for AFM testing if deposited in the same way. Because of this, the Pc samples included in the statistics above were deposited onto ITO slides via layer-by-layer electrostatic deposition<sup>48</sup>, where substrates are successively immersed in Pc solutions with alternating pH levels (3 and 11).

### **3.1.2 Sample Characterization**

AFM characterization was performed using an Asylum Research MFP-3D atomic force microscope. No modifications (i.e. vacuum or inert atmosphere) were made to the existing instrument hood; all samples were recorded in ambient conditions. The Electrilever AC240TM silicon tips with a titanium/platinum coating ( $k= 2 \text{ N/m}$  and  $f= 70 \text{ kHz}$ ) purchased from Asylum Research were utilized. Kelvin probe mode (KPFM) through the MFP-3D is frequency-modulated, with a default delta height (height of the lever above the surface during the potential

pass) of 40 nm. To ensure the electric isolation of the sample during the KPFM scan, a conductive atomic force microscopy (C-AFM) sample holder was used. The holder has two clips, which hold the sample in place but do not allow electrical contact from the substrate to the instrument unless one clip is attached to the scanning head. A wire connecting the clip to the cantilever holder provides a source of electrical grounding, which proved essential in the experiment. During scanning times, the temperature was recorded at the beginning and end of each scan, and the average change over approximately 35 separate sample runs is  $\pm 0.045$  °C per scan. Sample data was analyzed using the Asylum Research software (version 100729B) built into IgorPro (version 6.22A).

### **3.2 KPFM DISTRIBUTIONS: EMERGENCE OF ASYMMETRY**

Materials were selected for testing that have been extensively studied and/or are commonly used in organic devices to observe behavior common among many organic semiconductors. These include sulfonated nickel phthalocyanine<sup>49</sup> (NiPS), poly(3-hexyl)thiophene<sup>50</sup> (P3HT), terthiophene<sup>51,52</sup> (3T), and polyethylene dioxythiophene: polystyrene sulfonate<sup>6,42,53-55</sup> (PEDOT:PSS).<sup>6,51,53-56</sup> We also deposited P3HT onto several common substrates, including indium-tin oxide coated glass slides (ITO), single crystal quartz (SiO<sub>2</sub>), a gold electrode (Au), and single crystal magnesium oxide (MgO) to test variability of surface potential patterns with respect to substrate and/or substrate-material interaction. Histograms were then taken of potential scans via the Asylum Research software built into IgorPro. Example height and potential scans with a histogram are given below in Figure 3.1.

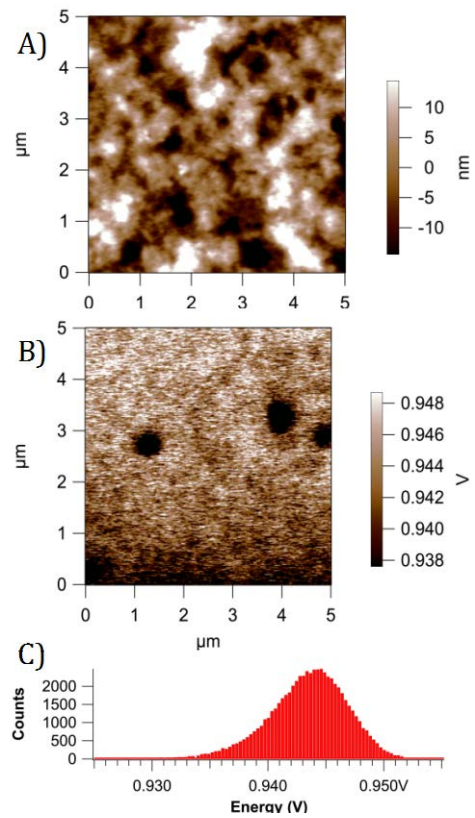


**Figure 3.1.** Representative height (a) and potential (b) scans and histogram (c) of the potential scan.

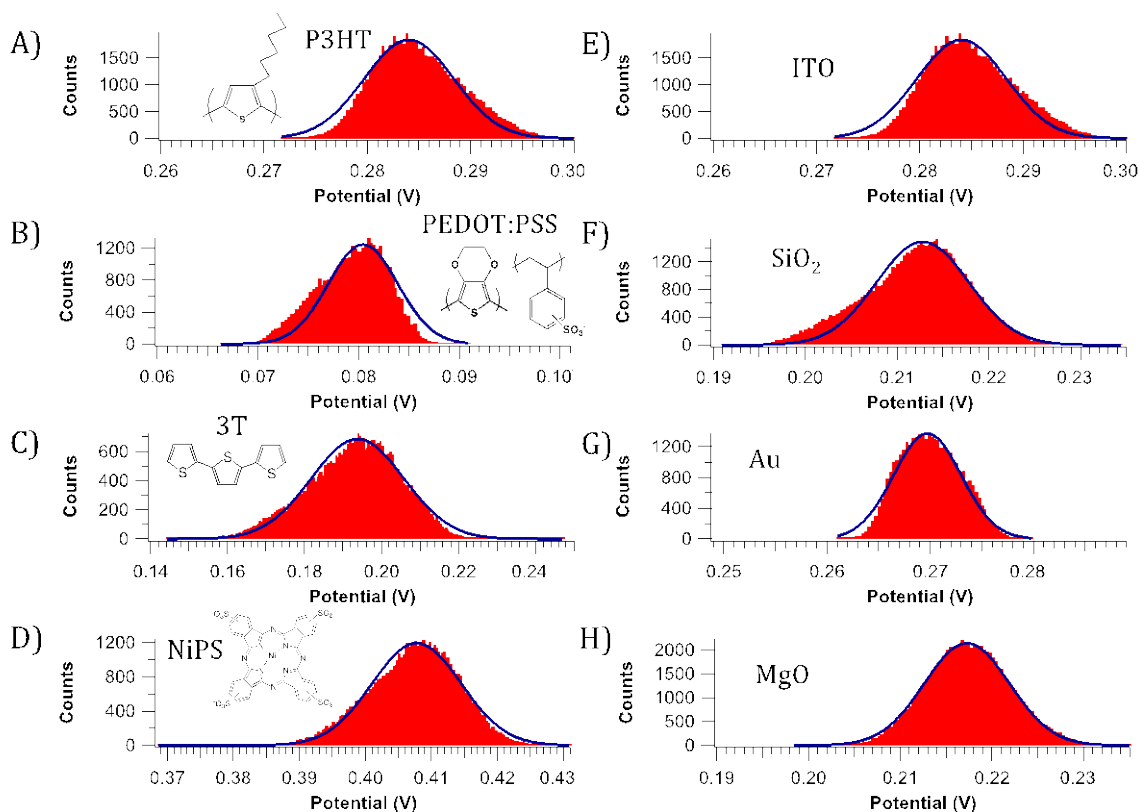


**Figure 3.2.** Representative histograms of surface potential scans obtained via KPFM for all materials and substrates. A-D) histograms of potential scans on varied materials as indicated (P3HT, PEDOT:PSS, 3T, and NiPS, respectively) and E-H) scans of P3HT on additional substrates for comparison with original ITO substrate samples (ITO, SiO<sub>2</sub>, Au, MgO, respectively). Gaussian distributions have been added to the histograms based on curve fitting from IgorPro to demonstrate inaccurate fits.

When taking histograms of the surface potential scans, normal, Gaussian distributions were expected due to typical disorder in a semi-crystalline organic semiconductor thin film.<sup>6,56,57</sup> This was not the case in at least 80% of samples scanned, seen in Figure 3.2 above, where the potential distribution showed a high degree of asymmetry. It can be imagined that the asymmetry is due to instrument artifacts like tip contamination or sample where. However, due to comparison to simulation models and to extensive control experiments, outlined in Appendix A,

we believe it is due to a unique distribution of charges during the scanning process and the effects of charge traps within the film and at the semiconductor-substrate interface.

To quantify comparisons between experimental samples, we calculated skewness and “skewtest” values for the potential distributions. Skewness is a measure of asymmetry via a comparison of the third moment about the mean and the standard deviation and is commonly used in tests of normality for sets of numbers.<sup>56-60</sup> Calculation of the skewtest for a distribution tests the following null hypothesis: that the skewness of the sample set is accurately represented by a Gaussian distribution.<sup>57-61</sup> In which case, a p-value of 1 for the skewtest shows that there is a 100% chance that the sample in question was taken from a population represented by a normal distribution. Calculated skewtest values are summarized in Table 3.1 below.

**Table 3.1.** Summation of KPFM Experimental Results

Substrate	ITO coated glass				ITO	MgO	SiO <sub>2</sub>	Au
Material	NiPS (LBL)	P3HT	PEDOT:PSS	3T	P3HT			
Samples with P<0.05 (%)	82	87	93	71	82	75	83	83
Total Samples	10	15	14	7	10	4	6	6

Though most samples had smooth morphologies, some samples (in particular dropcast phthalocyanines) displayed highly uneven potential distribution due to uniquely rough topography. To determine whether variation of the surface potential was caused mainly by topography, samples showing any real measure of correlation between height and potential scans (an  $R^2 > 0.25$ ) were removed from analysis. Thus, all samples in Table 3.1 had  $R^2$  values  $< 0.2$ . In all cases, these rough samples never comprised more than 30% of total prepared.

Skewness values for P3HT on SiO<sub>2</sub> were on average ~7 times larger than those of the MgO substrate (when absolute values are used), which indicates that initial asymmetry is typically greater for SiO<sub>2</sub> than for MgO. As both the MgO and SiO<sub>2</sub> used in this experiment are highly ordered single crystal substrates, the difference in the asymmetry presented here is likely not due to substrate morphology or film ordering at the interface. A difference, then, in the surface reactivity/functionality of the substrates most likely causes the substrate's effect on semiconductor behavior. More investigation is necessary to pinpoint the effects of each of these substrates film growth and properties.

Organic semiconductor interfaces are now known to have a high impact on charge transport in the organic layer and on device performance<sup>58-62</sup>, the extent of which, however, is still unclear. Because of this uncertainty, we tested multiple cleaning processes, interfacial layers, and surface treatments to determine their influence on surface potential. A summary of these interface tests is given below in Table 3.2.

The typical cleaning process for substrates prior to thin film deposition included rinses and heating with ultrapure water and acetone. However, it is possible that this process left organic contaminants on any of the substrates used. Because of this possibility, ITO substrates were cleaned via a UV-ozone cleaner prior to deposition of P3HT and scanned. Over 80% of samples cleaned with ozone displayed similar asymmetry to other samples. Representative scans and histograms can be found in the Appendix A.

Recently, Leever, *et al*<sup>61,62</sup> tested OPV devices on a variety of ITO surface treatments: an acid-etched ITO, cleaned but non-treated ITO, and a deposited PEDOT:PSS layer on top of ITO via atomic force photovoltaic microscopy (AFPM). With pixel averaged current maps, they determined that both the PEDOT:PSS layer and the acid etching reduced the photocurrent

variation in the devices significantly, with the acid etched devices showing the least variation of all three samples. However, when we deposited P3HT films onto ITO treated with the same acid etching process, asymmetric potential distributions were still apparent, as can be seen in figure 5.5. 75% of P3HT deposited on acid-etched ITO displayed a skewness  $P \leq 0.05$ . Scans of the acid-etched ITO itself, without any organic layer, have similar variation to the scan of an un-treated ITO sample (with 2/3 of samples having  $P \leq 0.05$ ), but the treatment does seem to reduce the degree of asymmetry in the potential distribution of a film deposited on top, as the average initial skewness for an acid etched P3HT sample was 0.342 versus a regular P3HT average of 0.639.

Many groups have also begun to investigate the influence of a self-assembled monolayer (SAM) deposited between the organic semiconductor and the substrate in organic thin film transistors (OTFTs)<sup>61,62</sup> to diminish the effects of traps and the effects of other surface treatments at the interfaces in organic photovoltaics (OPVs)<sup>60-62</sup>. Thus, we deposited P3HT onto two types of silane SAMs: trichloro (octadecyl) silane (TCOS) and 3-aminopropyl (triethoxy) silane (APTES), both assembled on ITO-coated glass. Though a monolayer between the substrate and organic semiconductor layer would change many aspects of the active layer's morphology and charge transport, previously witnessed asymmetry was still prevalent in all the monolayer samples tested: 75% of SAM samples showed a skewtest value of  $P \leq 0.05$  (an example of which is in figure 5.6). SAMs are typically thought to affect device performance through changes in semiconductor film growth morphology and/or interfacial properties (i.e., surface energy, injection barrier, or trap sites)<sup>3-5,60,62,63</sup> by changing the way in which the semiconductor is ordered at the interface or modifying the work function and charge injection of the interface<sup>3-5,60,63</sup>. Average initial skewness values of SAM samples were only 18% different than that of

regular P3HT samples. As such, the monolayer underneath the P3HT did not have a significant effect on the semiconductor film's surface potential and the asymmetry detailed here.

**Table 3.2.** Summation of Interfacial Test Results

Control Test	Before and After Deposition	APTES SAM	TCOS SAM	Ozone Cleaned ITO	Acid Etch
Samples with P<0.05 (%)	100	83	80	100	80
Total Samples	5	6	5	6	5

Many control experiments were performed to rule out behaviors caused by sample creation processes. The effects of tip contamination were analyzed by testing samples from the same deposition conditions using ozone-cleaned tips and tips coated in the material solution (visible after deposition), both in succession and on different samples. Contaminated tips, while having some affect on the appearance of some scans, neither diminished nor stimulated asymmetry in potential distributions. To ensure thermal drift was not affecting potential measurements over the long scan times utilized in these experiments, the first and last scans of several samples were analyzed to calculate an average drift ( $\leq 0.05$  nm/hr). Topographies were compared between AC/tapping mode and KPFM mode; height scans from the two modes displayed no discernable difference in topography. Also, an intentional bias was applied to a gold electrode in a set pattern to test the Kelvin probe mode's potential tracking. More detailed experimental results and figures can be found in Appendix A.

### 3.3 UNDERSTANDING ASYMMETRIC SURFACE POTENTIAL DISTRIBUTIONS: NANOSCALE HETEROGENEITY

Our group has developed a coarse-grained Monte Carlo hopping model to study charge transport in thin film OFETs and OPVs<sup>3-5,63,64</sup>. An important question in such modeling is the nature of energetic disorder, whether from charged defects, carrier-carrier interactions, or thermal broadening. At the same time, simple simulations should also allow deeper understanding of experimental results. For example, what is the fundamental cause of the asymmetric distribution of surface potentials in the KPFM scans?

Since thermal disorder will necessarily produce Gaussian broadening, one must assume the asymmetry derives from electrostatic disorder in the substrates and films. One possibility would be excess positive or negative charging. In the limit of purely homogenous distributions of positive and negative charges (whether carriers or charged traps / defects), an excess of one type of charge would force an asymmetry of surface potentials. Whatever the majority charge is, more sites would be biased in that direction. Such charging, however, is unlikely to persist in a grounded film over the timescale of minutes.

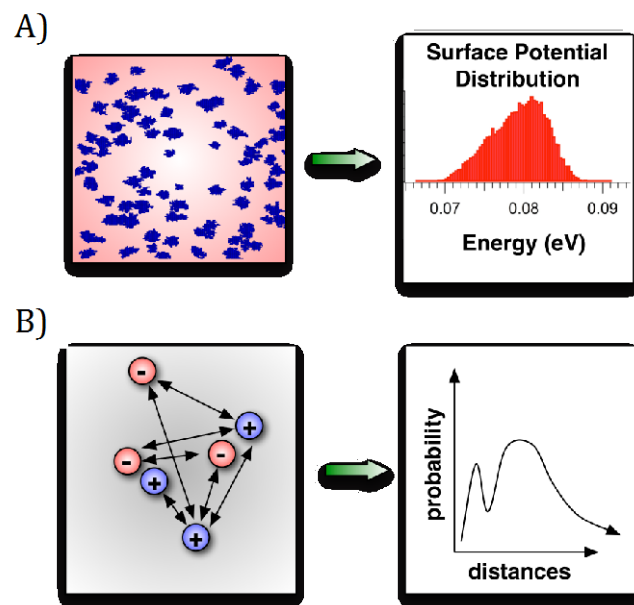


**Figure 3.3.** A) Schematic of heterogeneous islands of positive charge (blue) in a more homogeneous distribution of negative charges (red), leading to an asymmetric distribution of surface potentials. B) The heterogeneous spatial distribution of charges leads to a peak in short-range interactions.

An alternative explanation is a heterogeneous spatial distribution of charges. For example, if positively charged traps form nanoscale “islands” but the negatively charged traps are more homogeneously distributed through the film, as illustrated in Figure 3.3, there would be an increase in the probability of short-range positive-positive electrostatic interactions. Since the negative charges would be somewhat more homogeneously distributed, this imbalance would bias the distribution of chemical potential (and thus surface potential) in an asymmetric manner.

To model this effect, we developed a simple model of the electrostatic disorder due to charged traps or defects. We assume a square grid of molecules  $\sim 1$  nm in size, with the probe monitoring charges in a  $\sim 2$ -5 nm thick layer across the top of the film. Since we observed similar heterogeneity in bare substrates, the layer-by-layer phthalocyanine films, and various thicknesses

of the organic semiconductors, we believe this heterogeneity typically occurs throughout all films.

Equal concentrations of both positive and negative charges are placed into the grid with potentially different levels of spatial heterogeneity. A nonuniform, heterogeneous distribution of charge sites is achieved by first seeding the grid with a number of charges, followed by looping over the charge seeds to grow them into “islands” of trap sites. The fraction of seeds controls the spatial distribution of charge sites; fewer seeds create a more heterogeneous distribution.<sup>4,54,64</sup> For each positive and negative charge, a counterbalancing charge is embedded with the same X and Y position, but deeper into the film. For example, a positive charge trap is 0.9 nm below the surface, and a negative charge is 1.8 nm below the surface. This can be considered to model charge pairing, image charges or charge dipoles in the semiconductor. Similar effects are found without such counterbalancing charges, but the peak width is much wider without them. The potential energy at each site in the grid is then calculated by the electrostatic interaction with all charges using a relative static dielectric constant of 2.2, and adding Gaussian thermal noise (which has less effect than the electrostatic disorder in the simulations). Since such simulations are Monte Carlo, for all analyses below, five runs were performed with each set of parameters and statistics were collected for averaging and estimating standard errors.

In the limiting case of homogeneous distributions of both positive and negative charges, the simulated histograms of surface potentials show exactly Gaussian peaks, with the width (i.e., the standard deviation of the distribution of surface potentials) determined by the charge density. More charges lead to more energetic disorder, and hence, a broader distribution of site potentials.

With a distribution of spatially heterogeneous traps (e.g., positive charges) and more homogeneous opposing charges, the simulated histograms of surface potentials show clear

asymmetric skew, much like the experimental KPFM results (Figure 3.4). In general, both experimental and simulated skewed peaks fit poorly to either Gaussian or Lorentzian fits, but are fit well by a Voigt profile, representing a convolution of homogeneous (Lorentzian) and inhomogeneous (Gaussian) disorder.

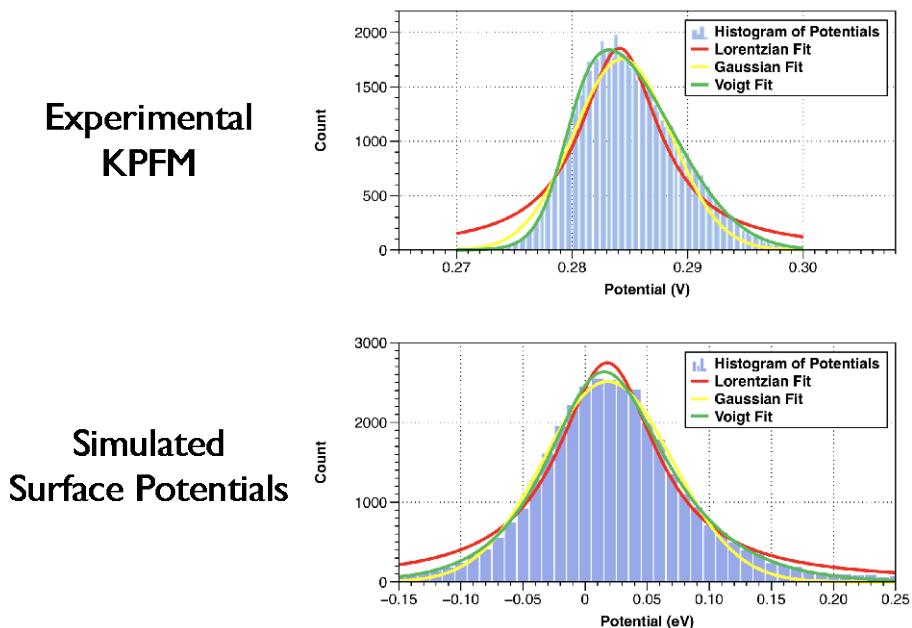


**Figure 3.4.** (top) Histogram of experimental KPFM surface potentials from a P3HT/ITO film in Figure 2, illustrating asymmetry, and a best fit from a Voigt model of mixed Gaussian and Lorentzian disorder and (bottom) simulated surface potentials from a heterogeneous spatial distribution of positive charges and a more homogeneous distribution of negative charges. The skewness (asymmetry) of both distributions is similar.

Using the nanoscale simulations, we find that the peak potential of the asymmetric distributions shifts with increasing charge concentration and with increasing heterogeneity (Figure 3.5A, B). The asymmetry of the distribution, measured by the skewness, also increases with increasing heterogeneity, but saturates with increasing charge concentration. After a threshold of 2% of sites with positive charges with heterogeneous spatial distribution and 2%

of sites with negative charges and a homogeneous spatial distribution, increasing the charge concentration with constant heterogeneity only serves to increase the width of the peak.

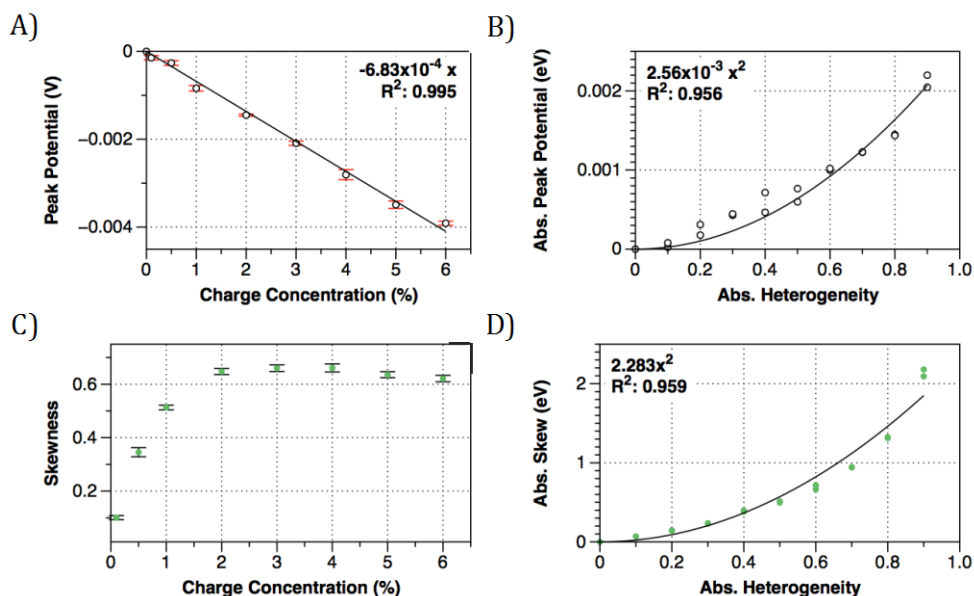


**Figure 3.5.** Compilation of Monte Carlo simulations of surface potentials as a function of heterogeneous spatial distribution of charge traps. A) Change in peak potential as the concentration of positive charges increases (with matching increase in negative charges), B) change in peak potential as the spatial heterogeneity of positive charges increases with constant charge concentration, C) saturation of asymmetric skewness with increasing concentration of positive charges, and D) change in skewness with increasing spatial heterogeneity.

Our simulations suggest that the most likely cause of the asymmetric distribution of surface potentials is nanoscale heterogeneity of charges. Since the “islanding” of like charges in the simulations would be on the 5-10 nm scale, they would not be directly observable via conventional KPFM used here. The Voigt profile is an excellent fit, since it models a mixture of homogeneous and heterogeneous electrostatic disorder, exactly as suggested by our simulations. It has been used successfully in other KPFM studies in organic semiconductors.<sup>54,64</sup> Finally, the

simulations suggest that as charge traps are discharged (i.e., the charge concentration in the film decreases), the asymmetric peaks will become purely Gaussian.

### 3.4 CONCLUSIONS

The interplay of disorder and charge transport with potential energy is a complex problem, and the study outlined in this chapter just began to scratch the surface of the pertinent property relationships. Further study was required to begin to understand exact causes of the asymmetry in the potential energy distributions and their relationship to macroscale sample properties. This evolved into two continuing studies, introduced below and detailed in the next two chapters.

During initial scanning of the material samples via KPFM, multiple scans in succession were performed to compare evolving potential energy distributions with initial scans. As a result, both a change in the shape of the distribution and its magnitude became evident with long scan times, on the order of 1-2 hours. An investigation of this phenomenon is described in Chapter 4.

In addition, it was suggested that phase separation and/or grain boundaries were responsible for witnessed asymmetry in potential energy distributions. Therefore, patterned, dual-component films were deposited and tested via KPFM as well, with a variety of patterns and sizes. These samples were then evaluated and compared to morphological parameters. This set of experiments is explained in Chapter 5.

#### 4.0 TIME EVOLUTION OF ASYMMETRIC POTENTIAL DISTRIBUTIONS

The organic semiconductor films described in the previous chapter produced asymmetric surface potential energy distributions (calculated via histogram of the KPFM potential scan) that were consistent among all materials tested during the first scan. Based on those experiments, it is likely that heterogeneous charge traps are the origin of the asymmetry in surface potential. Previous studies have investigated the kinetics of trap discharge using a variety of spectroscopic techniques. Most commonly, single molecule spectroscopic techniques with electronic modification are used to investigate devices<sup>65</sup> and controlled systems<sup>66</sup>.

For example single-molecule spectroelectrochemistry (SMS-EC) was developed in 2006 and uses fluorescence spectroscopy to measure electrochemical kinetics on a molecular scale. To do this, the fluorescence intensity of a single molecule as a function of time is measured while simultaneously scanning the potential of the working electrode of an electrochemical cell, yielding localized electrochemical variables instead of ensemble averages.<sup>67</sup> This was later utilized to investigate the oxidation of nanoparticles of a conjugated polymer system with a controlled charge injection setup.<sup>66</sup>

For further exploration of the mechanism witnessed in previous experiments, the original KPFM experiments were extended and performed over long time scales to determine the time evolution of the potential distributions in the materials. Though Kelvin probe AFM has not been frequently used for an investigation of this type of phenomenon, it has been consistently used to

examine charge trapping and dissipation in a variety of systems.<sup>68-71</sup> Its combination of spatial resolution with electronic measurements, similar to other electronic modes, makes it ideal for resolved trapped charge mapping in these materials. In addition to KPFM, other AFM modes have been utilized to resolve time-dependent behavior of charge trapping in similar materials. For instance, electrostatic force microscopy (EFM) is a technique similar to KPFM, but it measures the force on the cantilever exerted by the electric field around the sample. A custom-built EFM has detected the presence of charge traps in pentacene via changes in the contact potential, and inhomogeneous charge traps were observed not only at the grain boundaries, but throughout the bulk film.<sup>72</sup> Further studies of trap formation in pentacene transistors yielded potential data not well fit to either first- or second-order kinetics. This suggested that trap formation follows a series of steps not well modeled by a single, rate limiting reaction.<sup>73</sup>

In this related work, films of P3HT and PEDOT were scanned multiple times over approximately 1-2 hours via KPFM in the same location, a change in the distribution became evident in most cases. The distributions changed to a more normal, Gaussian distribution within 2-5 scans (20-50 minutes of scanning time). In addition to changes in the potential distribution's shape, the magnitude of the potential changed as well. A "drift" in potential was evident in most (>75%) samples scanned, though the direction of the change appeared to have little predictability. For Figure 4.1 below, histograms were taken of successive potential scans for the same sample in the same location and graphed together for comparison.

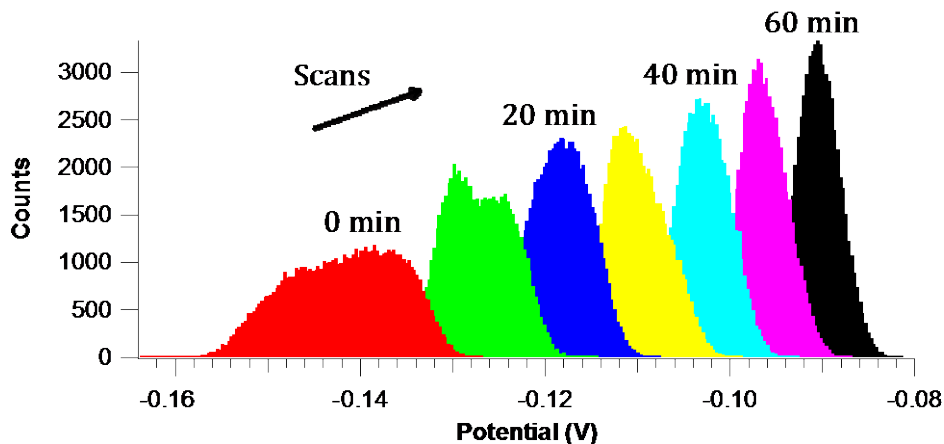


**Figure 4.1.** Histograms of the surface potential scans for a PEDOT sample graphed in succession. Each scan took approximately 10 minutes for a total of 120 minutes of scan time.

As is described below, we believe that the cause of both the changing potential distribution shape and magnitude is the charging/discharging of traps within the semiconductor film. This conclusion comes primarily from comparison to theory and control experiments to evaluate the effects of instrument artifacts. Interestingly, while some traps may persist at the semiconductor-substrate interface, we are confident that the charging and discharging of traps in the bulk film is responsible for this effect. Of note, all material film samples described here were prepared according to the description given in Section 3.1.1 (Sample Preparation).

## 4.1 PROPOSED MECHANISM

### 4.1.1 Comparison to Theory

Chapter 3 results suggest that, as the charge concentration decreases (i.e. the charged traps discharge to ground), the distribution of surface potential becomes more Gaussian and less

asymmetric. We believe that the changing shape of the potential distribution with long scan times is congruent with our simulations, that the discharging of traps (or a similar process) is the cause. In particular, this can be seen in Figure 3.5, which summarizes the relationship of both the skewness and the peak potential with heterogeneity and charge concentration. It is evident that as the heterogeneity of charges and the charge concentration (<2%) increase, so does the calculated skewness of the potential energy distribution. Concurrently, the peak potential calculated also changes as a function of the heterogeneity and charge concentration, though in inverse relationships.

#### **4.1.2 Instrument Artifacts**

While it is commonly accepted that AFM is susceptible to changes in temperature and humidity, we believe that there are other factors causing the bulk of this behavior. Temperatures during long scan times (~2 hours) in these experiments did not vary by more than 1-3 °C. Thus, though it is possible that variations in temperature do affect the overall drift in potential, the effects are not likely to be a main cause. Explicit effects of changes in temperature and environment are key questions for future studies.

In previous measurements, the only source of electrical grounding was the intermittent tapping of the metal-coated cantilever in AC mode (typically samples are not grounded for simple KPFM scans, though all the samples presented here were grounded). After intentionally grounding samples through the instrument controller via the sample holder clamp, the changing shape and shifting magnitude of the potential distributions became generally faster and more evident, though this was noted by researchers and not measured quantitatively. An acceleration of these behaviors with the introduction of a source of grounding further lead to the conclusion

that the effects witnessed were a discharge mechanism, most likely the removal of charges from various traps in the film.

### **4.1.3 Interfacial Traps**

To investigate whether charged traps persisted only at the interface, uncoated ITO films were scanned with KPFM while grounded, followed by P3HT film deposition and additional KPFM scanning. In principal, if charges were trapped on the surface of the ITO slide and asymmetry is caused by interfacial trapped charge, grounding and scanning the substrate before film deposition would remove trapped charges (many, if not all) and substantially affect the asymmetry witnessed in previous samples. While varying pre-deposition discharge times (20 min versus 100 min, Figure 4.2) affected the changing shape over time, initial asymmetry in the P3HT potential distribution persisted, suggesting interfacial effects are not a major cause for the asymmetry.

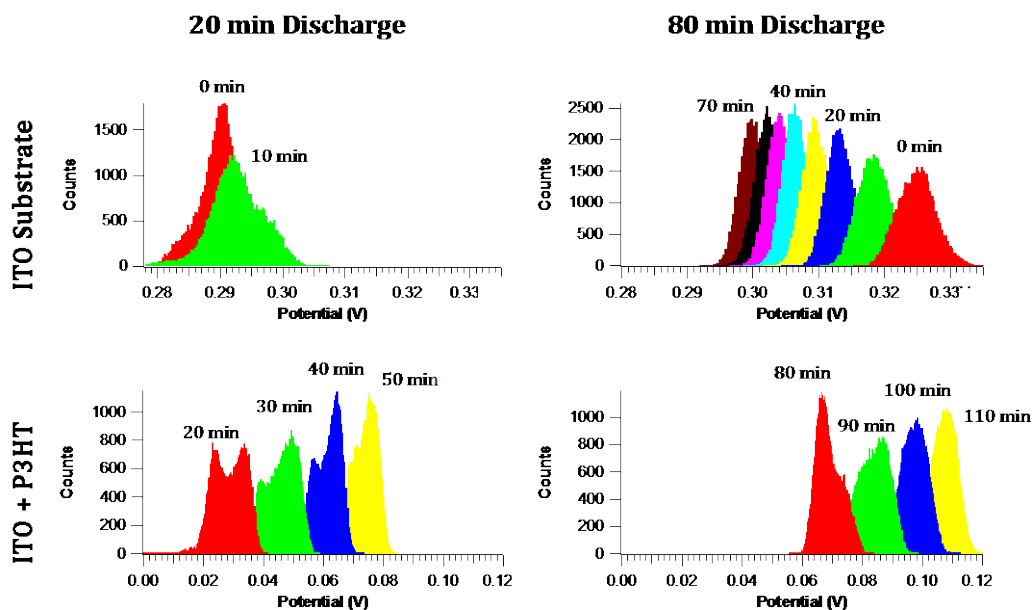


**Figure 4.2.** KPFM histograms indicating effects of discharging ITO substrates before deposition of P3HT. (left) Potential scans with a discharge time of 20 minutes and (right) with a discharge time of 100 minutes before measurement.

In Figure 4.2, two time intervals were used to discharge possible traps on the ITO surface before deposition: 20 minutes and 80 minutes. Longer discharge of the substrate produced a quicker reduction in asymmetry for the material after it was deposited and scanned, as indicated in Table 4.1.

**Table 4.1.** Control test for interfacial traps: summation of skewness values for samples where substrates were discharged before material deposition.

<b>Sample</b>	<b>Skewness of material, Scan 1</b>	<b>Skewness of material, Scan 4</b>	<b>Change</b>
20-min Discharge	-0.636	-0.235	+0.4
80-min Discharge	1.082	0.012	-1.07

Interestingly, both samples retain a high degree of initial skewness after deposition of P3HT. This implies that traps at the interface have an effect on evolving asymmetry in the distributions over time, but not on the occurrence of initial asymmetry. The absolute value of the skewness in the first scans after deposition of material is likely caused by disorder within the film itself. It is also possible, though, that this disorder is affected by interaction of the organic semiconductor with the substrate (traps and/or morphology), as some substrates showed a lower degree of initial asymmetry than others.

## 4.2 DISCUSSION

As the films tested here are likely semi-crystalline, with areas of higher and lower degrees of order, it is possible that their energetic disorder has multiple forms or an evolving nature. McMahon and Troisi<sup>54</sup> described the presence of static and dynamic disorder regions caused by varying degrees of morphological order and crystallinity in organic semiconductors, which are categorized by their timescales relative to charge transport in the sample, with static disorder on the timescale of charge hopping and dynamic disorder evolving faster. The presence of two types

of disorder is a feasible explanation for these dropcast films also, as they would have areas of higher and lower crystallinity. Though the timescales of the static and dynamic disorder regions were not estimated, the time scale in these experiments (i.e. hours) is likely much longer. This implies that there is varied disorder on multiple energetic levels: shallow and deep traps. This is not unlike data reported by Kaake and coworkers<sup>74</sup> where they described a two-tiered electronic energy landscape, with one due primarily to topography and the other to intrinsic defects.

During the discharge process over long scan times, we see an interesting correlation with this sense of two disorder regimes: many of the samples tested exhibit two distinct regions of potential movement, an initial rate that is quite rapid which is followed by a slower section in the same direction. In Figure 4.3 below, the plot in B) was created from the potential histograms graphed together in A), whereby the potential was estimated at the highest count and plotted versus time. In this way, we can see a time-evolution of the magnitude of the surface potential.

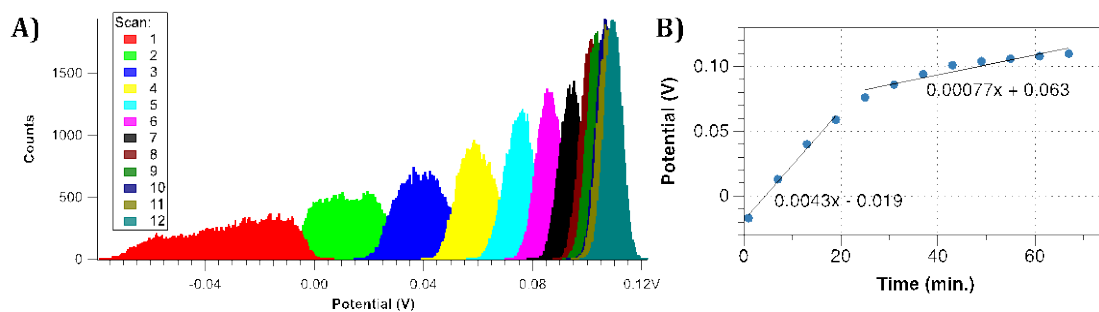


**Figure 4.3.** A) Histograms of surface potential energy scans graphed together for comparison. Each scan took ~6 minutes for a total scan time of ~70 minutes. B) Potential at highest count value for each of the histograms in A) graphed as a function of scan time.

Attempts to model the potential-time plots were largely inaccurate. First, a variety of fits were utilized, including exponential, power, linear, and quadratic functions, each providing an

inaccurate fit for part or all of the data. Second, kinetics plots were created to test first and second order rate laws. For example, if the data produced a correlated linear relationship with a plot of the natural log of potential versus time, we could assume first order. A majority of samples produced a curved distribution for both first and second order plots (examples in Appendix Figures 15 and 16). The lack of consistent fits for the sample data indicated that the two distinct regions of potential shift necessitated a dual fit. Examples of the fits used are given below in Figure 4.4. Thus, two equations were used to fit each sample.

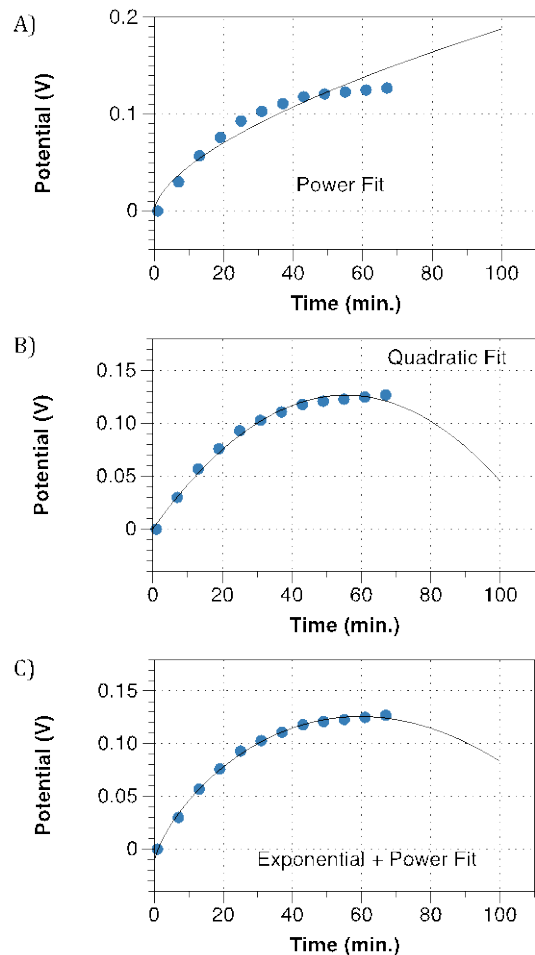


**Figure 4.4** Figure showing example fits attempted for the data presented in Figure 4.3. A) Power, B) quadratic, and C) a combination of exponential and power function fits were utilized, but none presented an accurate representation of the data and its projection into longer time scales. Fits were extended to 100 minutes to determine whether longer time scales would be well represented by the function.

As can be seen in Figure 4.3, a linear fit in each region was used. The data, though not a perfect linear relationship (as evidenced by the cured ends around the fit line in the figure), are approximated by the fits to estimate a rate of discharge in each region. To that effect, rates were determined for all of the samples tested (~15 total, including P3HT and PEDOT samples) for each of the two regions of discharge via the slope of each fit. Among them, the initial discharge region is labeled as shallow disorder, as it discharges much more quickly, while the plateau

region is labeled as deep disorder. These were calculated in mV/min, and the average rates of discharge are given in Table 4.2. Rates at this stage of experiments are preliminary, as evidenced by the high relative error. A more thorough investigation of all materials is necessary to draw concrete conclusions about the rates of discharge.

**Table 4.2.** Summary of long time scale scans for P3HT and PEDOT samples.

<b>Disorder Regime</b>	<b>Average Rate, P3HT (mV/min)</b>	<b>Average Rate, PEDOT (mV/min)</b>
Shallow	$1.1 \pm 0.3$	$1.6 \pm 0.7$
Deep	$0.31 \pm 0.08$	$0.33 \pm 0.1$

There is certainly some degree of topographic equilibration during long time scales in addition to the changes in potential. Though it is not believed to have a profound effect on the potential histograms, topography is likely to have some small effect on the potential maps created in each scan. In an effort to resolve the extent to which the topography of the sample affects its potential, height and potential scans throughout a long time scale (14 scans, ~2.5 hours) were qualitatively compared.

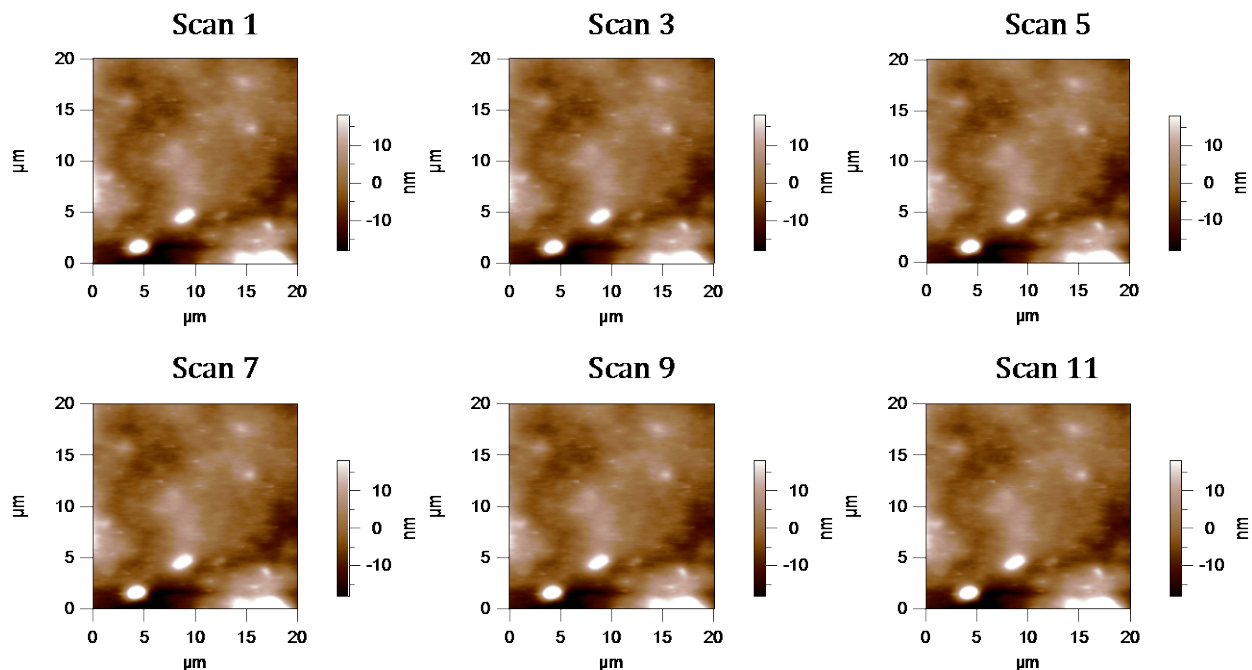


**Figure 4.5** Height images for a PEDOT:PSS sample scanned over a long time frame (11 scans, ~2 hours) in the same place.

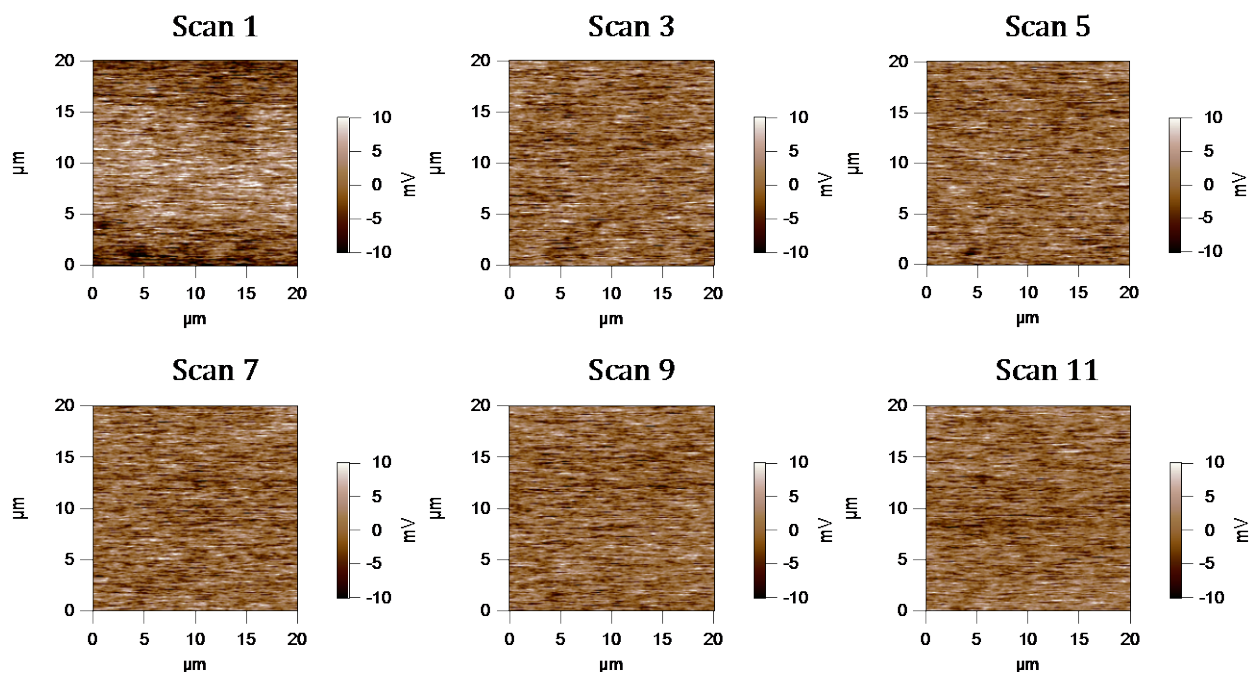


**Figure 4.6** Potential images for a PEDOT:PSS sample scanned over a long time frame (11 scans, ~2 hours) in the same place.

As evidenced by Figures 4.5 and 4.6 above, the progression of the height and potential scans for long time scales is fairly similar. The topography scans above show little to no changes in features, heights, and ranges over a scan time of two hours. There is a slight change evident early in the potential scans, from scan one to scan 3, but the potential map remains quite similar beyond the third scan.

The changing shape of surface potential distributions over long time scales (i.e. hours) is most likely due to dynamic pathways within the film. As traps are filled or discharged, Coulomb interactions between charges moving throughout the film or across the semiconductor-substrate interface affect pathways available to other charge carriers. For instance, a trapped charge would screen other carriers of the same sign and force them into other pathways, but would attract carriers of the opposite sign and create charge islands with a resultant increase in heterogeneity. In fact, Hallam, *et al.*<sup>68</sup> described a dual time scale for the recovery of their highly ordered polymer FET samples after the application of a gate bias stress for 60 min. While devices initially recovered to approximately 65% of their original current value within a few minutes, the devices further recovered to around 80% over the following 4-6 hours. This suggests the presence of deep traps in working transistor devices with ordered domains between well-defined grain boundaries. The presence of two energetic depths, both shallow and deep, also fits with the well-defined regions of potential shift in Figure 4.3B above, and this phenomenon was seen in a vast majority of samples tested (>90%).

The presence of two disorder regimes seems a likely explanation for the two time regions of discharge noted in long scan times. Dynamic disorder caused by heterogeneous charged traps is likely the main cause of the asymmetric distributions. Morphology plays little to no role, as

evidenced by Figures 4.5 and 4.6 above. If features in the topography affected the energetic distributions, potential scans would show a degree of correlation with those features. Exact causes of the heterogeneous charge distribution are cause for future study.

### 4.3 CONCLUSIONS

Trap kinetics in organic semiconductors is not well understood. Similarly to results determined for pentacene by Jaquith, *et al.*<sup>73</sup> the time evolution of surface potential observed for P3HT and PEDOT:PSS samples was not well modeled by expected means: potential as a function of scan time was ill fit by both first- and second- order kinetics plots. In addition, a variety of function models were tested, but none provided an accurate model for the data. No single model fit both regions of the potential shift in plots of potential versus time described here. The two discharge regions in the plots are likely representative of dual disorder regimes, with traps at varied energetic depths. This is an interesting addition conclusions presented previously, that heterogeneous charge traps are persisting within the film and causing the asymmetry in potential energy distributions. Charge distribution appears to be heterogeneous in energy as well.

## 5.0 INTERPLAY OF MORPHOLOGY AND ELECTRONIC PROPERTIES IN DUAL-COMPONENT, PATTERNED FILMS

The relationship between electronic and morphological properties in organic devices has been of particular interest for a number of years, and in that time, there has been extensive research into the ideal for each device<sup>75-77</sup>. For instance, the simplest and first developed morphology of organic photovoltaics from a device creation standpoint is a bulk heterojunction<sup>78,79</sup>, where both the electron donor and electron acceptor materials are interspersed isotropically through the active layer in pseudo-random fashion. This provides a high percentage of grain boundaries in the material at which excitons have energetic favorability to separate and produce current. Unfortunately, this type of morphology also yields very complex pathways to the electrodes for the separated charges, increasing the likelihood of loss mechanisms along the way. The challenge then becomes finding the morphological sweet spot where charges are separated consistently and within the right timescale after photon absorption and they also get to the electrode quickly and easily, avoiding recombination along the way. Investigations to identify ideal morphologies are common for many material combinations and devices<sup>80,81</sup> and they are also commonly treated via simulation<sup>63</sup>.

The picture becomes even more complicated on the nanoscale for charge transport properties. With a high degree of phase separation and grain boundaries, the system is much more disordered with higher occurrences of defects in many forms, like chemical impurities or

physical defects. Interfaces are thought to cause a high degree of energetic traps<sup>82,83</sup>, and there are many interfaces in an organic device: between the two materials, between two different phases of the same material, between either/both of the materials and the substrate or surface treatment layer, etc. In addition, as concluded in Chapter 4, it is likely that energetic traps persist not only at interfaces, but also in the bulk of the film and at its surface.

After the study detailed in Chapter 3, it was suggested that the asymmetry seen in the potential energy distributions was actually a combination of two Gaussian shapes and was likely caused by morphological disorder. The goal of this study was to identify whether morphology was a root cause of the asymmetry by intentionally creating phase-separated, two component films and measuring their surface potential distributions via KPFM. Thus, the distributions of various patterned films could be compared to those of single material films and establish whether the asymmetry was affected.

## **5.1 STRATEGY: INTENTIONAL PHASE SEPARATION AND GRAIN BOUNDARIES BY MATERIAL PATTERNING**

### **5.1.1 Experimental Methods**

Two different methods of patterning film samples were attempted for these experiments: directed and imprint patterning. The difference in the two approaches comes from the main method of pattern assembly. In directed patterning, differences in surface energy are utilized to preferentially direct materials to one area of the film or another. In the papers used as a guide,<sup>84,85</sup> carboxylic acid groups contrasted with alkyl chains in lined patterns to direct

P3HT/PCBM from spin-coated solutions. It was predicted that P3HT would preferentially order on top of carboxylic acid groups while PCBM would prefer alkyl chains, due to both energetics and size constraints.

In contrast, imprinted patterning outlined by Avnon<sup>86</sup> involved the transfer of a pattern from a polydimethyl siloxane (PDMS) stamp to a P3HT film that was dropcast onto an ITO slide. Then, PCBM was spin-coated on top of the patterned P3HT film where it would drop into recesses in the pattern. The experimental methods of these two processes are described below.

*Characterization:* (also previously outlined in Chapter 3)

AFM characterization was performed using an Asylum Research MFP-3D atomic force microscope. No modifications (i.e. vacuum or inert atmosphere) were made to the existing instrument hood; all samples were recorded in ambient conditions. The Electrilever AC240TM silicon tips with a titanium/platinum coating ( $k= 2 \text{ N/m}$  and  $f= 70 \text{ kHz}$ ) purchased from Asylum Research were utilized. Kelvin probe mode (KPFM) through the MFP-3D is frequency-modulated, with a default delta height (height of the lever above the surface during the potential pass) of 40 nm. Sample data was analyzed using the Asylum Research software (version 100729B) built into IgorPro (version 6.22A).

*PDMS Stamps:*

PDMS stamps were created using an elastomer base and curing agent mixed in a 10:1 ratio by weight (Sylgard Elastomer Kit, Fisher Scientific). The two components were mixed together, stirred rapidly, and allowed to degas in a desiccator for approximately 30 minutes. The mixing process was then repeated to ensure adequate incorporation. Then, PDMS solution was

deposited on the master (diffraction grating or patterned wafer piece) and cured in an oven at ~60 °C for 1.5-2 hours. After creation, the stamps were stored in a desiccator until use.

Stamp masters included a variety of patterns: 1  $\mu\text{m}$  lines, 2  $\mu\text{m}$  lines, 1  $\mu\text{m}$  dots, 2  $\mu\text{m}$  dots, and 5-pointed star designs. The line pattern masters were diffraction gratings purchased from an optics company with 1000 and 500 lines per  $\mu\text{m}$ . During stamp creation, PDMS material was allowed to fill the voids in the diffraction pattern, which created the stamp pattern. Due to the nature of diffraction grating (Figure 5.1), the line stamps created from it are not flat lines but jagged points. Resultant stamps could sometimes disfigure or collapse during the patterning process, making them difficult to obtain consistent patterns from.



**Figure 5.1.** Side-view diagram of the edges of diffraction grating from which the lined stamps were made.

Diagrams of all stamps utilized are shown below in Figure 5.2. The dots and star patterns were created from a wafer obtained from the NanoTech User Facility (NTUF) at the University of Washington. Designs were drawn in a CAD program for all stamp patterns from which a mask was created for the photolithography process and a silicon wafer stamp master was created. More information on this process can be found on the University of Washington's website.<sup>87</sup>

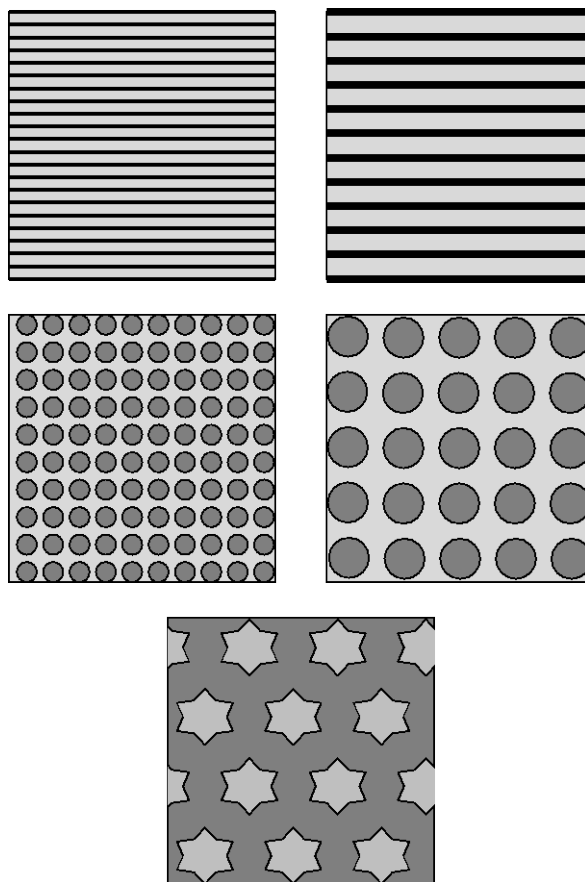


**Figure 5.2.** Diagrams for the stamp patterns used in this experiment. They include 1 and 2  $\mu\text{m}$  lines, 2 and 5  $\mu\text{m}$  dots, and 6-pointed stars measuring approximately 6  $\mu\text{m}$ . Dark colors in the figure are voids, meaning that the stars are actually voids in the resultant stamp while dots and lines are features in the stamps. Both positive and negative star stamps were created and utilized during the experiments, but this is the only pattern for which negative stamps were made.

### *Directed Patterning*

Samples for directed patterning utilized PEDOT:PSS films that were dropcast from ultrapure water obtained from a Millipore Synergy system (resistivity= 18.2  $\text{M}\Omega\cdot\text{cm}$ ) as a base. These films were deposited on a hotplate with a reservoir of ultrapure water and gentle heating of the solvent overnight to ensure smooth films.

Patterns were deposited onto PEDOT films via micro-contact printing ( $\mu$ CP). Two different silane materials were utilized for patterning: 3 amino-propyl triethoxy silane (APTES) and trichloro octadecyl silane (TCOS). Silane solutions were dropped onto PDMS stamps inside a glovebox under nitrogen atmosphere and allowed to wet the stamps for approximately 15 minutes. Stamps were then briefly dried by pipetting excess solution off the stamp and allowed to dry for 5 minutes. Finally, stamps were overturned onto PEDOT films and pattern transfer was executed for 20 minutes. Samples were then removed from the glovebox and stored in a desiccator until testing occurred.

### *Imprint Patterning*

Samples for imprint patterning were made from poly (3-hexyl) thiophene (P3HT) and phenyl-C61-butyric acid methyl ester (PCBM) (Fisher Scientific, 99%), both of which were used without further purification. P3HT was dropcast from chloroform (ACS certified, Fisher Scientific) with an approximate concentration of 1 mg/mL onto indium-tin oxide (ITO) coated glass slides (30-60  $\Omega$ ).

Patterns were imprinted into the P3HT films from the stamps via heat and pressure over a period of 3 hours in a vacuum oven. The temperature in the oven was  $\sim 110$   $^{\circ}\text{C}$  and the stamp and sample together were placed under a 2 kg balance weight (VWR International). Paper towel was placed around the weight to ensure the flat pressure on the stamp for equal pattern transfer. After imprinting, films were allowed to cool and stored in a desiccator for at least 30 minutes prior to PCBM deposition.

A few drops from a Pasteur pipette of PCBM solution (5 mg/mL in DCM) was spin-coated onto patterned P3HT samples at  $\sim 500$  rpm.

## 5.1.2 Results of Patterning

### *Directed Patterning*

As can be seen below, directed patterning proved largely unreliable. Major challenges occurred with wetting the PDMS stamps and with transfer of the silane material completely onto the PEDOT surface. In Figure 5.3 below, APTES was stamped on to a PEDOT surface for both samples, and incomplete pattern transfer is clear. This issue is also marked by the fact that the each sample was tested in several places (~10 cm apart), but this was the only one with any silane transfer. All of the samples tested in this way exhibited similar issues with varying degrees of pattern transfer. Because the lined stamps were made with diffraction grating, the shape of the protruding lines was sloped as described in Figure 5.1. This created a unique issue for use in  $\mu$ CP: if the stamp was left on the sample too long, the lines compressed and created patterns like those seen in Figure 5.3B.

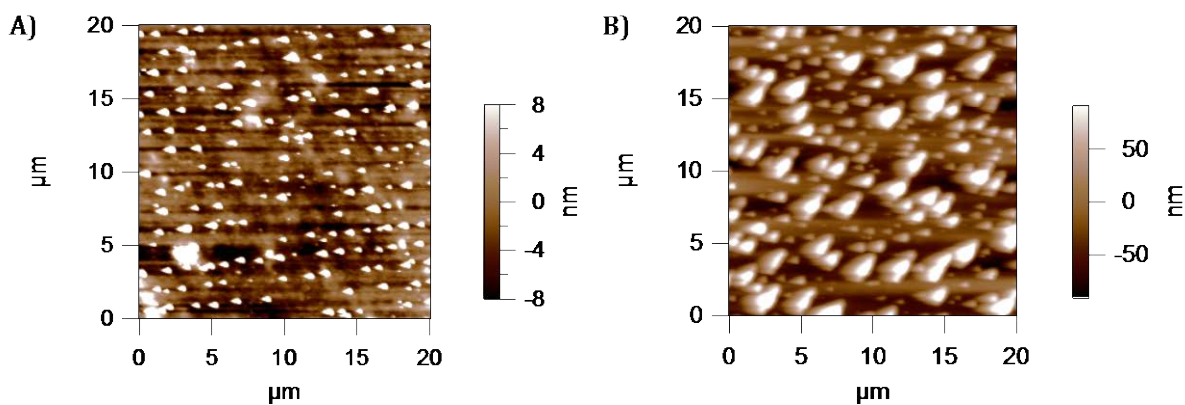


**Figure 5.3.** In both A) and B) above, APTES (aminopropyl triethoxysilane) was stamped onto PEDOT:PSS films via microcontact printing. Both of these images demonstrate an incomplete pattern transfer from the PDMS stamp to the sample surface, which was witnessed in most attempts of this patterning method.

### *Imprint Patterning*

Pattern transfer with all different types of PDMS stamps patterns was evident through imprint patterning. In the figures below, topography scans are displayed after the imprinting of the patterns but before the PCBM deposition via spin coating. Samples films were always tested via AFM before PCBM deposition to ensure consistent pattern transfer.

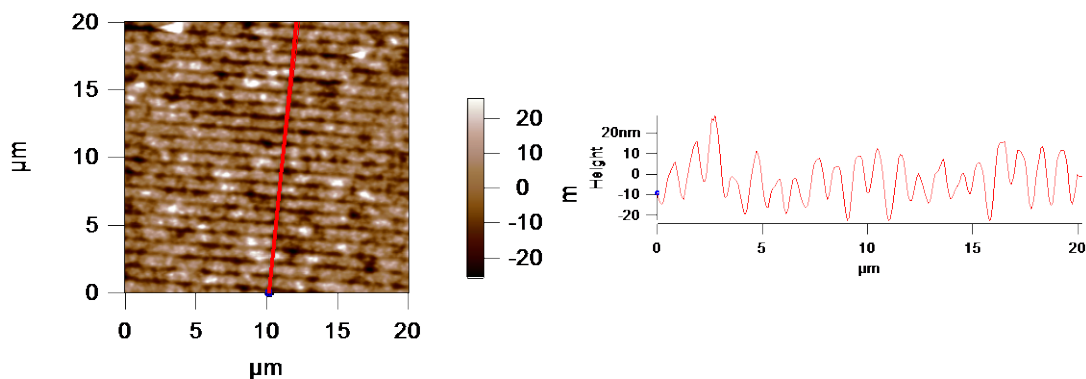


**Figure 5.4.** Height scan and line trace for 1  $\mu\text{m}$  line P3HT sample. These stamps had line patterns small enough that the patterning was consistent without much spreading of the PDMS during the stamping process.

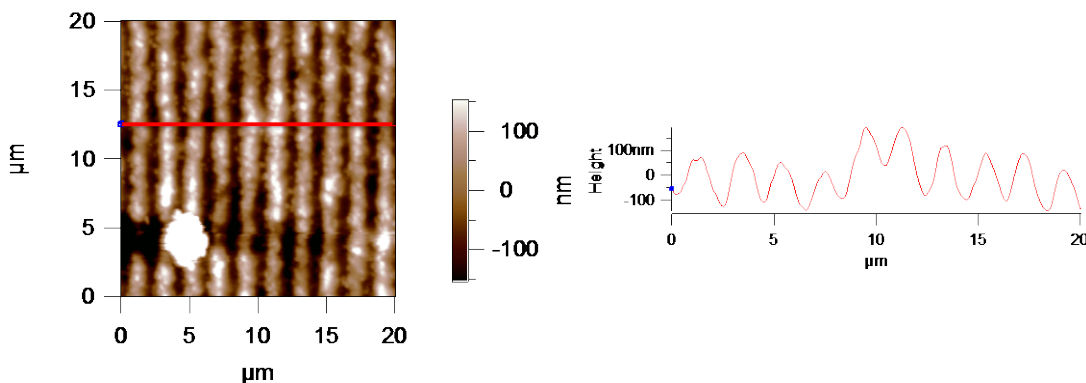


**Figure 5.5.** Height scan and line trace for 2  $\mu\text{m}$  line P3HT sample. Having been made from 500 lines/nm diffraction grating, the lines in these patterns appear wider. It is likely the stamp spreads during the imprinting process, producing a less-defined pattern.

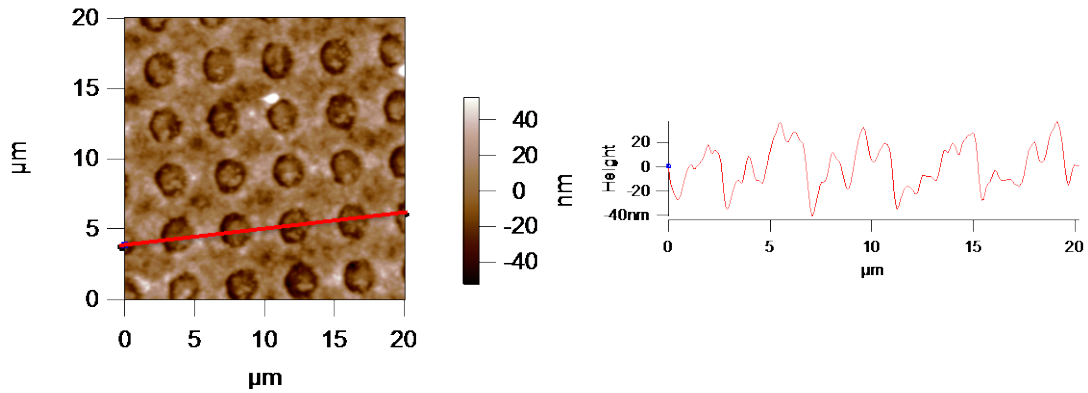


**Figure 5.6.** Height scan and line trace for 2  $\mu\text{m}$  dot P3HT sample. Slight amounts of bowing can be witnessed inside the dot patterns, as is evident in the line scan. These patterns were among the most consistent, as it appeared this size and pattern of stamps is ideal for imprinting.

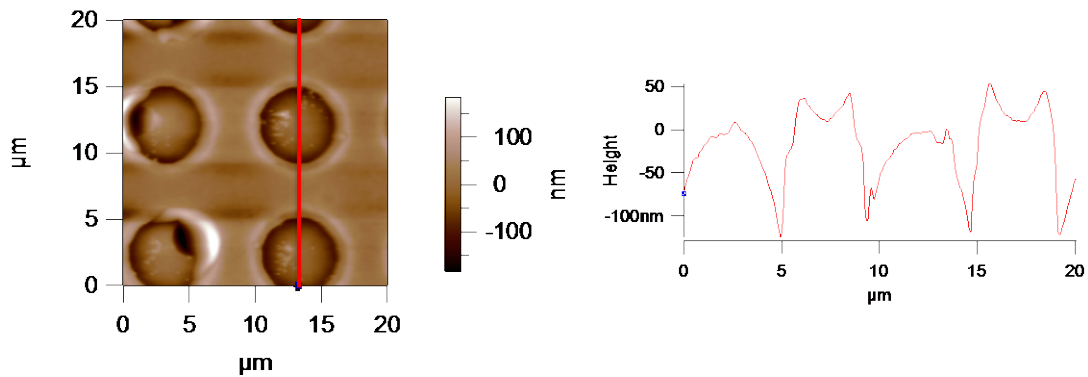


**Figure 5.7.** Height scan and line trace for 5  $\mu\text{m}$  dot P3HT sample. As is evident in the figure, this size dot pattern is pushing the limits of the stamping process. Bowing occurred with the stamp, which is why the voids of the dot pattern appear hill-like while the “flat” areas appear to have dips in them.

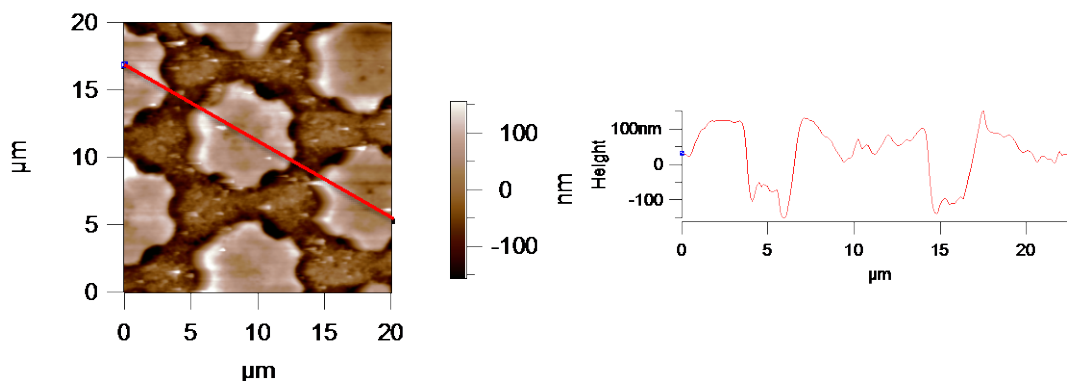


**Figure 5.8.** Height scan and line trace for star P3HT sample. This pattern was unique in that the features were voids in the stamp, making them features in the actual sample. Stamping was surprisingly consistent for such a large figure, as less bowing is seen than in the 5  $\mu\text{m}$  dot samples.

After depositing PCBM via spin coating, films were then tested via KPFM to determine whether patterns were evident both in topography and in surface potential, as P3HT should have a more positive potential energy while that of PCBM would be more negative. As is evident in the figures below, pattern transfer was exhibited in both scans, though it did appear that PCBM deposition disfigured the original imprinted P3HT pattern in many cases. This is not surprising, as it has been found that PCBM regularly diffuses into crystalline P3HT morphologies.<sup>88</sup> Because of this, there are three regions instead of the expected two, morphologically speaking: P3HT-rich, PCBM-rich, and combined P3HT-PCBM regions. Several rounds of patterned samples were created and tested, with analysis of their potential histograms. A discussion is given in the following section.

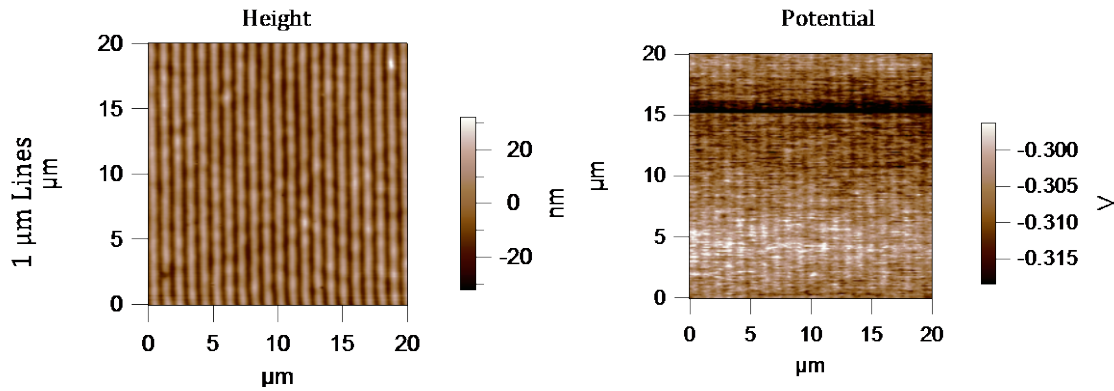


**Figure 5.9.** KPFM example scans for a 1  $\mu\text{m}$  line sample after PCBM deposition. PCBM consistently deposited well into the line voids in these samples, though it is difficult to see accumulated negative potentials due to the small dimensions of the patterns.

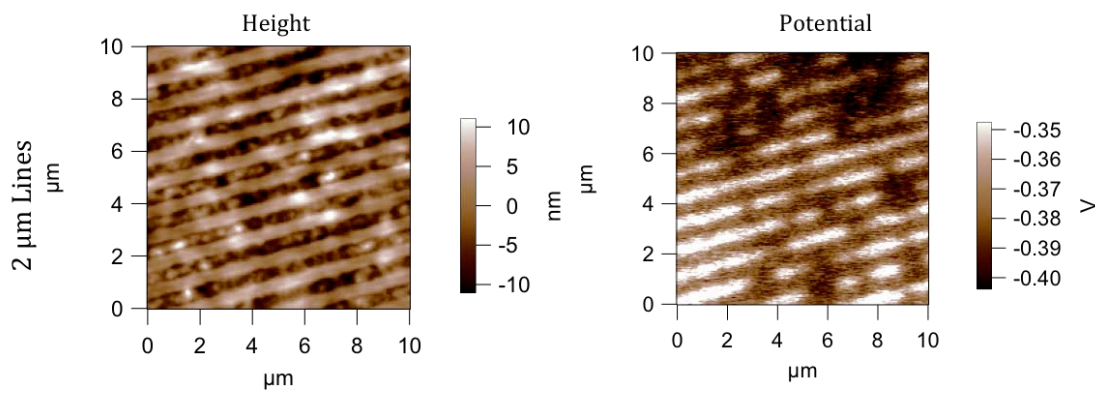


**Figure 5.10.** KPFM example scans for a 2  $\mu\text{m}$  line sample after PCBM deposition. Most of these types of patterned samples showed evidence of the lined pattern but also showed incomplete transfer.

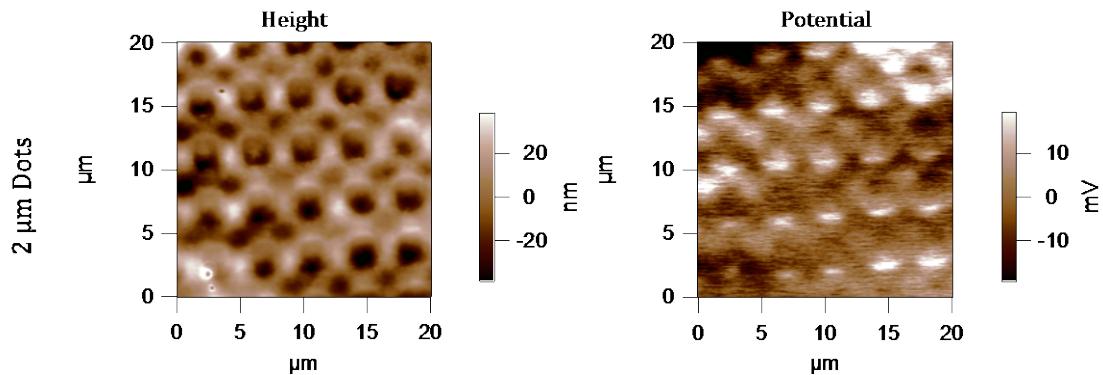


**Figure 5.11.** KPFM example scans for a 2  $\mu\text{m}$  dot sample after PCBM deposition. The light areas in the potential scan correspond to P3HT-rich flat areas in the height scan. These samples exhibited incomplete filling of the dot voids by PCBM. It is possible that this is due to quicker PCBM diffusion into the P3HT regions from a smaller pattern size.

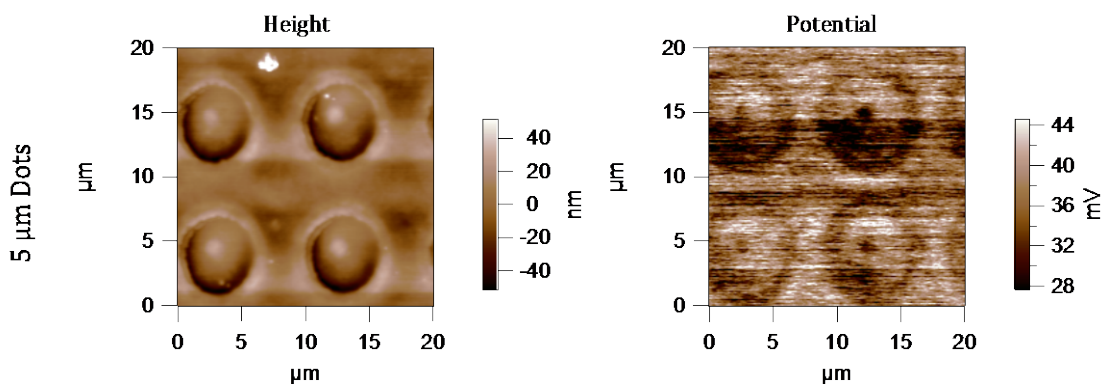


**Figure 5.12.** KPFM example scans for 5  $\mu\text{m}$  dot samples after PCBM deposition. Evident in these samples were the coffee-ring like display of PCBM. Because the dot voids are so large, it was difficult for the entire shape to be filled with PCBM, so deeper sections of the dots accumulated more PCBM clusters and an over all incomplete filling was noted.

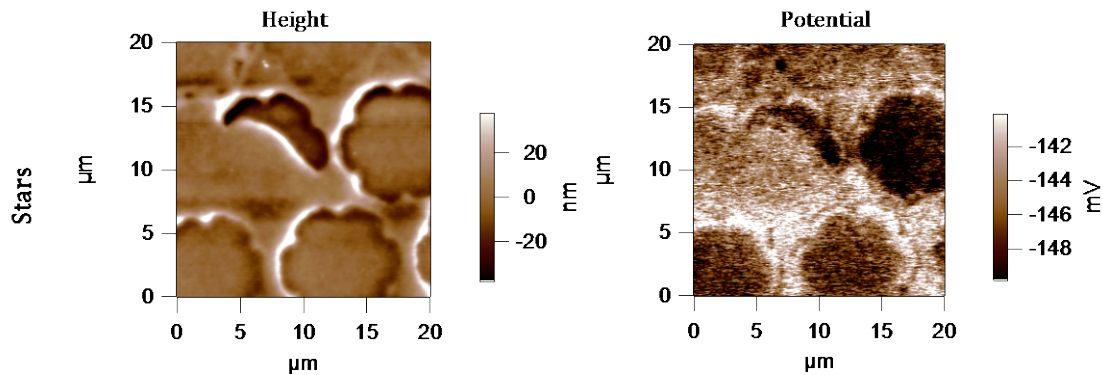


**Figure 5.13.** KPFM example results for the star samples after PCBM deposition. The stars seen here are from a positive star stamp. These patterns were less consistent than others, and this is likely due to the sheer size of the star in the master.

## 5.2 DISCUSSION

After the experiments performed on single material films produced asymmetric potential energy distributions, we believed that intentional patterning of dual-component films would shed some light on factors affecting the potential energy distribution in semiconductor films. Specifically, by intentionally creating grain boundaries and phase segregation between regions of a sample with different potential energies, we sought to determine what effects macro scale morphological characteristics had on the energetic distribution of the overall film.

Interestingly, they have much less of an effect than many would expect. Across the rounds of patterned samples that were tested, there were both asymmetric and normal distributions present, with asymmetric distributions encompassing a vast majority. Example histograms of the potential scans given in Figures 5.9-5.13 are given in Figure 5.14 below. In comparing histograms from many different types of patterned samples, there were no apparent experimental factors determining which were asymmetric.

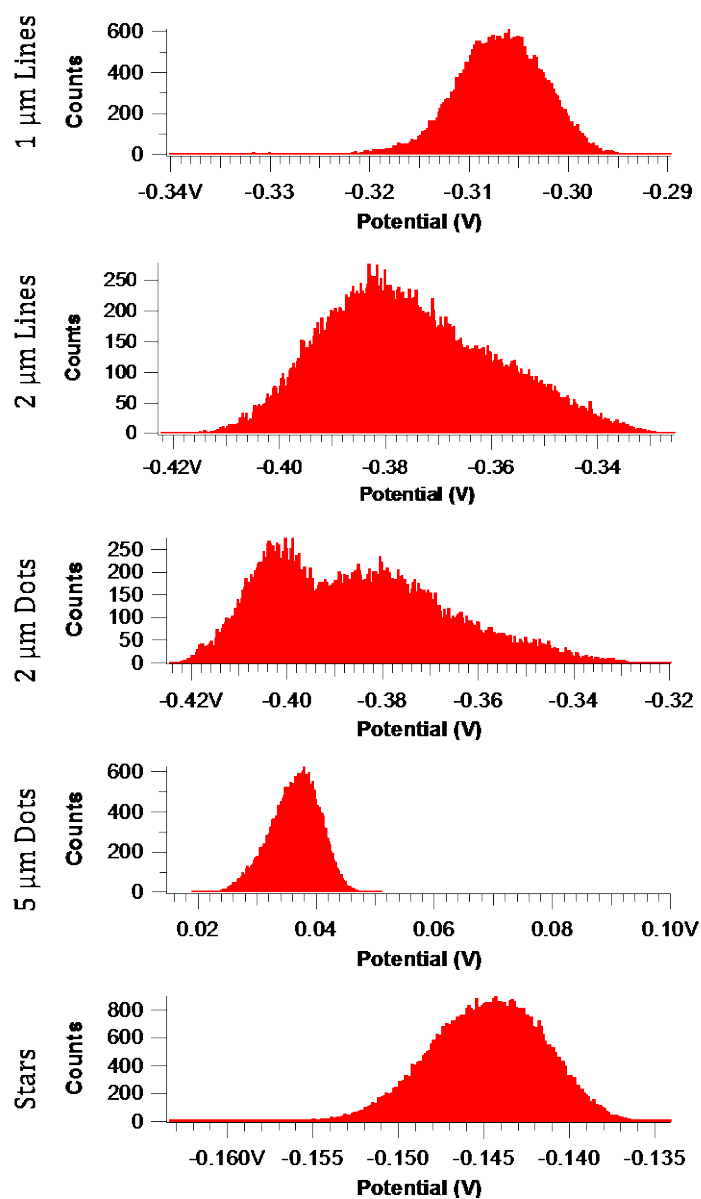


**Figure 5.14.** Histograms of surface potential scans for the samples given in Figures 5.9 through 5.13. As can be seen in the figure, the 1 μm line and star patterns in this example produced more symmetric distributions than the other patterns. The patterned sample sets produced consistent asymmetric distributions in the initial scan 95% of the time.

To quantify the behavior, skewness values were calculated for the patterned samples characterized. Skewness is a measure of asymmetry, and the additional calculation of “skewtest” conveys the probability of the sample set having come from a normal distribution. For example, a distribution with a skewtest value of 0.56 has a 56% probability of coming from a normal distribution.

As the patterning process was sometimes inconsistent even after the optimization process, samples with no discernable pattern in both the height and the potential scans were omitted (roughly 15% of samples created). Among the 75 patterned samples, only four had skewtest values higher than 0.05 (greater than 5% probability that the sample came from a normal distribution). The breakdown of skewtest values among the patterns is given in Table 5.1 below.

**Table 5.1.** Summary of patterned sample skewtest values.

Pattern	Total Samples	Samples with Skewtest $\geq 0.05$	Asymmetric Samples
1 $\mu\text{m}$ lines	12	0	100%
2 $\mu\text{m}$ lines	13	1	92%
2 $\mu\text{m}$ dots	20	2	90%
5 $\mu\text{m}$ dots	10	1	90%
Stars	20	0	100%
<b>Total</b>	<b>75</b>	<b>4</b>	<b>95%</b>

There does appear to be a bit of correlation between the asymmetry and the absolute difference in surface potential between the two materials in the sample. For example, among the surface potential scans and histograms given in the figures above, the more normal distributions (1  $\mu\text{m}$  lines and stars) have a difference in potential of around 10 to 15 mV, whereas the samples with asymmetric distributions (5  $\mu\text{m}$ , 2  $\mu\text{m}$  dots, and 2  $\mu\text{m}$  lines) display a difference of approximately 16 to 20 mV. Other samples tested roughly show the same correlation, though there was certainly overlap in the potential gaps between the two types of samples. In comparison to the absolute value and the spread of the distribution, however, this is not a large change in surface potential.

Topography, in fact, seems to have much less of an effect on the actual shape of the surface potential distribution than one might expect. The dropcast scans given in Figure 5.15 are from samples of the same batch scanned approximately 20-40 minutes apart. They have very similar topographies in terms of range, disorder, and resolution, and yet, they give fairly different energy distribution shapes. This is indicative of an energetic equilibration effect mentioned earlier: that through the process of scanning, charge transport pathways are dynamic, and they evolve based on the molecular sites available to them with the charging and discharging of traps in the film.

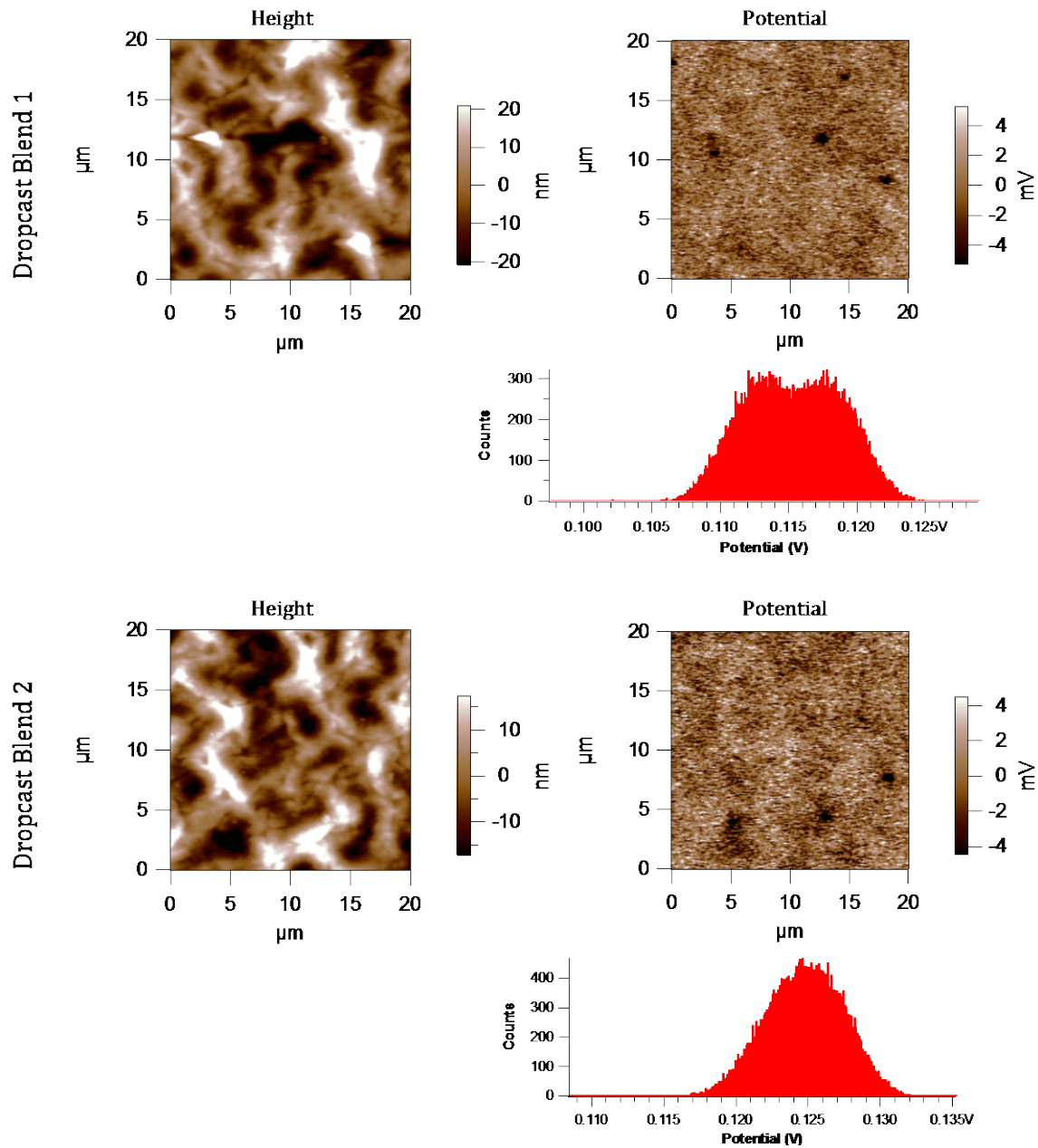


**Figure 5.15.** Height and potential scans with potential histograms for samples from the same batch of a dropcast P3HT/PCBM film scanned via KPFM approximately 20-40 minutes apart. Similar topographies produce different potential distributions, indicating the source of the distributions' shapes is separate from topography.

One certainly might speculate that the asymmetry in the potential distributions is caused by a multi-Gaussian or multi-Voigt distribution, i.e. that the peaks of the component materials are too close together in the distribution to be completely resolved, which would be supported by a handful of samples with high resolution in the potential scan where two peaks are indeed seen (one example is the 2  $\mu\text{m}$  dot sample in Figure 5.14). We think this is not the case due to the nature of the asymmetry. If the distribution was indeed comprised of two Gaussian peaks combined, it would likely display a broadening on both sides of the peak, as the dual-peaked distributions show. The asymmetric distributions seen in the patterned samples tested show a much more pronounced extension on only one side, leading us to believe this is evident of a unique process occurring on a scale much smaller than topographical characteristics.

One might also expect a higher degree of correlation between the height and potential scans in patterned samples, as the morphologies have been intentionally phase separated between the two materials with different energy values. To determine whether this is the case, the  $R^2$  correlation value was calculated for all samples tested, including both the single-material films and the patterned samples, between the height and potential scans. First the scan images were saved as text files with each point in the scan having its own value, then the correlation was calculated between the corresponding points in each scan. The  $R^2$  value for each sample is the average of all these points. The average  $R^2$  value for all of the single material samples on ITO slides is 0.19, and the average for all of the patterned samples is 0.18. Thus, even with intentional patterning of two component materials, there is not an appreciable correlation between the height and potential values.

### 5.3 CONCLUSIONS

Like the samples detailed previously comprised of only one material, patterned samples made of P3HT and PCBM mixes appear to have an energetic disorder giving rise to asymmetric potential energy distributions. While morphology has some effect on disorder in organic devices, it is not the only factor at play. Samples outlined in this chapter support the theory that energetic defects persist within the bulk materials of the active layer that contribute to asymmetry in the potential distribution.

## 6.0 CONCLUSION

### 6.1 SUMMARY AND CONCLUSIONS

The goal of this research project was to explore the surface potential distributions of organic semiconductors commonly used in electronic devices. When thin films of phthalocyanine materials were tested via KPFM, an unexpected asymmetry in the potential energy distribution was observed. As the Gaussian disorder model is commonly accepted to describe semi crystalline materials well, we expected a normal distribution in the surface potential. When this was not seen, more materials commonly used in electronic devices were tested along with multiple substrates. The asymmetry persisted in all materials and in almost all substrates. Control tests were also performed to rule out instrument artifacts, temperature and humidity dependence, etc.

After comparing these results to Monte Carlo simulations for monolayer semiconductors utilizing a wide array of disorder effects, we concluded that the asymmetry was likely due to charge islands within the film. We believed that these charge islands are likely due to energetic traps in the film affecting charge movement. After this initial investigation, new sets of experiments were performed to answer the following questions: Does the asymmetry persist beyond the first KPFM scan (~20 minutes)? And is the asymmetry caused primarily by grain boundaries/phase separation in the films, as is commonly suggested?

Over long scan times (~2 hours) via KPFM, the asymmetry noted in initial scans of the organic semiconductor films does not remain. We observed an equilibration after the first few scans where two major changes are noted: that the absolute value of the surface potential shifts over time (either positively or negatively in different samples) and the shape of the distribution changes to become more normal/Gaussian. This effect became faster and more pronounced when samples were electrically grounded, giving further evidence of charge movement being affected. The time scale on which this process occurred was much too long for the instrument to be picking up actual movement of individual charges, but it was possibly indicative of the charging/discharging of deep seated energetic traps in the film. This is supported by the fact that other researchers have noted a presence of dual disorder regimes, static and dynamic, where the former is more energetically shallow and the latter is deeper. In addition, when the surface potential value of the scans is plotted versus time, we noted two distinct regions: one where the potential shifts quickly (shallow traps) and another where the potential shift is much slower (deep traps).

To test the effects of grain boundaries and phase separation, we created patterned films of P3HT/PCBM combinations with varied spacing and design. We observed no apparent correlation between the degree of material separation and asymmetry in the potential energy distribution. Though there were cases of highly resolved patterns where the potential energy distribution produced two distinct Gaussian peaks, this did not appear to feasibly explain the asymmetry in other distributions. Creating our own artificial “charge islands” with dotted stamps (1  $\mu\text{m}$  and 2  $\mu\text{m}$  dots) did not appear to consistently reproduce the asymmetry as was predicted after the first set of experiments performed. However, this was not unexpected, as the scale of the dot pattern

and the scale of a charge island due to an energetic trap would be vastly different (micrometers versus tens or hundreds of femtometers).

## 6.2 FUTURE DIRECTIONS

As with many areas of research, the minute one question is answered, another three pop up in its place. There are several follow-up research avenues that might be pursued after this project.

The experiments exploring the time evolution of surface potential highlighted an interesting process at play in these materials: that there is some equilibration process occurring during long scan times that appears to be affected by charge movement in the active layer. Based on the experimental evidence detailed above, we believe it to be a charging and/or discharging of traps in two different energetic depths. This is consistent with the control experiments performed and with noted literature findings. With the patterned samples, however, there was little observable correlation between the degree of phase separation and the asymmetry of the distribution. We saw some samples of a pattern exhibit perfectly normal distributions while others of the same pattern displayed highly asymmetric patterns. Many speculate that grain boundaries in organic semiconductors yield very deep energetic traps in the disorder landscape. If our hypothesis about the nature of the equilibration is correct, then long scan times of patterned samples should indicate the presence of shallow traps, deep traps, or both. For instance, if many patterned samples display initial asymmetry in the potential distribution with no indication of discharge of deep traps over long scan times, it would be unlikely that deep traps are causing the asymmetry at all. However, if deep trap discharge and initial asymmetry in the

potential distribution occur consistently, it is a possible contributing factor. Long KPFM experiments of the patterned samples would be a worthwhile next avenue for the project.

Another set of experiments might explore possible dependence on film width. All of the films tested here are likely between 50 and 150 nm. Because Kelvin probe AFM is a surface technique, it is expected to probe only the first few layers of the film itself. As such, it is difficult to determine with KPFM whether the effects exhibited here are occurring entirely on the surface, within the bulk, both, or neither. Testing monolayer semiconductor films, with both single material and dual component patterned films included, would provide us information about the true location of the energetic traps hypothesized to be a main cause of the effects outlined above.

It is important to recognize the limitations of the experimental setup described here. Not only is KPFM a surface technique, but also its resolution is not sufficient to provide information about disorder on the nanoscale. Currently, we can only use intentional experimental setup and resulting evidence to make educated guesses about the causes of asymmetric potential energy distributions. To elucidate more detail here, other techniques might be used, like excited state absorption spectroscopy or fluorescence excitation spectroscopy. In fact, deep level transient spectroscopy (DLTS) would be a particularly well-suited technique for this system. DLTS uses a voltage pulse to measure defect charging into the space charge region of simple devices and is commonly used for semiconductors.<sup>89-92</sup>

## APPENDIX A

### ASYMMETRY CONTROL EXPERIMENTS

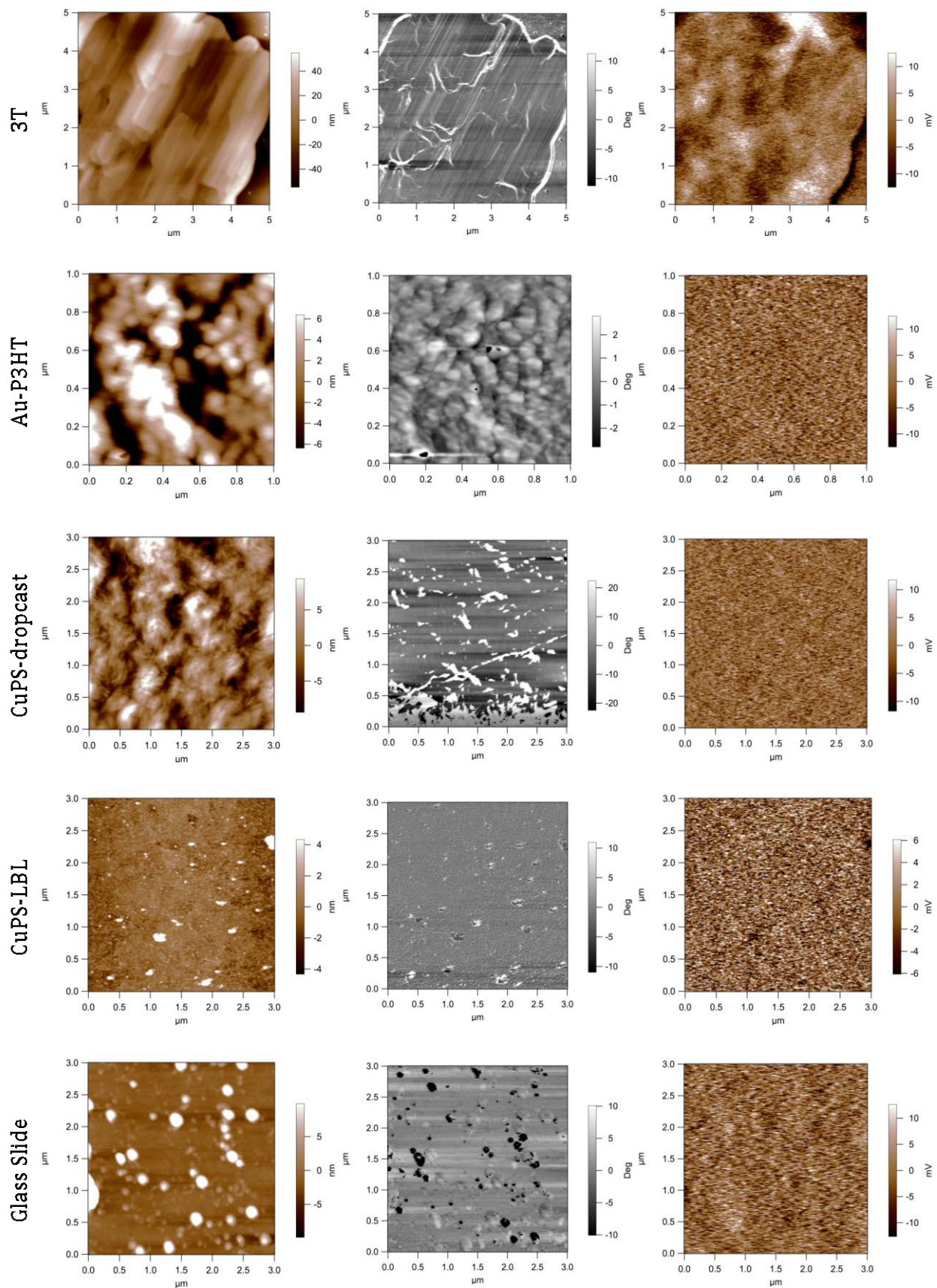
*This information previously published as supplemental information.*<sup>93</sup>

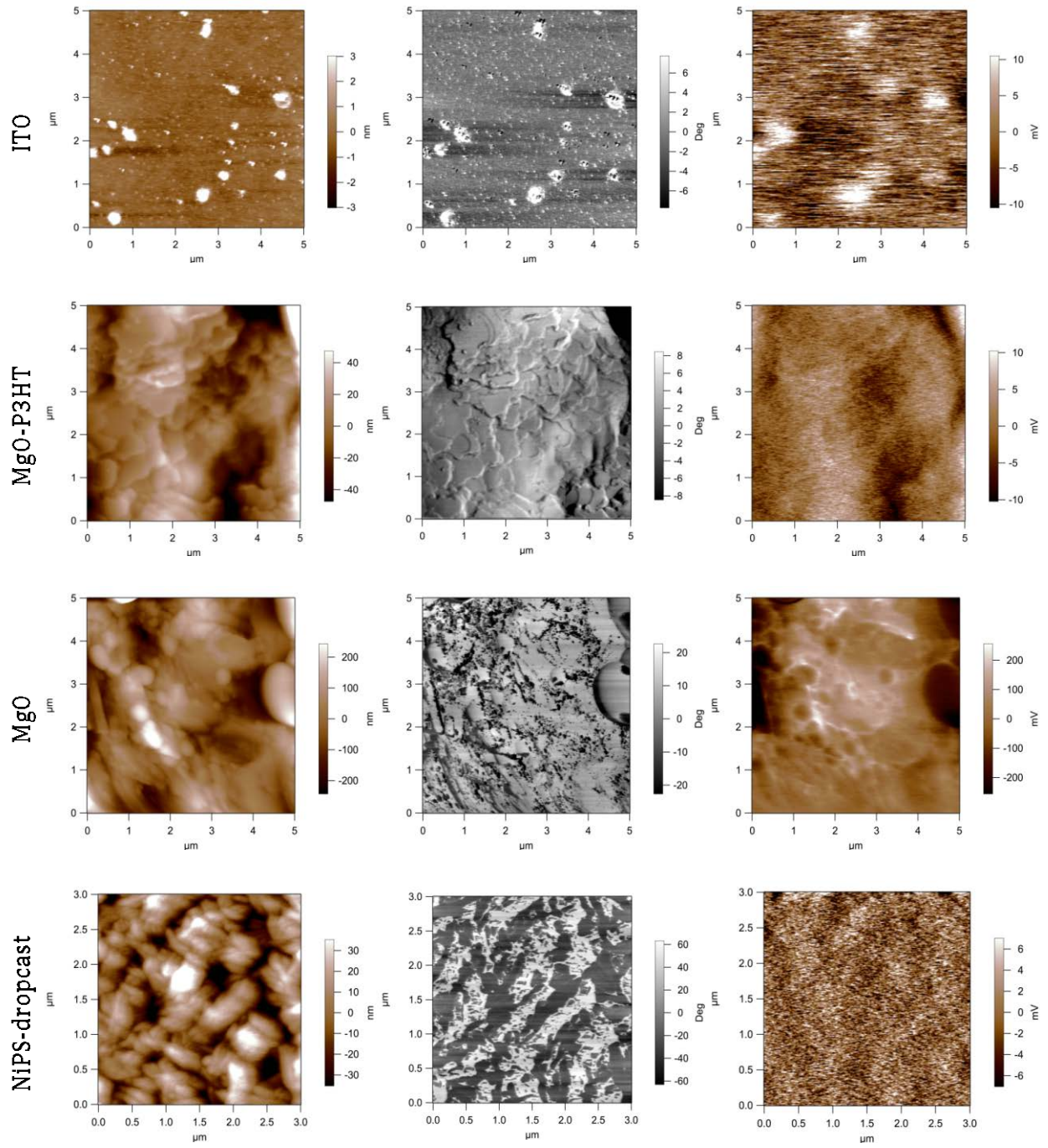
This appendix is comprised of all control experiments performed to evaluate the asymmetric surface potential distributions noted previously. These include surface treatments, interfacial layers, rough topography correlation calculations, evaluation of tip contamination, etc.

#### A.1 SCAN IMAGES

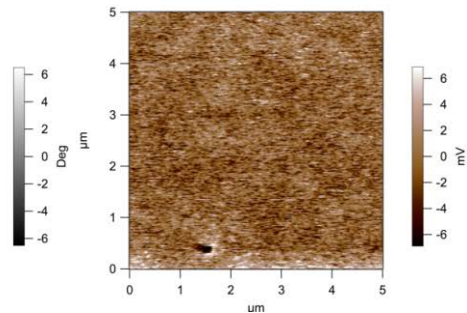
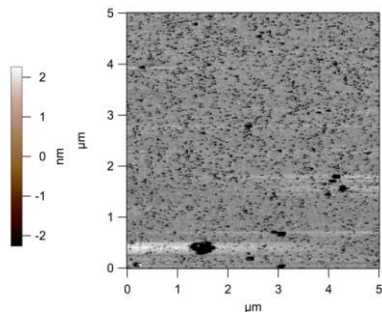
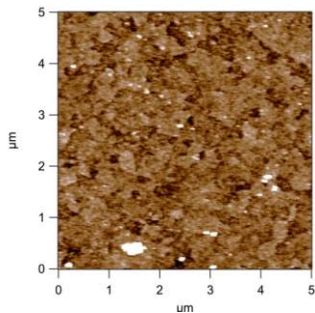
Below are sample scans from each of the types of samples studied. All raw data is available upon request via the Internet at [hutchison.chem.pitt.edu](http://hutchison.chem.pitt.edu) or by e-mail request. Height, phase, and potential scans (left to right) are given where the units are nm, degrees, and mV, respectively. All scans are 5  $\mu\text{m}$  x 5  $\mu\text{m}$ , and samples are provided in alphabetical order for clarity.

Note: Figure A.1 below spans several pages (104-107) and the figure caption can be found on page 107.

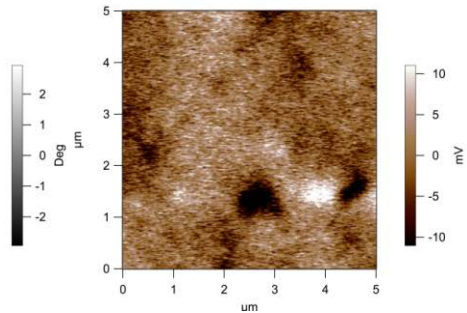
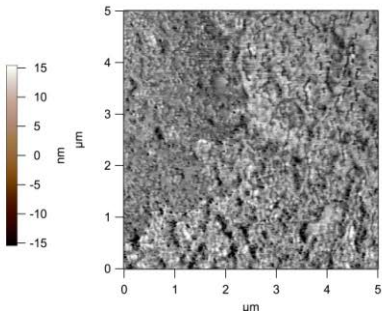
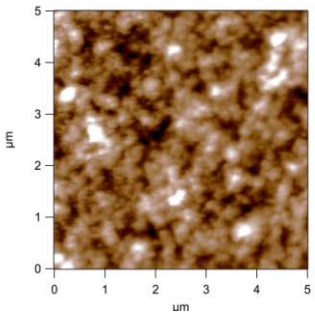




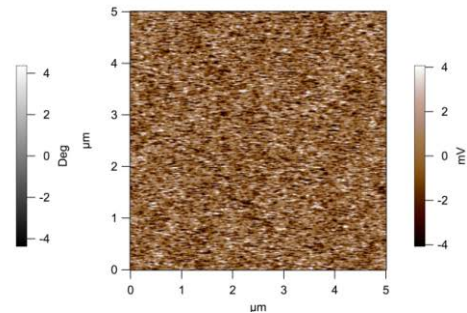
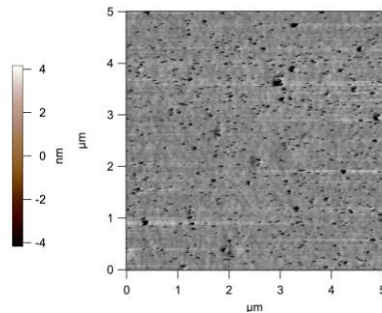
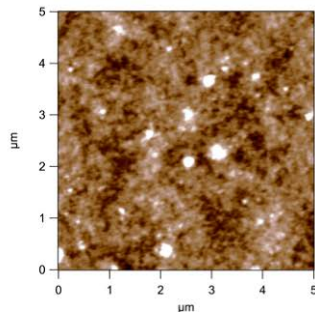
NIPS-LBL



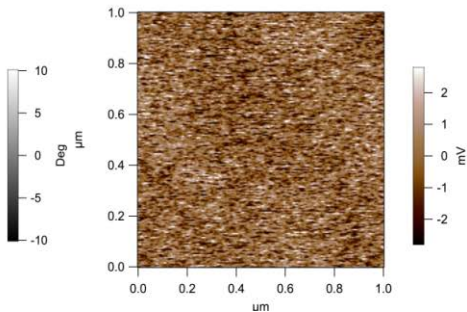
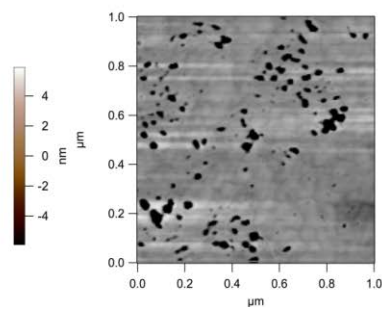
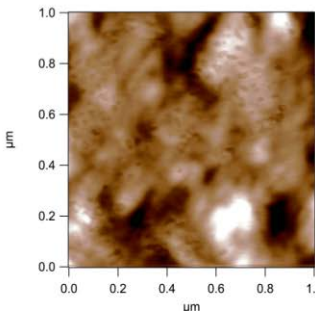
P3HT

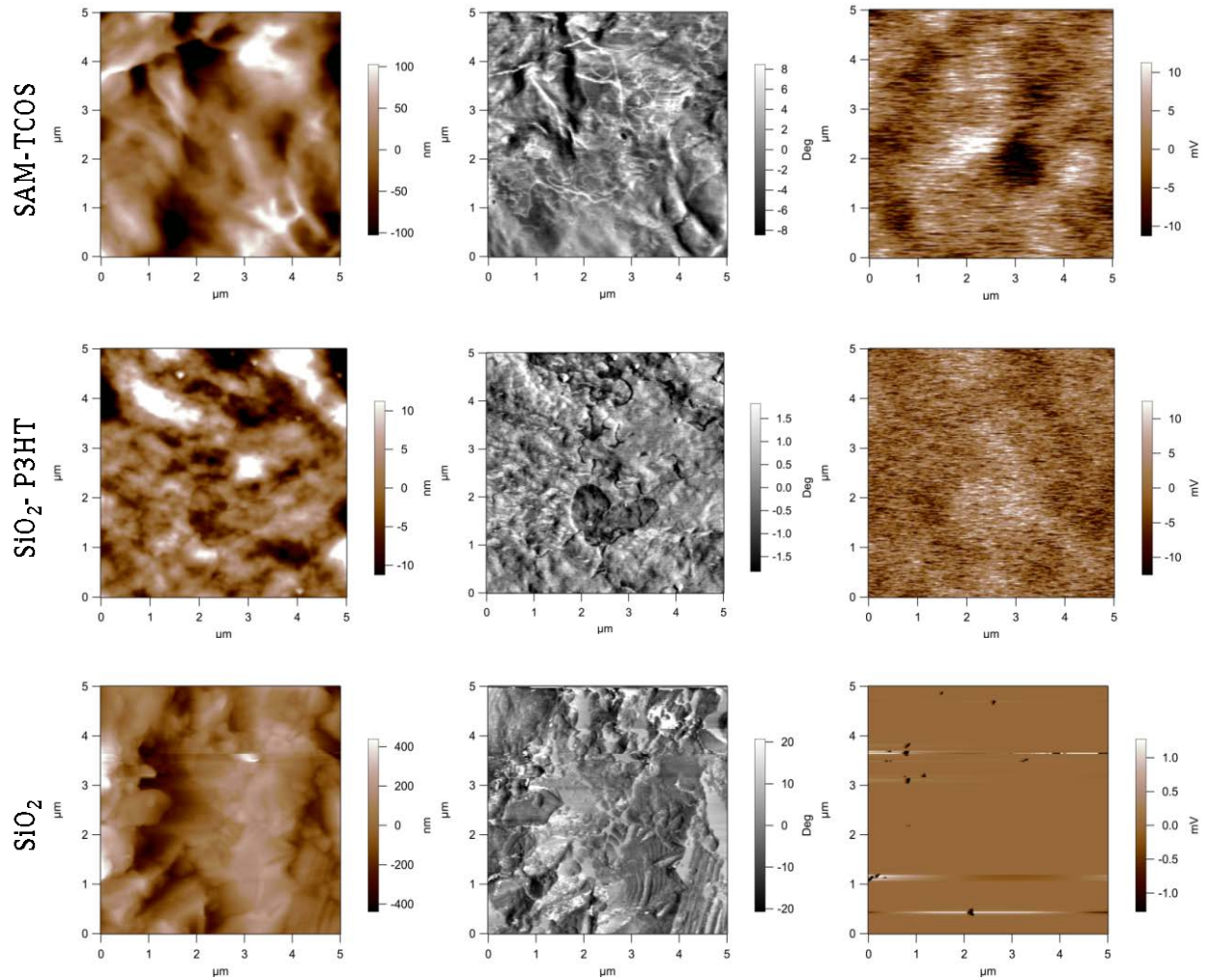


PEDOT



SAM-APTES



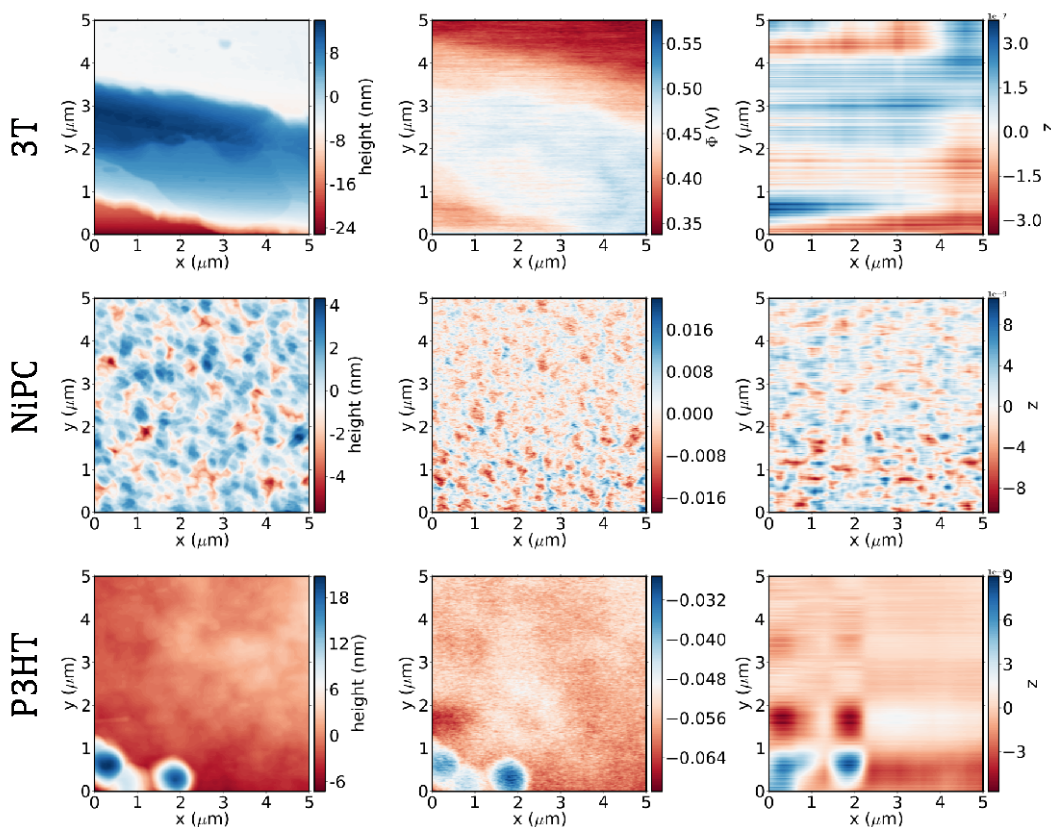


**Appendix Figure 1.** Height (left), phase (middle), and potential (right) scan images for each of the sample types tested. All scans are the first of the set taken for the sample and were taken in ambient conditions using experiment settings described in Chapter 3.

## A.2 SAMPLE PREPARATION VARIATION

### A.2.1 Rough sample correlation

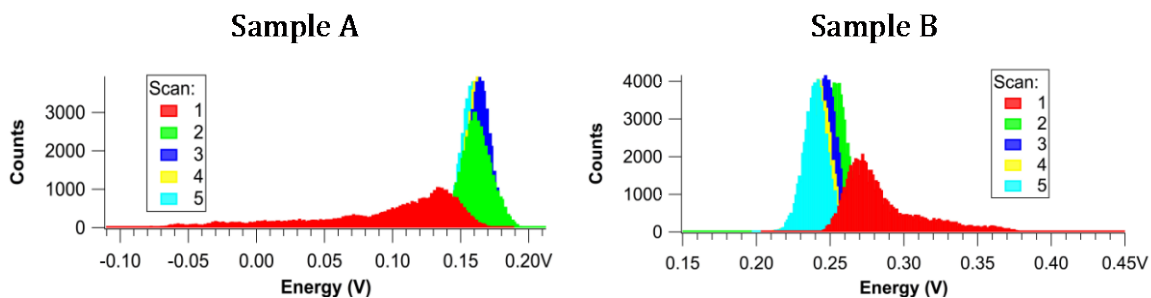
To confirm the removal of topographically rough samples scanned via KPFM, the coefficient of correlation,  $R^2$ , for each sample's potential and height scan data was calculated. Overall, less than 10% of all samples scanned showed an  $R^2$  greater than 0.5, and all of those were included in “rough” samples removed from statistics. Below are the plots (height, potential, and correlation) for all samples with an  $R^2 \geq 0.5$ .



**Appendix Figure 2.** Topography (left column), potential (middle column), and correlation (right column) plots for each of the indicated materials. Height and potential scans were taken directly from experiment data. Correlation plots were calculated using the deviance of the height and potential scans calculated for each point in the grid.

## A.2.2 Sample Batches

While samples were consistently made in the same manner, some environmental aspects were not easily controlled in a lab setting. For example, lab temperature and humidity could vary day to day. Samples from the same batch tend to have similarly shaped histograms and to have a potential drift heading toward a similar value. Still, as can be seen in the two samples below, even those from the same batch, having had the same temperature, humidity, dropcasting time, etc. can be dissimilar in the overall potential and in the skewness direction of the initial distribution.

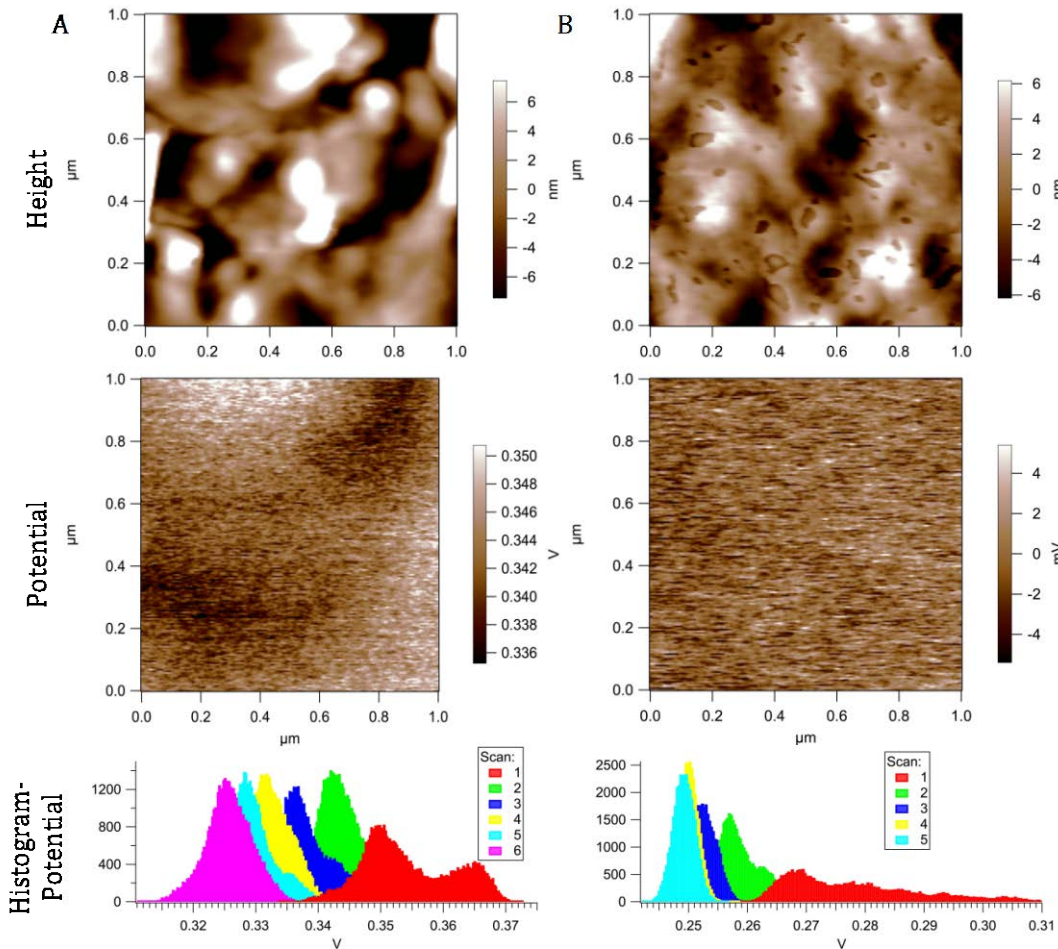


**Appendix Figure 3.** Two P3HT samples scanned for the same amount of time after being prepared at the same time in the same manner.

### A.3 INTERFACIAL EFFECTS

#### A.3.1 Ozone-Cleaned Substrates

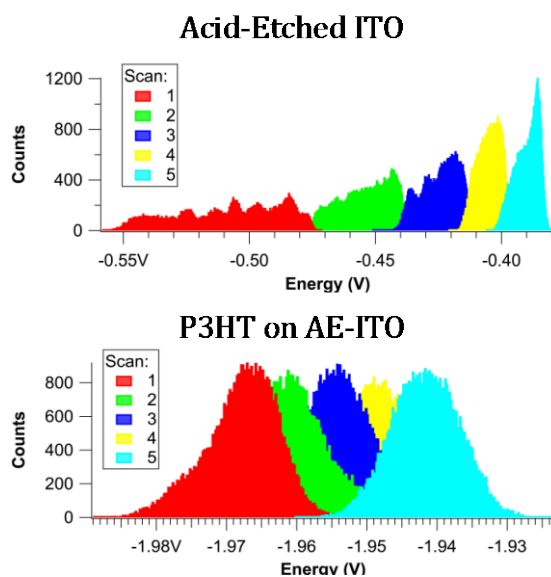
To determine whether organic defects at the organic semiconductor-ITO interface affected behavior witnessed during KPFM scans, ITO substrates were cleaned for 20 min in a UV-Ozone cleaner (with 30 minutes hold time after cleaner was turned off) prior to deposition of P3HT via dropcasting, consistent with prior samples.



**Appendix Figure 4.** Two samples (A and B) made from P3HT deposited onto ozone-treated ITO substrates and scanned via KPFM with sample grounding. Including height and potential scans of one scan and a histogram of all potential scans from the sample (as indicated).

### A.3.2 Acid-Etched Substrate

As acid etching has had demonstrated effects on the electrical activity of ITO substrates,<sup>94</sup> ITO was etched with a solution of hydrochloric acid and dried under nitrogen prior to deposition of P3HT. No noticeable difference between P3HT on cleaned ITO and on acid-etched ITO was observed for height or surface potential.

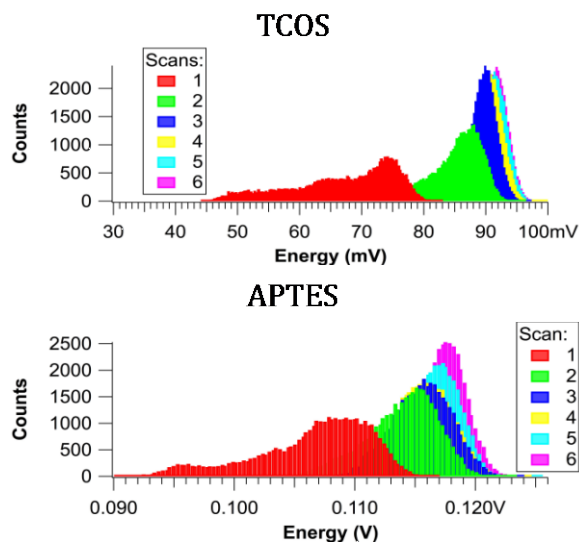


**Appendix Figure 5.** Surface potential distributions for acid-etched ITO and a P3HT solution deposited onto acid-etched ITO.

### A.3.3 Self-Assembled Monolayer Samples

Self-assembled monolayers (SAMs) have previously been utilized for a variety of modifications in organic electronic devices, from use as a hole-injecting layer to dielectric materials in transistors. Because of this, their effects on the surface potential of the films tested were

determined. Again, no discernable difference was noted with the use of SAMs with the substrates and materials tested.



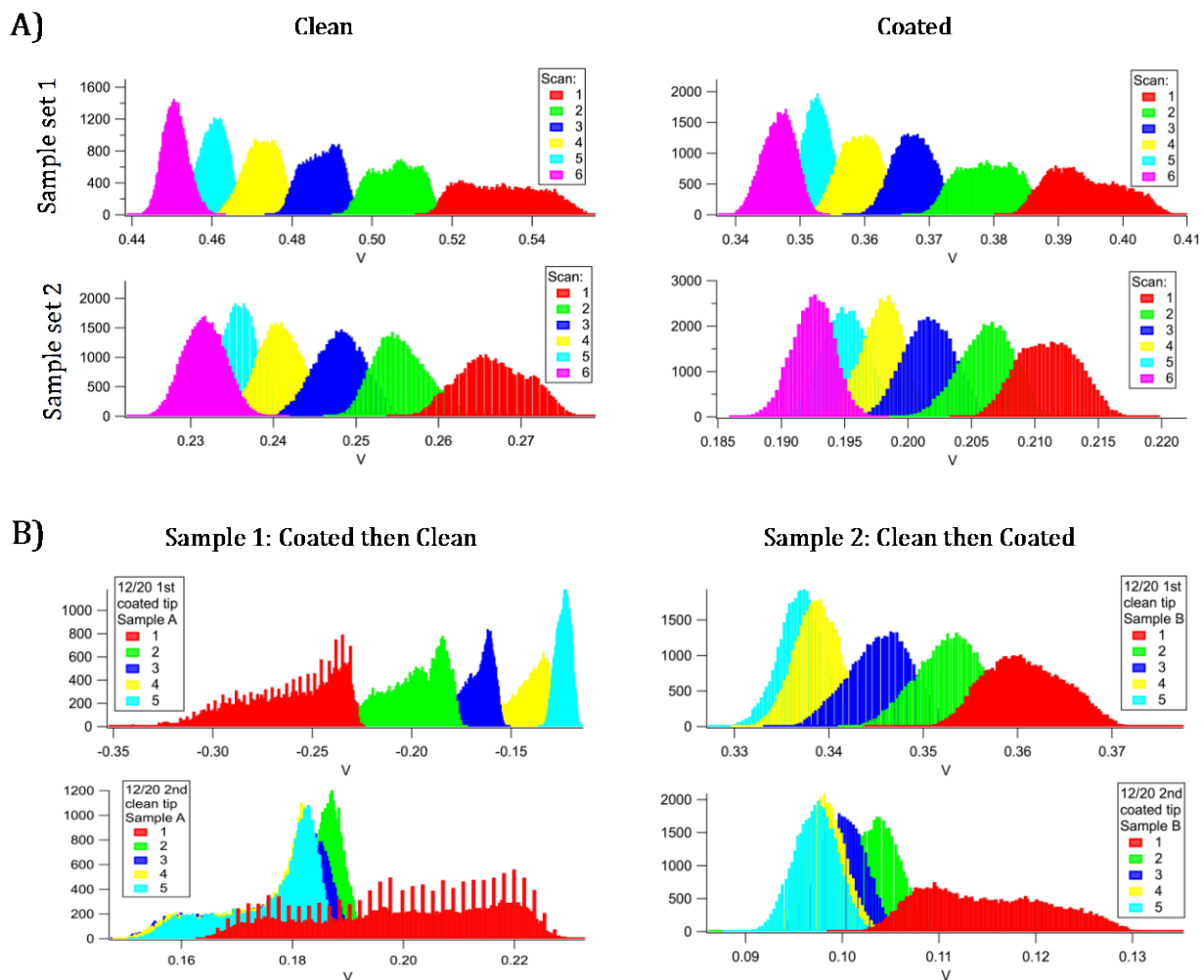
**Appendix Figure 6.** Histograms of multiple scans for P3HT/SAM samples. Both films are P3HT dropcast onto a TCOS or an APTES self-assembled monolayer.

## A.4 TIP/INSTRUMENT ARTIFACTS

### A.4.1 Contaminated Tip Tests

By intentionally coating an AFM tip in the same substance as that being scanned, the effects of scanning a sample with a “contaminated” tip could be determined. The film of P3HT dropcast onto the tips was visible in color and texture. In Appendix Figure 7A below, four P3HT films were deposited onto ITO glass slides at the same time and scanned with either an AFM tip cleaned via ozone or a tip coated in P3HT (clean and coated, respectively). In Appendix Figure 7B, two samples were made at the same time. Sample 1 was scanned first with a coated tip then

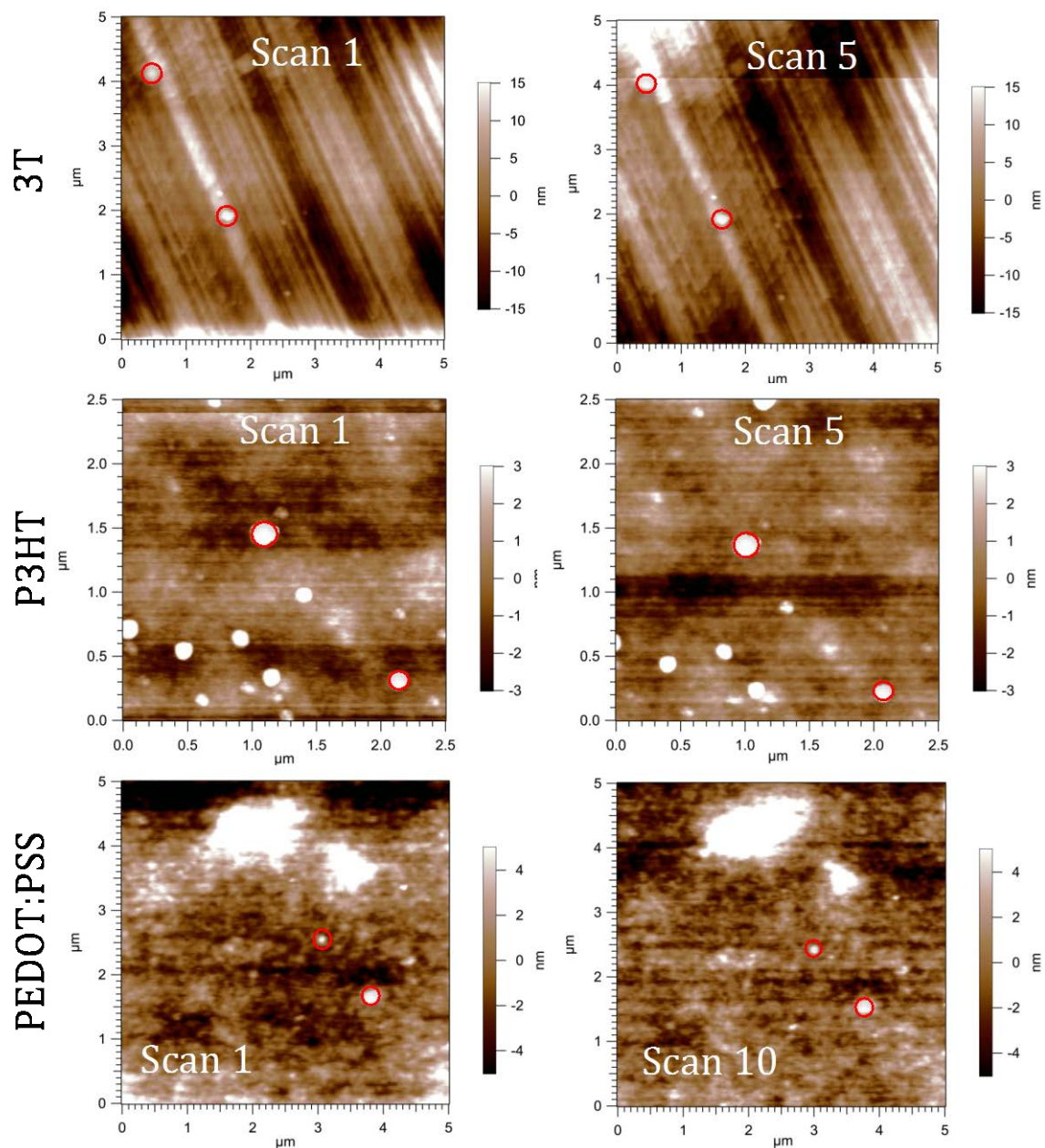
with an ozone-cleaned tip, while sample 2 was scanned with a clean tip first followed by a coated tip. Effects of tip contamination appeared to be minimal if present at all for all tests performed.



**Appendix Figure 7.** A) Histograms of potential scans of P3HT films made at the same time utilizing both clean (left) and coated/contaminated (right) tips to determine the effects of contaminated tips on sample behavior. B) One P3HT sample was scanned successively with coated then clean tips (left) while the other from the same batch was scanned with clean then coated tips (right).

#### **A.4.2 Topography Drift**

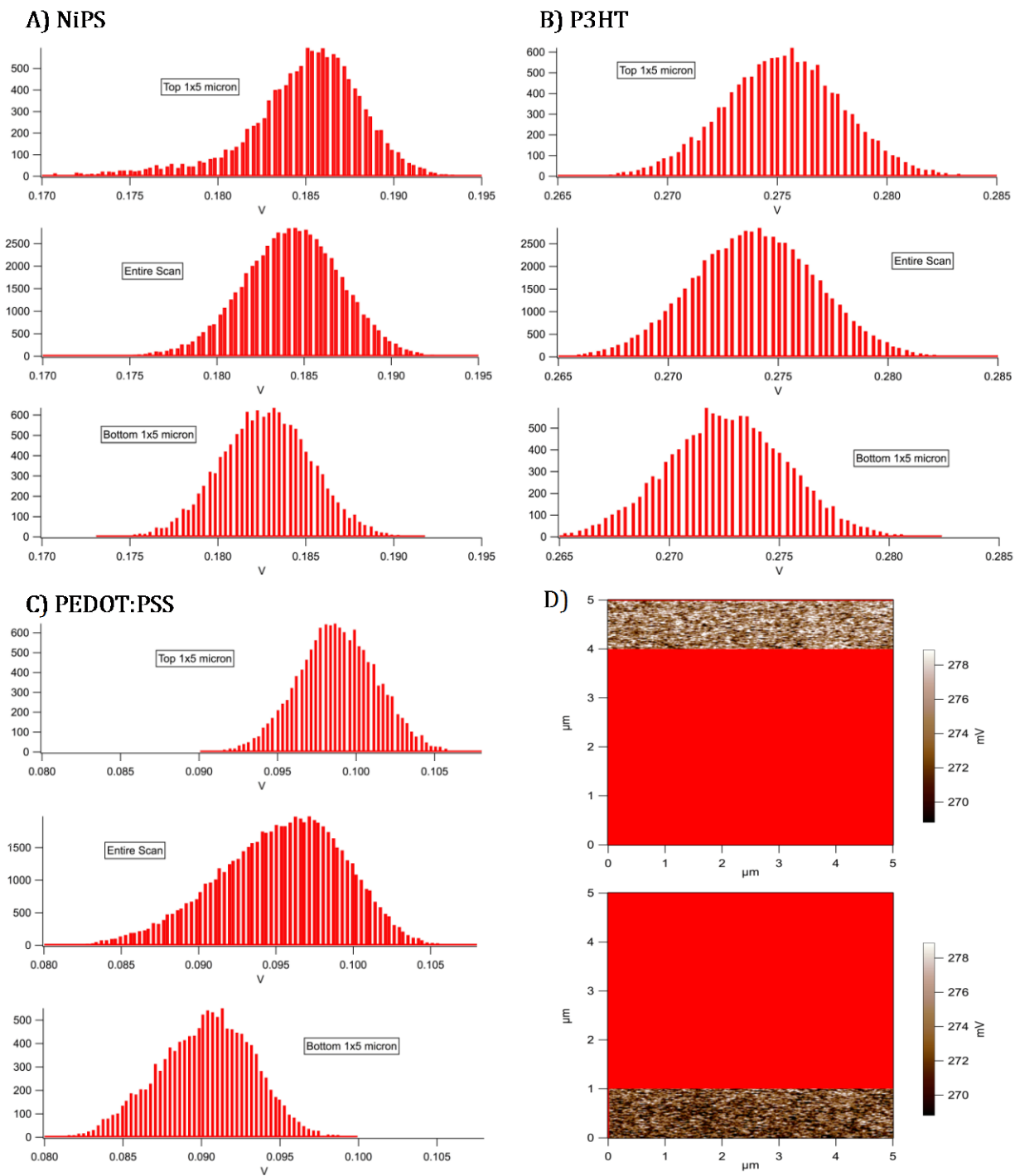
To ensure that potential changes over time were not caused by changes in the topography of the sample, the first and last height images of several scans were analyzed for how much they had shifted and/or changed during the full scan time. These are shown in Appendix Figure 8 below. Features were identified in the first topography scan and tracked through to the last scan. The change in their positions was calculated and averaged across all three scans. The average change in their positions was calculated and averaged across all three scans. The average change in the x-direction is 0.034 nm/hr and in the y-direction is 0.049 nm/hr.



**Appendix Figure 8.** First and last (as indicated) topography scans of terthiophene (top), poly(3-hexyl)thiophene (middle), and polyethylene dioxythiophene: polystyrene sulfonate (bottom). Each scan lasts approximately 10 min.

### **A.4.3 Potential Drift**

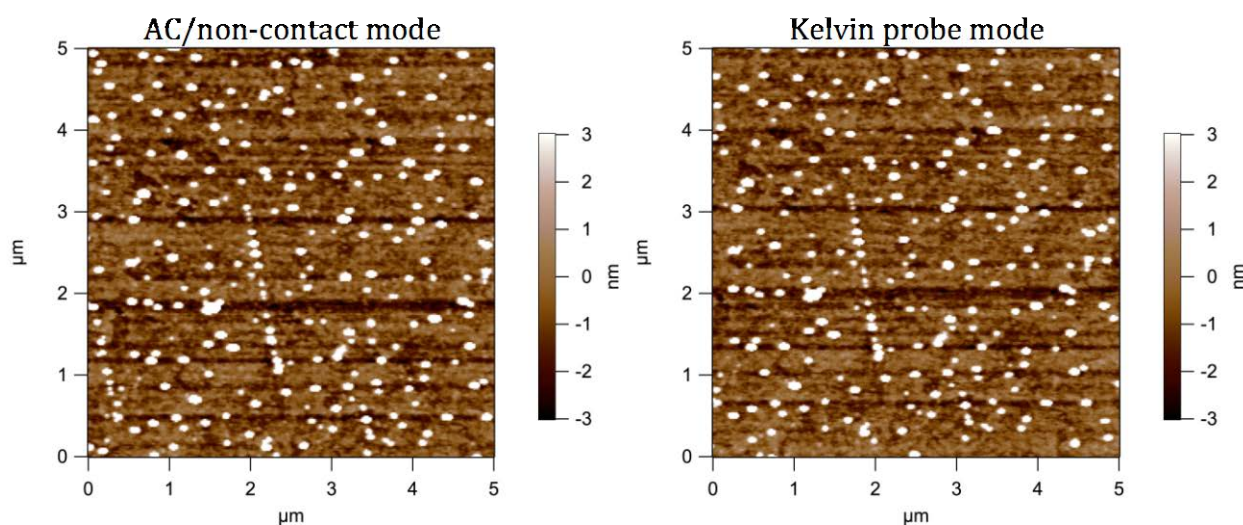
To ensure the potential scans did not shift overmuch during one scan period, histograms of the top and bottom  $1 \times 5 \mu\text{m}^2$  were compared with the histogram of the entire scan for three different samples. As can be seen in Appendix Figure 9, while the graphs of the top and bottom are separated by a small change in potential, it is unlikely that the change is significant enough to change the shape of the overall histogram.



**Appendix Figure 9.** Divided histograms for the top  $1 \times 5 \mu\text{m}^2$ , the entire scan ( $5 \times 5 \mu\text{m}^2$ ), and the bottom  $1 \times 5 \mu\text{m}^2$  for A) sulfonated nickel phthalocyanine, B) poly (3-hexyl)thiophene, and C) polyethylene dioxythiophene samples. Part D) shows an example of the method used to separate the scans to take histograms of different segments, by masking the rest of the scan.

#### A.4.4 Topography Mode Variation

Because differences in topography imaging can sometimes occur between two different AFM modes, scans were taken of the same sample in the same area with regular non-contact/AC mode and also with KPFM. From this, one can see that the topography variation between the two modes is negligible, as can be seen in Appendix Figure 10 below.

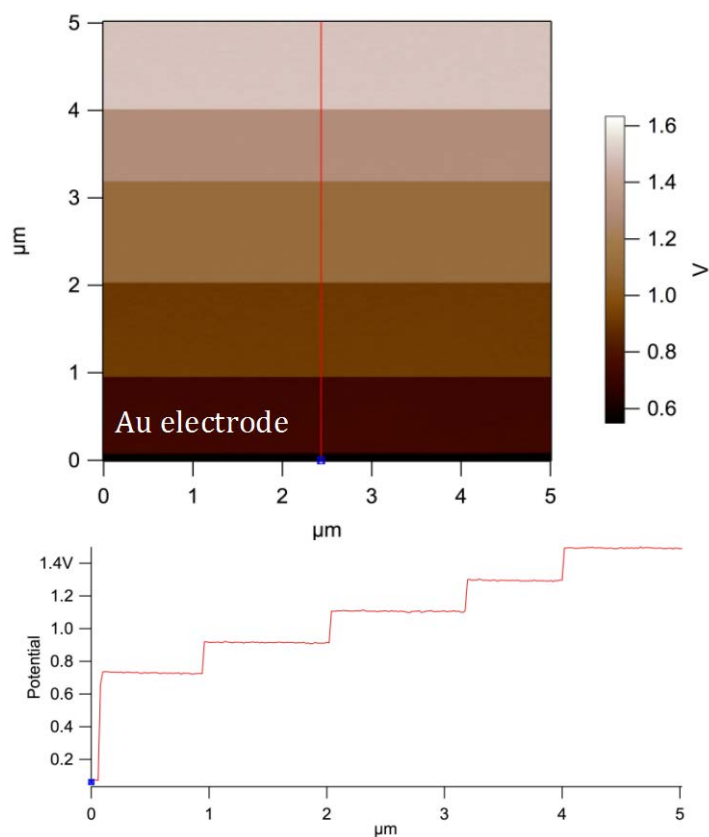


**Appendix Figure 10** Height images for a layer-by-layer deposited thin film of nickel phthalocyanine taken in the same spot using both non-contact (left) and Kelvin probe (right) modes.

#### A.4.5 Standard Sample Bias

To test the effectiveness of sample offset via the instrument controller, a gold electrode was tested in Kelvin mode with successive biases applied. The potential scan is given in Appendix Figure 11 below, with a line graph across the changing bias to show the effectiveness of the offset. The biases applied from the beginning of the scan to the end (changing approximately every 1 μm) are as follows: 0.6V, 0.8V, 1.0V, 1.2V, and 1.4V. Though the instrument measured

the potential as approximately 0.1  $\mu\text{V}$  higher than was applied, it was consistent and precise following changes made to the bias.

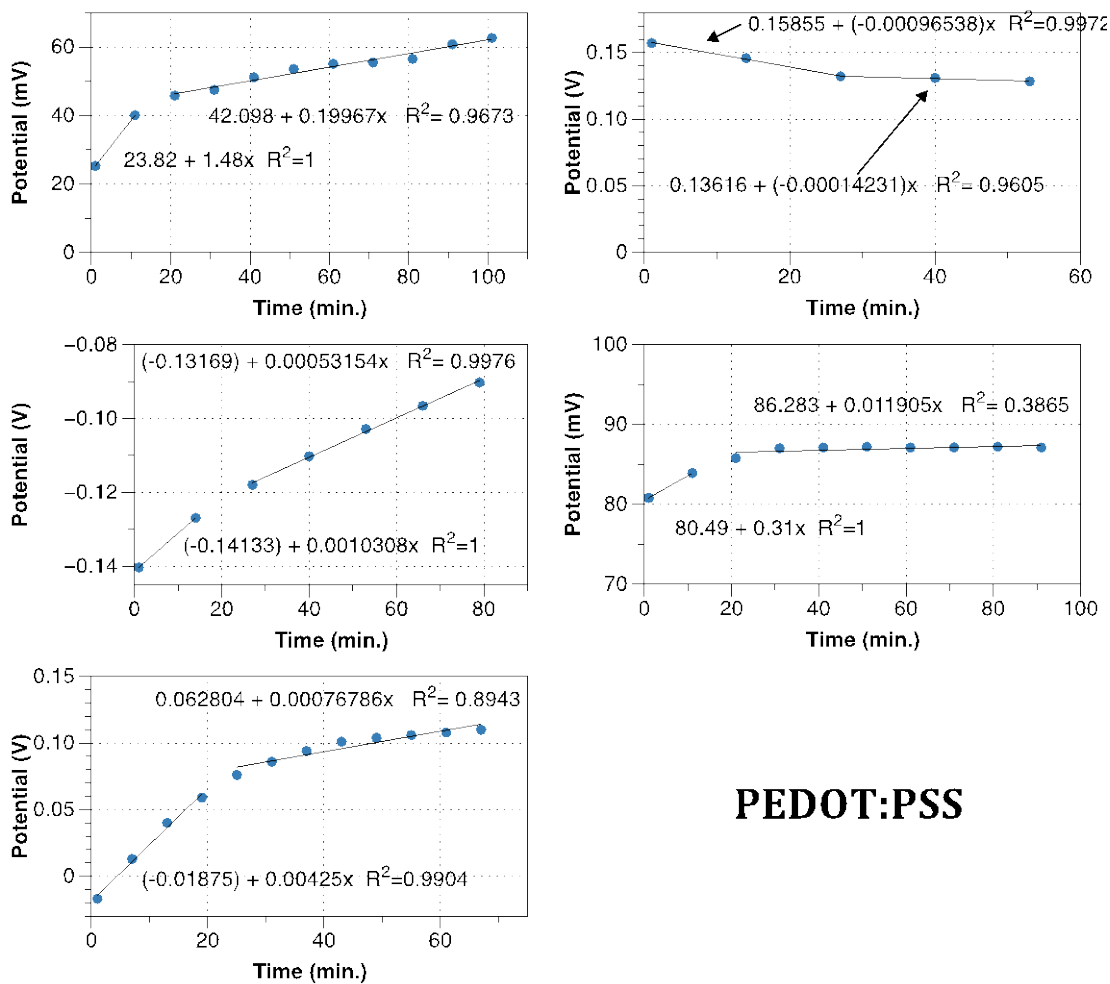


**Appendix Figure 11.** A potential scan and corresponding line scan for a sample gold electrode tested via KPFM. Applied bias was changed approximately every micron by 0.2V and ranged from 0.6V to 1.4V.

## **APPENDIX B**

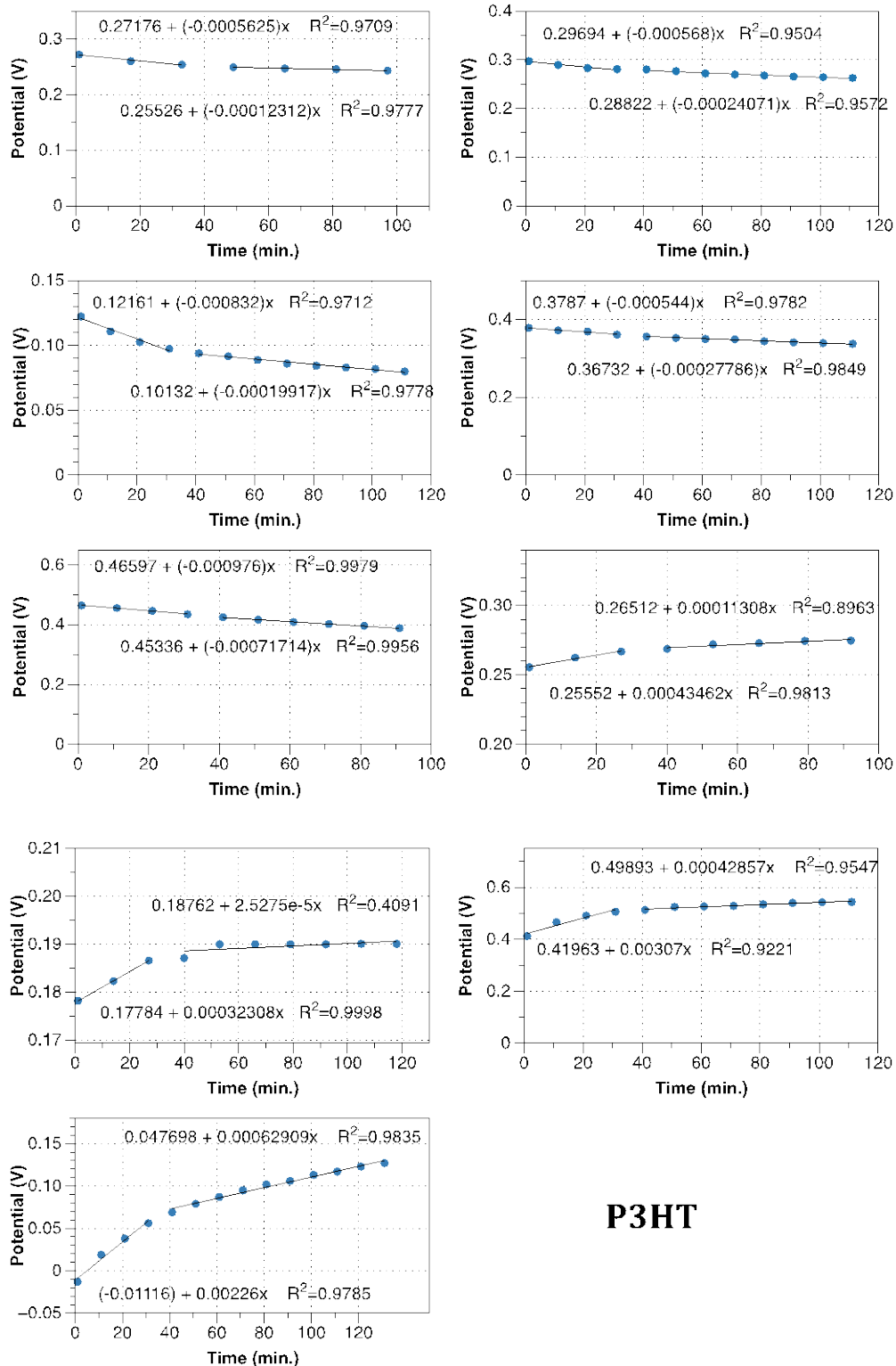
### **KINETICS MODELING**

This appendix comprises supplementary plots to Chapter 4, Time Evolution of Asymmetric Potential Distributions. The first figures were utilized to calculate the average change in potential with scan time.



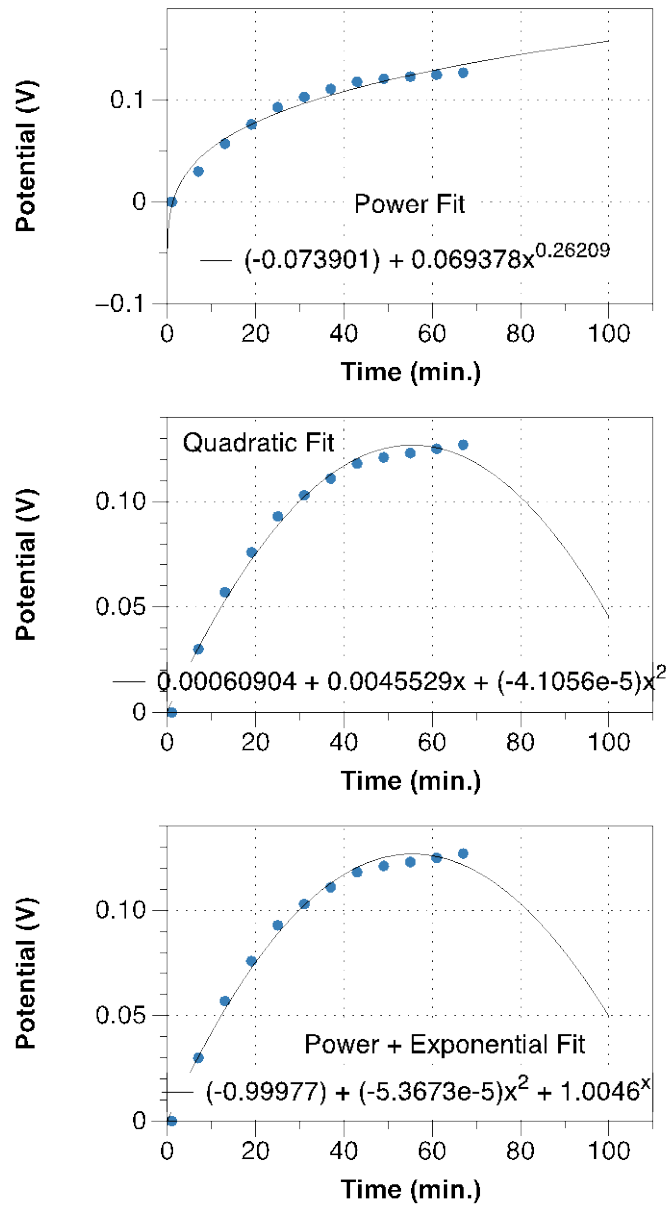
## PEDOT:PSS

**Appendix Figure 12** Peak potential versus scan time for several PEDOT:PSS samples. Linear fits were utilized to calculate the average change in potential over scan time for each of the two discharge regions.



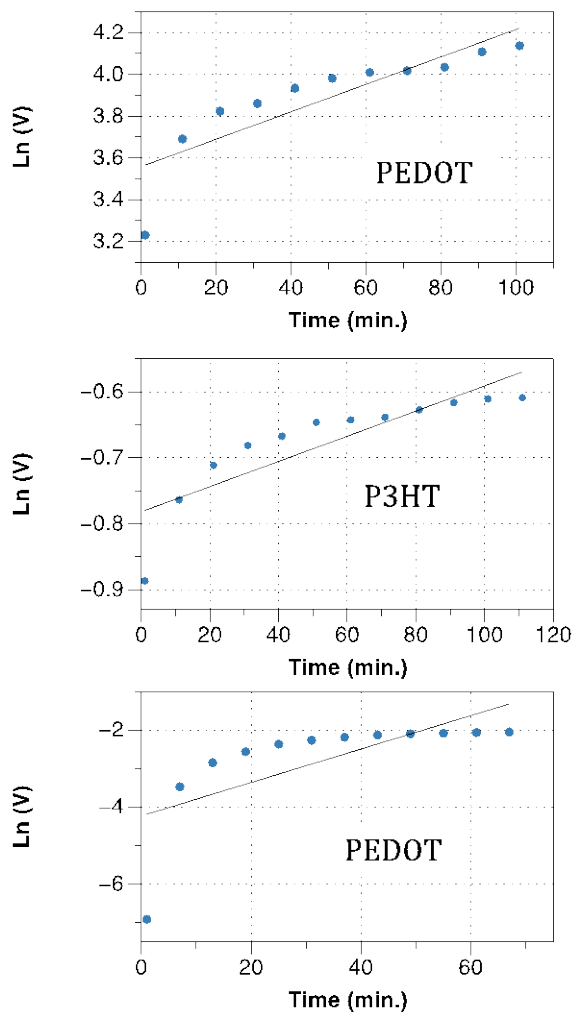
**Appendix Figure 13** Peak potential versus scan time for several P3HT samples. Linear fits were utilized to calculate the average change in potential over scan time for each of the two discharge regions.

The figure below is an example graph of functions utilized for modeling the potential versus scan time plots.

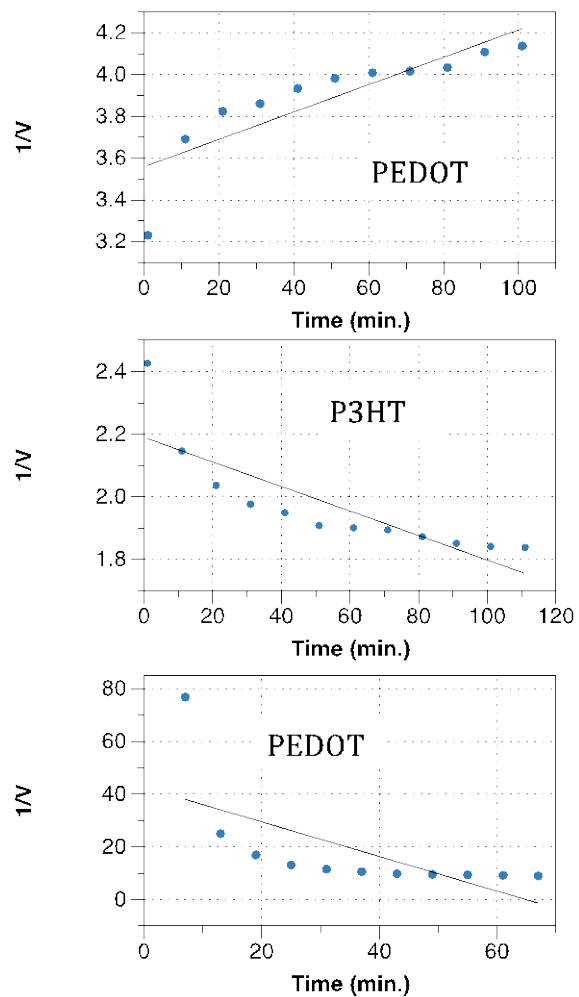


**Appendix Figure 14** Example plots of fits attempting to model potential discharge data.

Below are first and second order rate plot examples for three of the discharge samples. If the data were first order, a plot of  $\ln V$  versus time would be linear. Similarly, if the data were second order, a plot of  $1/V$  versus time would be linear. As is evident below, the data are not well approximated by either.



**Appendix Figure 15** Example first order rate plots for three samples (indicated).



Appendix Figure 16 Example second order rate plots for three samples (indicated).

## APPENDIX C

### LAYER-BY-LAYER DEPOSITION TROUBLESHOOTING

#### C.1 INTRODUCTION

Layer-by-layer deposition is a common technique to build films that are several atomic layers thick. Before its development, there were limitations for the thickness of films possible for deposition at the two ends of the spectrum, monolayers (nm) to bulk films ( $\mu\text{m}$ -mm). The former could be created through various chemisorption methods, for instance deposition of a long-chain silane onto a modified glass substrate via an R-S-O-substrate bond. Thicker films are deposited through methods like drop casting, spin coating, and various vapor deposition methods.

The theory behind the layer-by-layer method is a build dependent on the electrostatic interaction of one layer with another. A layer-by-layer assembly of phthalocyanine films was developed by our group following a procedure<sup>48</sup> utilizing solutions of varying pH to build the film. After synthesizing water-soluble phthalocyanine solutions, solutions were split in half and one was brought to pH 3 and the other to pH 11. To build the samples, the ITO-glass substrates were cleaned and dried, then immersed in a polydiallyldimethylammonium chloride (PDDA) solution to functionalize the surface and aid the first monolayer's binding. Then, the ITO glass substrate was successively immersed in each solution to build a layer each time, relying on the

attraction of opposite charges in each layer to build upon themselves. However, after depositing several samples, the expected thickness reported in the preceding paper was not detected. Instead, films were much thinner and did not appear to accumulate full layers with each immersion. This implied that the film deposition details previously outlined were not due to alternating pH solutions, but some other unknown effect.

## C.2 TESTS

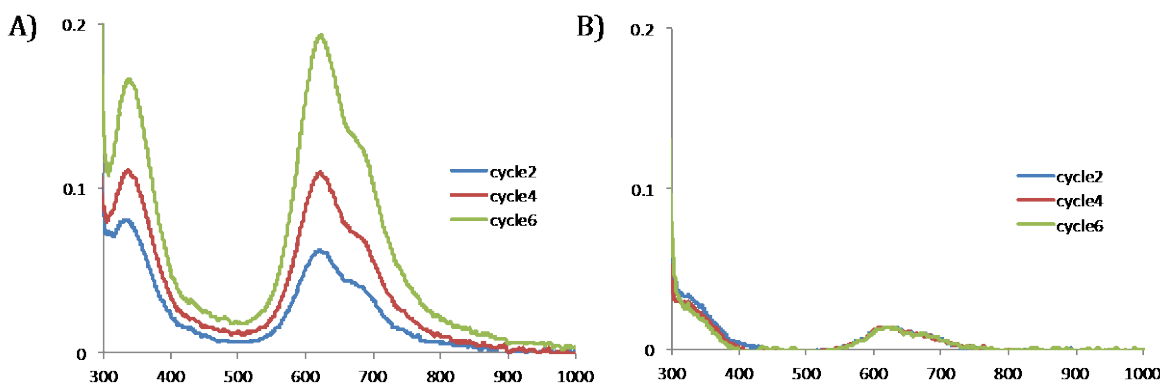
After evaluating the steps of the deposition process, the problem was narrowed down to the PDDA pre-treatment and the washing steps between each successive layer. Thus, several variations of the stamping process were analyzed to isolate the true cause of the deposition witnessed in the previous paper. Those variations are summarized in Table A.1 below.

**Appendix Table 1.** Summary of varied film samples for troubleshooting layer-by-layer deposition.

Pre Treatments	Washes Between Layers	Alternating solutions
Cleaning, PDDA	Ultrapure water	pH 3 / pH 9
Cleaning only	Ultrapure water “contaminated with PDDA”	pH 3 / pH 3
-	No wash	pH 9 / pH 9

All possible permutations of the variations outlined in the table above were created and characterized in multiple ways. The most compelling evidence came from absorbance measurements and AFM topography tests. The absorbance of each layer of the film was measured (Appendix Figure 12) as it was being deposited to determine whether additional layers

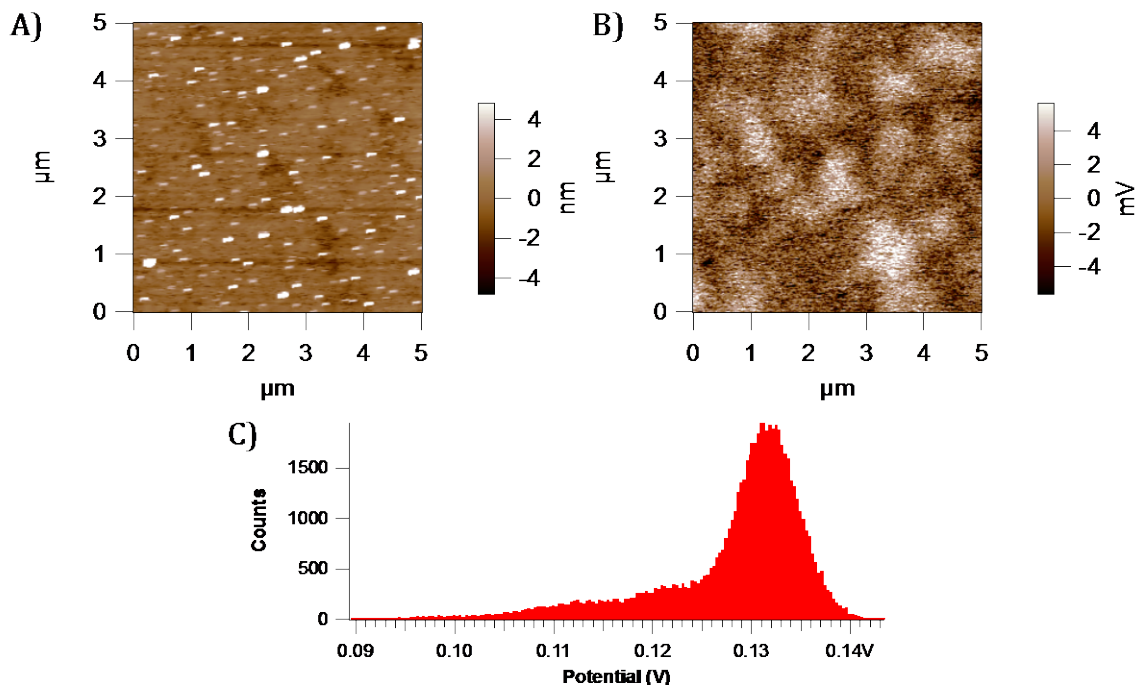
were being deposited in each step. This is made possible due to the deep color of the phthalocyanine compounds: more layers produce a deeper color in the film, which is exhibited in a higher absorbance value.



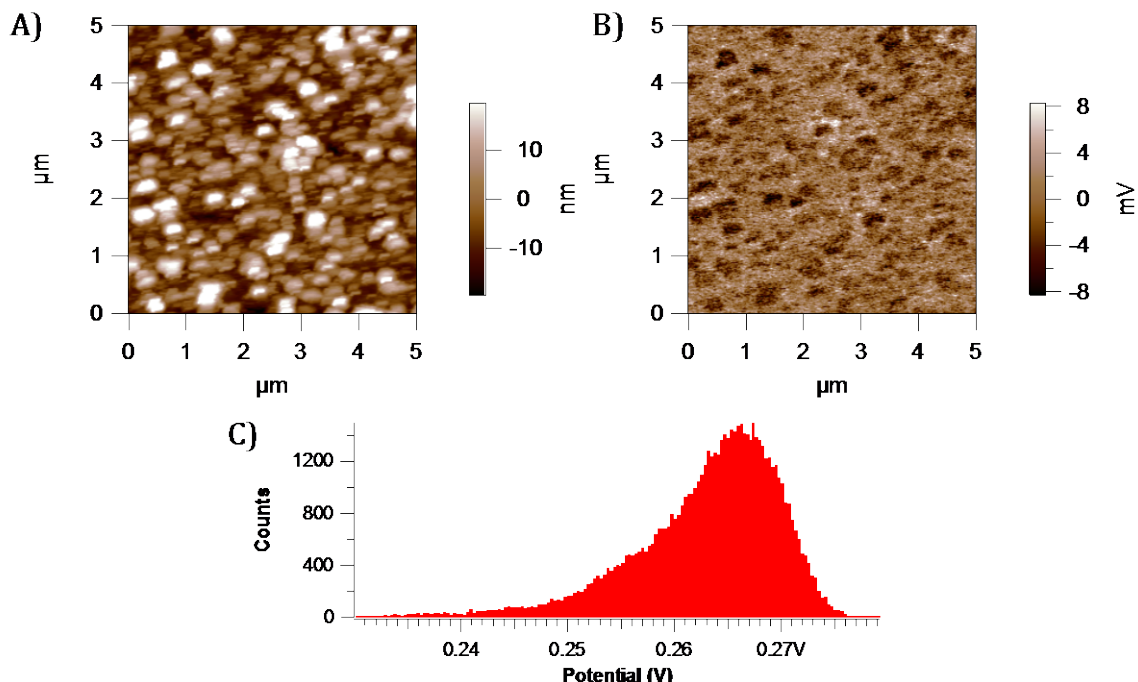
**Appendix Figure 17.** UV-Vis spectra for phthalocyanine films tested for film deposition troubleshooting. A) shows spectra for films where PDDA was added to the wash water between film layers and spectra in B) are for films with no PDDA in the water bath. As can be seen, there is no appreciable film deposition without additional PDDA. Work done by Xialing Chen.

After this process, all of the film samples were tested via KPFM to evaluate several sample parameters, including thicknesses of the films, surface potential relative to one another, and RMS roughness of the height scan. Film thickness would shed light on whether we were getting consistent layer deposition. Surface potential information, while on an arbitrary scale, would be helpful in comparing multiple samples created and characterized at the same time. PDDA, in theory, contributes positive charges/energy to the film samples, which can be monitored via surface potential. The use of the same tip and same timeframe for scanning would mean that temperature, humidity, tip contamination etc. (common instrument artifacts) were minimized and measured surface potential values relative to one another are useful.

Theoretically, roughness correlates with increases in the number of layers deposited, but in practice this is not the case. As there may not be complete deposition across the entire sample, larger variations in height would be seen with increasingly thick films due to the somewhat disordered nature of small molecule film samples.



**Appendix Figure 18.** KPFM data for phthalocyanine layer-by-layer films without PDDA in water baths used for rinsing samples between sample layers, including: A) height scan, B) potential scan, and C) potential histogram.



**Appendix Figure 19.** KPFM data for phthalocyanine layer-by-layer films with PDDA in water baths used for rinsing samples between sample layers, including: A) height scan, B) potential scan, and C) potential histogram. In comparing this figure with Appendix Figure 13 above, a far rougher height profile is seen.

### C.3 DISCUSSION

The tests outlined in the previous section implied that the deposition of each successive layer during the immersion process was not facilitated by the interaction of opposite charges from the alternating acid-basic solutions. In fact, the deciding factor in whether another layer was successfully added to the film or not was the presence of additional PDDA in the wash water between the phthalocyanine layers.

Significant growth was seen (as is seen in Appendix Figure 12 above) with all alternating phthalocyanine solutions (both alternating pH's and with the same successive solution in all layers) as long as PDDA (~5 drops) was present in the water of the wash bath between the

layers. When PDDA was not in the wash bath, there was no measurable addition with each immersion.

Evaluation of the AFM images supported these conclusions. As expected, thicker films grew with the use of PDDA in the water bath as measured by the range recorded in all of the height images. Surface potential values were consistently more positive for those films as well. While this does not implicitly imply that layers were deposited each time, it is unlikely that positive charges from the PDDA would penetrate the entire film to the surface to affect the surface potential values measured if the PDDA were only at the substrate/film interface. The fact that a consistently more positive surface potential was seen in samples with PDDA in the water bath indicates that the PDDA is intermixed in the phthalocyanine layers and can contribute to energetics at the surface. RMS roughness as calculated in the Asylum Research instrument software saw an increase from samples without PDDA to samples with PDDA in the water baths during preparation. For example, the samples in Appendix Figures 13 and 14 above had height roughness values of 1.486 and 8.897, respectively. This increase is indicative of a thicker film.

Interestingly, the increase in roughness also provides evidence that PDDA is involved in the layer-by-layer building process. With such a small concentration of PDDA utilized in the water bath (a few drops for ~200 mL ultrapure water), coverage of the PDDA on the phthalocyanine layers would be intermittent at best, contributing to a more uneven, disordered film above. Also, as a disordered polymer, the material itself would also lend itself to a rough distribution on the surface of the phthalocyanine layer. This method of characterization has proved useful for determining the underlying factors affecting the layer-by-layer deposition of metal phthalocyanines. PDDA is identified as the root cause of deposition with cyclic immersion of sample substrates in material solutions.

## **APPENDIX D**

### **ELECTROCHEMICAL CHARACTERIZATION OF FILMS**

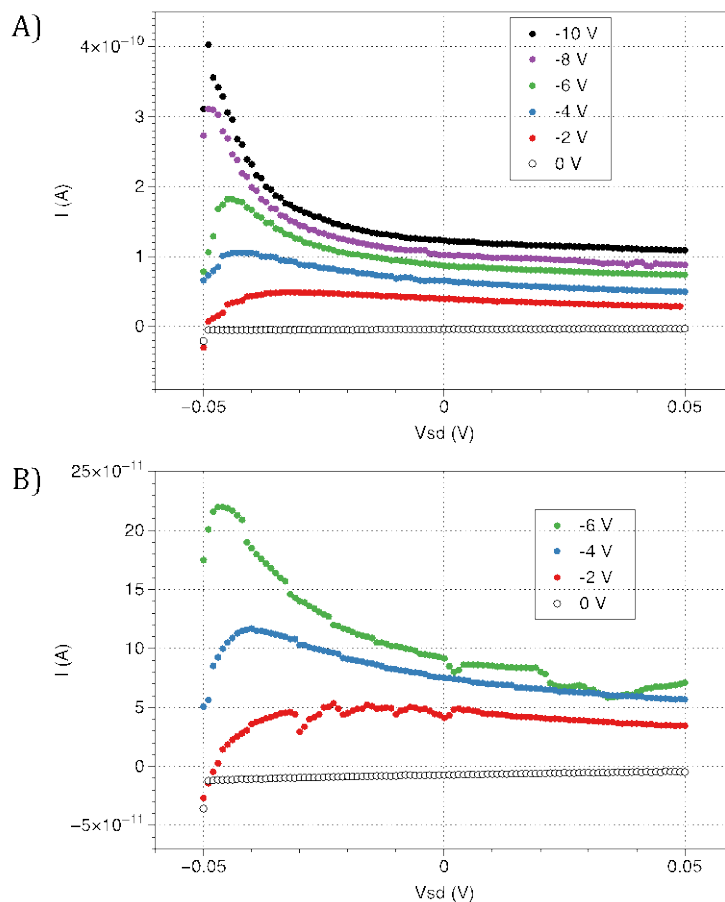
Electrochemical characterization of materials is useful for determining many characteristics. Commonly, current-voltage (IV) curves are produced by analysis either of material solutions or materials deposited as a thin film or device. Based on the type of sample in question, IV curves can provide information about the workings of a device or on parameters of a material and typically follow characteristic profiles. For example, a transistor exhibits a drastically different IV curve than a photovoltaic, and information about efficiency and device operation can be calculated from the curves very easily.

While collaborating with a student in another group in the chemistry department, I had the opportunity to analyze carbon nanotube transistors. The goal of the project was to determine whether the nanotubes synthesized via a novel method developed by the Liu group (unpublished work, similar to Surwade, et al<sup>95</sup>) would be suitable for use in transistor applications.

The setup of the probe station utilized three electrodes for analysis: source, drain, and gate. While all three of the electrodes could be placed on top of the sample for top-contact transistors, the setup was also equipped for bottom-contact transistors via a conducting stage. During analysis, a preset gate voltage was applied along with a specific sweep of source-drain

voltage. Then, using a source meter, the current between the source and drain was measured as a function of source-drain voltage.

As can be seen in the figure below, there was some transistor behavior witnessed in the electrochemical analysis. However, the nanotube devices produced were deemed too unstable and unreliable for continued study.



**Appendix Figure 20.** Two current-voltage (IV) curves for nanotube devices. Both were created on the same wafer in the same way, with silver paint dotted on the ends of the nanotubes to create contacts.

Experimental challenges with nanotube devices were numerous and included little reproducibility, no consistency in devices, and contact deposition. With no changes in production

method, devices and nanotube characteristics (number, length, width, etc.) deviated significantly between different wafers. This, in turn, yielded transistor data with very different current values and IV curve shape. In addition, many devices produced no working transistor curves at all. Not only were devices inconsistent between different wafers, even those on the same wafer had the same issues. Silver paint as a contact for the devices worked well when there was sufficient coverage of the nanotube, but because of their very small size, this occurrence was intermittent at best.

Though the devices showed the promise of working transistor behavior, without more development of the synthetic method to produce reliable nanotubes and working contacts, the project was unfeasible. Practically speaking, the devices would need to be much more reliable to make the project line worthwhile.

## BIBLIOGRAPHY

- (1) Kagan, C. R. Organic-Inorganic Hybrid Materials as Semiconducting Channels in Thin-Film Field-Effect Transistors. *Science* **1999**, *286*, 945–947.
- (2) Askerov, B. M. O. Electron Transport Phenomena in Semiconductors; World Scientific, 1994.
- (3) Hanwell, M. D.; Madison, T. A.; Hutchison, G. R. Charge Transport in Imperfect Organic Field Effect Transistors: Effects of Explicit Defects and Electrostatics. *J. Phys. Chem. C* **2010**, *114*, 20417–20423.
- (4) Madison, T. A.; Gagorik, A. G.; Hutchison, G. R. Charge Transport in Imperfect Organic Field Effect Transistors: Effects of Charge Traps. *J. Phys. Chem. C* **2012**, *116*, 11852–11858.
- (5) Gagorik, A. G.; Hutchison, G. R. Simulating Charge Injection and Dynamics in Microscale Organic Field-Effect Transistors. *J. Phys. Chem. C* **2012**, *116*, 21232–21239.
- (6) Bassler, H. Charge Transport in Disordered Organic Photoconductors-a Monte-Carlo Simulation Study. *Phys. Status Solidi B* **1993**, *175*, 15–56.
- (7) Bässler, H.; Köhler, A. Charge Transport in Organic Semiconductors. *Top Curr Chem* **2012**, *312*, 1–65.
- (8) Marcus, R. A. Chemical and Electrochemical Electron-Transfer Theory. *Annual Review of Physical Chemistry* **1964**, *15*, 155–&.
- (9) Marcus, R. A.; Sutin, N. Electron Transfers in Chemistry and Biology. *Biochimica et Biophysica Acta (BBA) - Reviews on Bioenergetics* **1985**, *811*, 265–322.
- (10) Chin, S.-C.; Chang, Y.-C.; Hsu, C.-C.; Lin, W.-H.; Wu, C.-I.; Chang, C.-S.; Tsong, T. T.; Woon, W.-Y.; Lin, L.-T.; Tao, H.-J. Two-Dimensional Dopant Profiling by Electrostatic Force Microscopy Using Carbon Nanotube Modified Cantilevers. *Nanotechnology* **2008**, *19*, 325703.
- (11) Riviere, J. C. Contact Potential Difference Measurements by the Kelvin Method. *Proceedings of the Physical Society of London Section B* **1957**, *70*, 676–686.

- (12) Smith, J.; Zhang, W.; Sougrat, R.; Zhao, K.; Li, R.; Cha, D.; Amassian, A.; Heeney, M.; McCulloch, I.; Anthopoulos, T. D. Solution-Processed Small Molecule-Polymer Blend Organic Thin-Film Transistors with Hole Mobility Greater Than 5  $\text{cm}^2/\text{vs}$ . *Adv. Mater.* **2012**, *24*, 2441–2446.
- (13) Thompson, B. C.; Fréchet, J. M. J. Organic Photovoltaics - Polymer-Fullerene Composite Solar Cells. *Angew. Chem. Int. Ed.* **2008**, *47*, 58–77.
- (14) Li, G.; Shrotriya, V.; Huang, J. S.; Yao, Y.; Moriarty, T.; Emery, K.; Yang, Y. High-Efficiency Solution Processable Polymer Photovoltaic Cells by Self-Organization of Polymer Blends. *Nat Mater* **2005**, *4*, 864–868.
- (15) Jones, B. A.; Facchetti, A.; Wasielewski, M. R.; Marks, T. J. Tuning Orbital Energetics in Arylene Diimide Semiconductors. Materials Design for Ambient Stability of N-Type Charge Transport. *J. Am. Chem. Soc.* **2007**, *129*, 15259–15278.
- (16) Bao, Z.; Dodabalapur, A.; Lovinger, A. J. Soluble and Processable Regioregular Poly(3-Hexylthiophene) for Thin Film Field-Effect Transistor Applications with High Mobility. *Appl. Phys. Lett.* **1996**, *69*, 4108–4110.
- (17) Sirringhaus, H.; Kawase, T.; Friend, R. H.; Shimoda, T.; Inbasekara, M.; Wu, W.; Woo, E. P. High-Resolution Inkjet Printing of All-Polymer Transistor Circuits. *Science* **2000**, *290*, 2123–2126.
- (18) Mas-Torrent, M.; Rovira, C. Novel Small Molecules for Organic Field-Effect Transistors: Towards Processability and High Performance. *Chem. Soc. Rev.* **2008**, *37*, 827–838.
- (19) McCulloch, I.; Heeney, M.; Bailey, C.; Genevicius, K.; Macdonald, I.; Shkunov, M.; Sparrowe, D.; Tierney, S.; Wagner, R.; Zhang, W.; et al. Liquid-Crystalline Semiconducting Polymers with High Charge-Carrier Mobility. *Nat Mater* **2006**, *5*, 328–333.
- (20) Finlayson, C. E.; Friend, R. H.; Otten, M. B. J.; Schwartz, E.; Cornelissen, J. J. L. M.; Nolte, R. L. M.; Rowan, A. E.; Samorì, P.; Palermo, V.; Liscio, A.; et al. Electronic Transport Properties of Ensembles of Perylene-Substituted Poly-Isocyanopeptide Arrays. *Adv. Funct. Mater.* **2008**, *18*, 3947–3955.
- (21) Sancho-García, J. C.; Pérez-Jiménez, A. J. Accurate Calculation of Transport Properties for Organic Molecular Semiconductors with Spin-Component Scaled MP2 and Modern Density Functional Theory Methods. *J Chem Phys* **2008**, *129*, 024103.
- (22) Li, C.; Duan, L.; Sun, Y.; Li, H.; Qiu, Y. Charge Transport in Mixed Organic Disorder Semiconductors: Trapping, Scattering, and Effective Energetic Disorder. *Journal of Physical Chemistry C* **2012**, *116*, 19748–19754.
- (23) Roberson, L. B.; Kowalik, J.; Tolbert, L. M.; Kloc, C.; Zeis, R.; Chi, X. L.; Fleming, R.; Wilkins, C. Pentacene Disproportionation During Sublimation for Field-Effect

- Transistors. *J. Am. Chem. Soc.* **2005**, *127*, 3069–3075.
- (24) Shtein, M.; Mapel, J.; Benziger, J. B.; Forrest, S. R. Effects of Film Morphology and Gate Dielectric Surface Preparation on the Electrical Characteristics of Organic-Vapor-Phase-Deposited Pentacene Thin-Film Transistors. *Appl. Phys. Lett.* **2002**, *81*, 268–270.
- (25) Lee, B.; Chen, Y.; Fu, D.; Yi, H. T.; Czelen, K.; Najafov, H.; Podzorov, V. Trap Healing and Ultralow-Noise Hall Effect at the Surface of Organic Semiconductors. *Nat Mater* **2013**, *12*, 1125–1129.
- (26) Olthof, S.; Mehraeen, S.; Mohapatra, S. K.; Barlow, S.; Coropceanu, V.; Brédas, J.-L.; Marder, S. R.; Kahn, A. Ultralow Doping in Organic Semiconductors: Evidence of Trap Filling. *Phys Rev Lett* **2012**, *109*.
- (27) Chang, L. L.; Esaki, L.; Tsu, R. Resonant Tunneling in Semiconductor Double Barriers. *Appl. Phys. Lett.* **1974**, *24*, 593–595.
- (28) Zhou, C. W.; Kong, J.; Yenilmez, E.; Dai, H. J. Modulated Chemical Doping of Individual Carbon Nanotubes. *Science* **2000**, *290*, 1552–1555.
- (29) Chitta, R.; Rogers, L. M.; Wanklyn, A.; Karr, P. A.; Kahol, P. K.; Zandler, M. E.; D'Souza, F. Electrochemical, Spectral, and Computational Studies of Metalloporphyrin Dimers Formed by Cation Complexation of Crown Ether Cavities. *Inorganic Chemistry* **2004**, *43*, 6969–6978.
- (30) Ma, W.; Ye, L.; Zhang, S.; Hou, J.; Ade, H. Competition Between Morphological Attributes in the Thermal Annealing and Additive Processing of Polymer Solar Cells. *J. Mater. Chem. C* **2013**, *1*, 5023.
- (31) Qiu, L.; Xu, Q.; Lee, W. H.; Wang, X.; Kang, B.; Lv, G.; Cho, K. Organic Thin-Film Transistors with a Photo-Patternable Semiconducting Polymer Blend. *J. Mater. Chem.* **2011**, *21*, 15637.
- (32) Jung, J. S.; Cho, E. H.; Jo, S.; Kim, K. H.; Choi, D. H.; Joo, J. Photo-Induced Negative Differential Resistance of Organic Thin Film Transistors Using Anthracene Derivatives. *Org. Electron.* **2013**, *14*, 2204–2209.
- (33) Servaites, J.; Ratner, M.; Marks, T. Organic Solar Cells: a New Look at Traditional Models. *Energy Environ. Sci.* **2011**, *4*, 13.
- (34) Luria, J. L.; Schwarz, K. A.; Jaquith, M. J.; Hennig, R. G.; Marohn, J. A. Spectroscopic Characterization of Charged Defects in Polycrystalline Pentacene by Time- and Wavelength-Resolved Electric Force Microscopy. *Adv. Mater.* **2011**, *23*, 624–628.
- (35) Bernasek, S. L. Can We Understand the Molecule in Molecular Electronics? *Angew. Chem. Int. Ed.* **2012**, *51*, 9737–9738.
- (36) Janssen, R. A. J.; Nelson, J. Factors Limiting Device Efficiency in Organic

- Photovoltaics. *Adv. Mater.* **2012**, *13*, 1847–1858.
- (37) Eder, F.; Klauk, H.; Halik, M.; Zschieschang, U.; Schmid, G.; Dehm, C. Organic Electronics on Paper. *Appl. Phys. Lett.* **2004**, *84*, 2673.
- (38) Nelson, J.; Kwiatkowski, J. J.; Kirkpatrick, J.; Frost, J. M. Modeling Charge Transport in Organic Photovoltaic Materials. *Accounts Chem Res* **2009**, *42*, 1768–1778.
- (39) Gwinner, M. C.; Pietro, R. D.; Vaynzof, Y.; Greenberg, K. J.; Ho, P. K. H.; Friend, R. H.; Siringhaus, H. Doping of Organic Semiconductors Using Molybdenum Trioxide: a Quantitative Time-Dependent Electrical and Spectroscopic Study. *Adv. Funct. Mater.* **2011**, *21*, 1432–1441.
- (40) Shaked, S.; Tal, S.; Roichman, Y.; Razin, A.; Xiao, S.; Eichen, Y.; Tessler, N. Charge Density and Film Morphology Dependence of Charge Mobility in Polymer Field- Effect Transistors. *Adv. Mater.* **2003**, *15*, 913–916.
- (41) Puntambekar, K.; Dong, J.; Haugstad, G.; Frisbie, C. D. Structural and Electrostatic Complexity at a Pentacene/Insulator Interface. *Adv. Funct. Mater.* **2006**, *16*, 6.
- (42) Kim, Y.; Ballantyne, A. M.; Nelson, J.; Bradley, D. D. C. Effects of Thickness and Thermal Annealing of the PEDOT: PSS Layer on the Performance of Polymer Solar Cells. *Org. Electron.* **2009**, *10*, 205–209.
- (43) Zerweck, U.; Loppacher, C.; Otto, T.; Grafström, S.; Eng, L. M. Accuracy and Resolution Limits of Kelvin Probe Force Microscopy. *Phys. Rev. B* **2005**, *71*, 125424.
- (44) Tal, O.; Rosenwaks, Y.; Preezant, Y.; Tessler, N.; Chan, C.; Kahn, A. Direct Determination of the Hole Density of States in Undoped and Doped Amorphous Organic Films with High Lateral Resolution. *Phys Rev Lett* **2005**, *95*, 256405.
- (45) Meoded, T.; Shikler, R.; Fried, N.; Rosenwaks, Y. Direct Measurement of Minority Carriers Diffusion Length Using Kelvin Probe Force Microscopy. *Appl. Phys. Lett.* **1999**, *75*, 2435.
- (46) Reid, O. G.; Rayermann, G. E.; Coffey, D. C.; Ginger, D. S. Imaging Local Trap Formation in Conjugated Polymer Solar Cells: a Comparison of Time-Resolved Electrostatic Force Microscopy and Scanning Kelvin Probe Imaging. *J. Phys. Chem. C* **2010**, *114*, 20672–20677.
- (47) Maturová, K.; Kemerink, M.; Wienk, M. M.; Charrier, D. S. H.; Janssen, R. A. J. Scanning Kelvin Probe Microscopy on Bulk Heterojunction Polymer Blends. *Adv. Funct. Mater.* **2009**, *19*, 1379–1386.
- (48) Bertocello, P.; Peruffo, M. An Investigation on the Self-Aggregation Properties of Sulfonated Copper(II) Phthalocyanine (CuTsPc) Thin Films. *Colloid Surface A* **2008**, *321*, 106–112.

- (49) la Torre, de, G.; Claessens, C. G.; Torres, T. Phthalocyanines: Old Dyes, New Materials. Putting Color in Nanotechnology. *Chem. Commun.* **2007**, 2000.
- (50) McCulloch, I.; Bailey, C.; Giles, M.; Heeney, M.; Love, I.; Shkunov, M.; Sparrowe, D.; Tierney, S. Influence of Molecular Design on the Field-Effect Transistor Characteristics of Terthiophene Polymers. *Chem. Mater.* **2005**, *17*, 1381–1385.
- (51) Craley, C. R.; Zhang, R.; Kowalewski, T.; McCullough, R. D.; Stefan, M. C. Regioregular Poly(3-Hexylthiophene) in a Novel Conducting Amphiphilic Block Copolymer. *Adv. Mater.* **2009**, *30*, 11–16.
- (52) Mishra, A.; Bäuerle, P. Small Molecule Organic Semiconductors on the Move: Promises for Future Solar Energy Technology. *Angew. Chem. Int. Ed.* **2012**, *51*, 2020–2067.
- (53) Bao, Z.; Lovinger, A. J.; Dodabalapur, A. Organic Field-Effect Transistors with High Mobility Based on Copper Phthalocyanine. *Appl. Phys. Lett.* **1996**, *69*, 3066.
- (54) McMahon, D. P.; Troisi, A. Organic Semiconductors: Impact of Disorder at Different Timescales. *ChemPhysChem* **2010**, *11*, 2067–2074.
- (55) Kim, W. H.; Mäkinen, A. J.; Nikolov, N.; Shashidhar, R.; Kim, H.; Kafafi, Z. H. Molecular Organic Light-Emitting Diodes Using Highly Conducting Polymers as Anodes. *Appl. Phys. Lett.* **2002**, *80*, 3844.
- (56) Pearson, K. On the General Theory of Skew Correlation and Non-Linear Regression; Cambridge University Press: London, 1905.
- (57) Jones, E.; Oliphant, T.; Peterson, P. SciPy: Open Source Scientific Tools for Python. *www.scipy.org* **2001**.
- (58) Grossiord, N.; Kroon, J. M.; Andriessen, R.; Blom, P. W. M. Degradation Mechanisms in Organic Photovoltaic Devices. *Org. Electron.* **2011**, *13*, 432–456.
- (59) Acton, O.; Dubey, M.; Weidner, T.; O'Malley, K. M.; Kim, T.-W.; Ting, G. G.; Hutchins, D.; Baio, J. E.; Lovejoy, T. C.; Gage, A. H.; et al. Simultaneous Modification of Bottom-Contact Electrode and Dielectric Surfaces for Organic Thin-Film Transistors Through Single-Component Spin-Cast Monolayers. *Adv. Funct. Mater.* **2011**, *21*, 1476–1488.
- (60) Knesting, K. M.; Hotchkiss, P. J.; MacLeod, B. A.; Marder, S. R.; Ginger, D. S. Spatially Modulating Interfacial Properties of Transparent Conductive Oxides: Patterning Work Function with Phosphonic Acid Self-Assembled Monolayers. *Adv. Mater.* **2012**, *24*, 642–646.
- (61) Leever, B. J.; Murray, I. P.; Durstock, M. F.; Marks, T. J.; Hersam, M. C. Influence of Indium Tin Oxide Surface Treatment on Spatially Localized Photocurrent Variations in Bulk Heterojunction Organic Photovoltaic Devices. *J. Phys. Chem. C* **2011**, *115*, 22688–22694.

- (62) DiBenedetto, S. A.; Facchetti, A.; Ratner, M. A.; Marks, T. J. Molecular Self-Assembled Monolayers and Multilayers for Organic and Unconventional Inorganic Thin-Film Transistor Applications. *Adv. Mater.* **2009**, *21*, 1407–1433.
- (63) Gagorik, A. G.; Mohin, J. W.; Kowalewski, T.; Hutchison, G. R. Monte Carlo Simulations of Charge Transport in 2D Organic Photovoltaics. *J. Phys. Chem. Lett.* **2012**, *4*, 36–42.
- (64) Liscio, A.; Veronese, G. P.; Treossi, E.; Suriano, F.; Rossella, F.; Bellani, V.; Rizzoli, R.; Samorì, P.; Palermo, V. Charge Transport in Graphene–Polythiophene Blends as Studied by Kelvin Probe Force Microscopy and Transistor Characterization. *J. Mater. Chem.* **2011**, *21*, 2924.
- (65) Bolinger, J. C.; Fradkin, L.; Lee, K. J.; Palacios, R. E.; Barbara, P. F. Light-Assisted Deep-Trapping of Holes in Conjugated Polymers. *Proceedings of the National Academy of Sciences* **2009**, *106*, 1342–1346.
- (66) Palacios, R. E.; Fan, F.-R. F.; Grey, J. K.; Suk, J.; Bard, A. J.; Barbara, P. F. Charging and Discharging of Single Conjugated-Polymer Nanoparticles. *Nat Mater* **2007**, *6*, 680–685.
- (67) Palacios, R. E.; Fan, F.-R. F.; Bard, A. J.; Barbara, P. F. Single-Molecule Spectroelectrochemistry (SMS-EC). *J. Am. Chem. Soc.* **2006**, *128*, 9028–9029.
- (68) Hallam, T.; Lee, M.; Zhao, N.; Nandhakumar, I.; Kemerink, M.; Siringhaus, H. Local Charge Trapping in Conjugated Polymers Resolved by Scanning Kelvin Probe Microscopy. *Phys Rev Lett* **2009**, *103*, 4.
- (69) Ando, M.; Heike, S.; Kawasaki, M.; Hashizume, T. Trapped Charge Mapping in Crystalline Organic Transistors by Using Scanning Kelvin Probe Force Microscopy. *Appl. Phys. Lett.* **2014**, *105*, 193303.
- (70) Ando, M.; Kehoe, T. B.; Yoneya, M.; Ishii, H.; Kawasaki, M.; Duffy, C. M.; Minakata, T.; Phillips, R. T.; Siringhaus, H. Evidence for Charge- Trapping Inducing Polymorphic Structural- Phase Transition in Pentacene. *Adv. Mater.* **2015**, *27*, 122–129.
- (71) Teague, L. C.; Loth, M. A.; Anthony, J. E. Influence of Film Structure and Light on Charge Trapping and Dissipation Dynamics in Spun-Cast Organic Thin-Film Transistors Measured by Scanning Kelvin Probe Microscopy. *Appl. Phys. Lett.* **2012**, *100*, 263305.
- (72) Muller, E. M. Electric Force Microscopy of Charge Trapping in Thin-Film Pentacene Transistors, 2005, pp. 1–141.
- (73) Jaquith, M.; Muller, E. M.; Marohn, J. A. Time-Resolved Electric Force Microscopy of Charge Trapping in Polycrystalline Pentacene. *J. Phys. Chem. B* **2007**, *111*, 7711–7714.
- (74) Kaake, L.; Dang, X. D.; Leong, W. L.; Zhang, Y. Effects of Impurities on Operational Mechanism of Organic Bulk Heterojunction Solar Cells. *Advanced ...* **2013**.

- (75) Kumar, B.; Kaushik, B. K.; Negi, Y. S. Organic Thin Film Transistors: Structures, Models, Materials, Fabrication, and Applications: a Review. *Polymer Reviews* **2014**, *54*, 33–111.
- (76) Lai, Y.-Y.; Liao, M.-H.; Chen, Y.-T.; Cao, F.-Y.; Hsu, C.-S.; Cheng, Y.-J. Compact Bis-Adduct Fullerenes and Additive-Assisted Morphological Optimization for Efficient Organic Photovoltaics. *ACS Appl. Mater. Interfaces* **2014**, *6*, 20102–20109.
- (77) Mazziro, K. A.; Luscombe, C. K. The Future of Organic Photovoltaics. *Chem. Soc. Rev.* **2015**, *44*, 78–90.
- (78) Yu, G.; Gao, J.; Hummelen, J. C.; Wudl, F.; Heeger, A. J. Polymer Photovoltaic Cells - Enhanced Efficiencies via a Network of Internal Donor-Acceptor Heterojunctions. *Science* **1995**, *270*, 1789–1791.
- (79) Dennler, G.; Scharber, M. C.; Brabec, C. J. Polymer-Fullerene Bulk-Heterojunction Solar Cells. *Adv. Mater.* **2009**, *21*, 1323–1338.
- (80) Ray, B.; Alam, M. A. Random vs Regularized OPV: Limits of Performance Gain of Organic Bulk Heterojunction Solar Cells by Morphology Engineering. *Sol Energ Mat Sol* **2012**, *99*, 204–212.
- (81) Shao, G.; Glaz, M. S.; Ma, F.; Ju, H.; Ginger, D. S. Intensity-Modulated Scanning Kelvin Probe Microscopy for Probing Recombination in Organic Photovoltaics. *pubs.acs.org*.
- (82) Sirringhaus, H. Device Physics of Solution-Processed Organic Field-Effect Transistors. *Adv. Mater.* **2005**, *17*, 2411–2425.
- (83) Hill, I. G.; Milliron, D.; Schwartz, J.; Kahn, A. Organic Semiconductor Interfaces: Electronic Structure and Transport Properties. *Appl Surf Sci* **2000**, *166*, 354–362.
- (84) Germack, D. S.; Checco, A.; Ocko, B. M. Directed Assembly of P3HT:PCBM Blend Films Using a Chemical Template with Sub-300 Nm Features. *ACS Nano* **2013**, *7*, 1990–1999.
- (85) Chen, F.-C.; Lin, Y.-K.; Ko, C.-J. Submicron-Scale Manipulation of Phase Separation in Organic Solar Cells. *Appl. Phys. Lett.* **2008**, *92*, 023307–023307–3.
- (86) Avnon, E.; Yaacobi-Gross, N.; Ploshnik, E.; Shenhar, R.; Tessler, N. Low Cost, Nanometer Scale Nanoimprinting–Application to Organic Solar Cells Optimization. *Org. Electron.* **2011**, *12*, 1241–1246.
- (87) Darling, D. R. EE-527: MicroFabrication, Photolithography.
- (88) Vandewal, K.; Himmelberger, S.; Salleo, A. Structural Factors That Affect the Performance of Organic Bulk Heterojunction Solar Cells. *Macromolecules* **2013**, 130729154511008.

- (89) Carr, J. A.; Chaudhary, S. The Identification, Characterization and Mitigation of Defect States in Organic Photovoltaic Devices: a Review and Outlook. *Energy & Environmental Science* **2013**, *6*, 3414–3438.
- (90) Bozyigit, D.; Wood, V. Electrical Characterization of Nanocrystal Solids. *J. Mater. Chem. C* **2014**, *2*, 3172–3184.
- (91) Neugebauer, S.; Rauh, J.; Deibel, C.; Dyakonov, V. Investigation of Electronic Trap States in Organic Photovoltaic Materials by Current-Based Deep Level Transient Spectroscopy. *Appl. Phys. Lett.* **2012**, *100*.
- (92) Stuchlikova, L.; Weis, M.; Juhasz, P.; Kosa, A.; Harmatha, L.; Jakabovic, J. Defect Analysis of Pentacene Diode. *Acta Physica Polonica A* **2014**, *125*, 1038–1041.
- (93) Hoffmann, P. B.; Gagorik, A. G.; Chen, X.; Hutchison, G. R. Asymmetric Surface Potential Energy Distributions in Organic Electronic Materials via Kelvin Probe Force Microscopy. *J. Phys. Chem. C* **2013**, *117*, 18367–18374.
- (94) Brumbach, M.; Veneman, P. A.; Marrikar, F. S.; Schulmeyer, T.; Simmonds, A.; Xia, W.; Lee, P.; Armstrong, N. R. Surface Composition and Electrical and Electrochemical Properties of Freshly Deposited and Acid-Etched Indium Tin Oxide Electrodes. *Langmuir* **2007**, *23*, 11089–11099.
- (95) Surwade, S. P.; Li, Z.; Liu, H. Thermal Oxidation and Unwrinkling of Chemical Vapor Deposition-Grown Graphene. *J. Phys. Chem. C* **2012**, *116*, 20600–20606.